Informatik

Respiratory Motion Correction on 3D Positron Emission Tomography Images

Inaugural-Dissertation
zur Erlangung des Doktorgrades
der Naturwissenschaften im Fachbereich
Mathematik und Informatik
der Mathematisch-Naturwissenschaftlichen Fakultät
der Westfälischen Wilhelms-Universität Münster

vorgelegt von
Mohammad Dawood
aus Tripoli
- 2008 -

Dekan:	Herr Prof. Dr. Dr. h.c. Joachim Cuntz
Erster Gutachter:	Herr Prof. Dr. Xiayoi Jiang
Zweiter Gutachter:	Herr Prof. Dr. Michael Schäfers
Tag der Promotion:	4.7.2008

Dedication

To my parents

Mohammad Yousuf Majoka and Khatija Begum

Acknowledgments

I would like to express my sincere thanks to Prof. X. Jiang and Prof. M. Schäfers for the guidance and sound scientific advice that I have enjoyed during the whole period of this work. Similarly my thanks go to Dr. K.P. Schäfers for enabling me to work in the medical physics research group at the department of nuclear medicine in Münster which has been a pleasant and enriching experience and for his support in many other ways which includes the visits that lead to an exchange of experience with other researchers in the field and helped in the improvement of this work.

Many sincere thanks to my friend and colleague F. Büther, he has been at the center of the wonderful atmosphere in the group, along with T. Kösters, M. Fieseler and N. Lang. They were all ever ready to help wherever they could. All of them also proof-read the manuscript and proposed improvements.

Contents

Abstract

Combined Positron emission tomography (PET) and Computed Tomography (CT), called PET/CT systems, are becoming more common with every passing day. These systems allow an anatomical as well as morphological insight into the body without large displacements. However the internal respiratory motion remains. This problem of respiratory motion is well known in PET/CT studies. The PET images are formed over an elongated period of time, typically many minutes. Whereas the CT images are formed within a few seconds. As the patients cannot hold breath during the PET acquisition, spatial blurring and motion artifacts are the natural result. Moreover, in many cases the PET and the CT parts of the studies do not correspond to each other spatially. This results in motion artifacts and wrong attenuation correction with the misregistered CT data. Wrong attenuation correction may lead to wrong quantification of the radioactive uptake, and possibly to wrong assessment.

A solution to this problem is presented in two steps:

- Gating of the PET data to get relatively motion-free snapshots by sorting the PET data with reference to a respiratory signal. A system for respiratory signal acquisition is devised and implemented which allows retrospective gating. Different methods of gating were compared and the best method, amplitude based variable gating, is selected. Gated images have less motion but poor quality due to the lack of statistics.

- The PET images are corrected for motion with an optical flow algorithm which estimates the deformation between two time frames and thus allows them to be co-registered accurately in a non-rigid fashion. The algorithm is based on a combined local and global optical flow method. Modifications were done to allow for discontinuity preservation across organ boundaries and the method was extended for application to 3D volume datasets. Motion correction restores the image quality by producing images containing all statistics and reduced motion.

To apply this solution to the specific task of motion correction in 3D PET/CT imagery, three additional aspects have to be dealt with:

- Optical flow algorithms can not be applied to large displacements due to inherent mathematical problems. A multi-resolution approach based upon Gaussian-pyramids is utilized to apply optical flow to large displacements.

- Motion correction of the PET is not sufficient, as the PET data has to be also corrected for attenuation inside the human body. For this the CT data has to be deformed to match the different PET respiratory phases.

- Motion correction performed on image data is not as accurate as that performed on the listmode data as the images are themself reconstructed from the listmode data in an iterative process which allows for small errors. Thus the motion vectors are incorporated in a listmode based reconstruction scheme to achieve higher precision.

The results of the study show that the motion of the heart due to respiration, which was as high as 25 mm in some patient datasets, was reduced to about 0.3 mm. This allows more accurate evaluation of the PET data and also minimizes the effects of misregistration between the PET and the CT datasets.

Outline

This study is divided into three main parts, introduction (chapters 1 to 3), gating (chapters 4 to 6) and optical flow (chapters 7 to 12). These parts can be summarized as follows.

The first chapter gives the basics of the instruments used in Positron Emission Tomography and the Computed Tomography. The physical properties of the markers used in PET studies and the process of image formation are also introduced. It also describes the different modes of acquiring the PET data as well as the factors limiting the resolution of the PET images and the motivation for hybrid PET/CT scanners. Along with the basics of PET/CT, the causes for large amount of noise on the images will become more obvious to the reader in this chapter.

The second chapter allows a basic insight in the process of reconstructing the images from the PET data. The acquired data is a forward projection of the distribution of the radiotracer in the body of the patient. From this data the original distribution has to be reconstructed using a backprojection. Different methods of reconstruction are described which include both analytical methods as radon transform and iterative methods as OSEM. Examples of reconstructed images are also provided for easy comparison. The reconstruction of the data also requires some correction, which are described in detail.

The third chapter presents different aspects of the problem of motion in PET/CT studies. The process of motion, it's magnitude in different organs and the effects of motion on PET/CT data are described. It will become apparent that respiratory motion is a serious problem in PET/CT studies which has clinical relevance. Not correcting the data for motion may lead to artifacts and mistakes in diagnosis and therapy planning. The proposed solution is outlined in the last section of this chapter.

Chapters four to six describe the first step of the proposed solution: Gating. The PET data can be divided and sorted in many ways to obtain images with less motion and statistics. After an overview of gating methods seven methods of gating are compared. The variable amplitudes method, devised especially for our task, is found to be the best method. Two aspects were considered while comparing the gating methods. These were the ability to capture the motion and the amount of noise present on the images. The results of the gating methods are given in chapter five and discussed in the sixth chapter.

Chapters seven introduces the second part of the proposed solution i.e. the optical flow methods. A short overview of the registration methods, optical flow methods and their applications form the base of the following sections. The mathematical foundations of the optical flow are described, and a discontinuity preserving optical flow method is presented. Comparison of five algorithms based on software phantom data and patient studies is included in the eighth chapter with a discussion of the results in the ninth one.

The optical flow algorithms confront difficulties when large displacements are present

on the images. As this is the case in respiratory motion, a multiresolution strategy to calculate optical flow is described in chapter ten. The results on real patient data are given and discussed to prove the correctness of the multiresolution scheme.

One part of the solution to the problem of motion in PET/CT data is specific to this kind of hybrid scanners. The PET data has to be corrected for density differences in the body tissues. To use spatially correct coefficients for this process, called attenuation correction, the CT data from the scanner has to be deformed to fit the PET data in different respiratory phases. This part of the solution is presented in chapter eleven.

Chapter twelve gives the complete motion correction scheme and its application to the reconstruction of PET data in listmode. The study is completed with chapter thirteen describing the conclusions and an outlook for future research in this area.

Part I

Introduction

Chapter 1

Instrumentation

Tomographic methods are very important in medical diagnosis as they allow examination of subjects without invasive surgical methods. Two of the most important methods of tomography are the computed tomography (CT) and the positron emission tomography (PET). The combined hybrid PET and CT systems are called PET/CT systems. This study is concerned with a problem which is related especially to the PET/CT data. Therefore, an introduction into the principle instruments of data acquisition is in place here. As the PET/CT scanners consist of two basic parts, namely the CT and the PET scanners, first both of these are introduced and than the special properties of the PET/CT are described in the following sections.

1.1 CT

CT (computed tomography) gives a detailed picture of the body's anatomical structures by taking cross-sectional images or x-ray slices of the body: as x-rays pass through the body they are absorbed or attenuated (weakened) at differing levels creating a profile of x-ray beams of different strength. This x-ray profile is registered on detectors which measure the x-ray profile.

The CT scanner itself is a circular, rotating frame with an x-ray tube mounted on one side and detectors on the other. A fan-shaped beam of x-rays is created as the rotating frame spins the x-ray tube and detectors around the patient. For each complete rotation, one cross-sectional slice of the body is acquired. The profiles taken are analyzed, and the full set of profiles from each rotation is compiled to form the slice image. The raw data produced during the CT scanning is not yet in image form. The actual image volume has to be reconstructed from this data after the acquisition process with the help of special reconstruction algorithms.

While CT does an excellent job of depicting structures and anatomy, it may miss small or early stage tumors. It also can not show the metabolization and thus the degree of health or damage in an organ.

1.2 PET

Positron emission tomography (PET) is a method of observing the biochemical functioning of cells by detecting how they process certain compounds, such as glucose. The

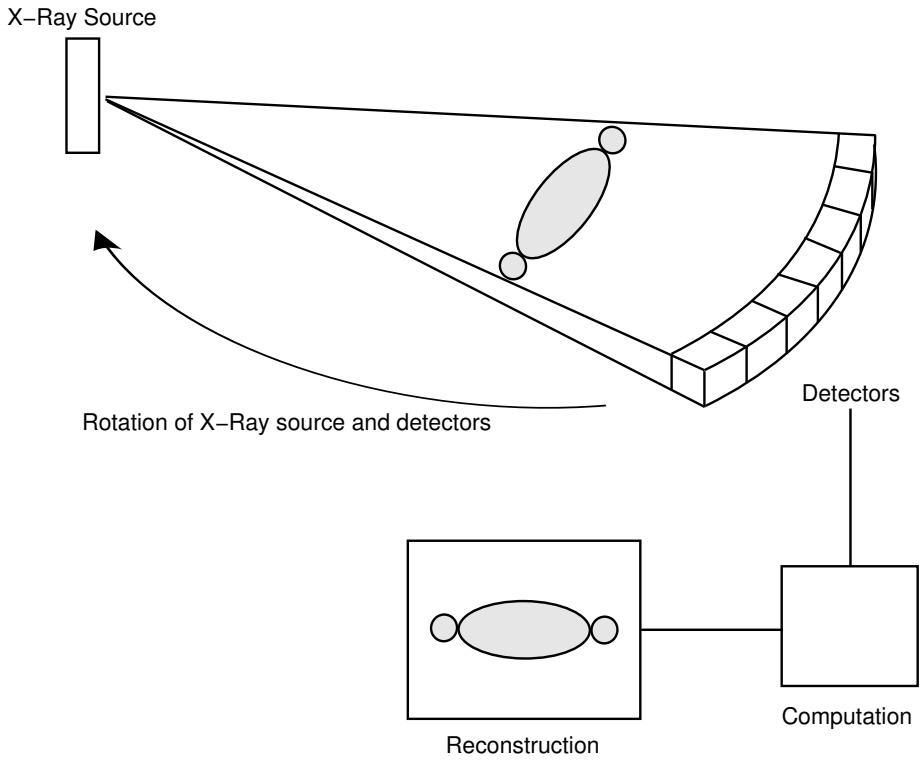

Figure 1.1: Imaging a 'slice' of body in a CT scan

compounds under consideration are labeled with a special radioactive agent, such as ^{18}F or ^{13}N, which emits positrons under radioactive decay. This property is important for using the PET scanner, as not all radioactive substances fulfill the demands required for PET imagery.

The positron is the anti-matter counterpart to the electron, and therefore has the same mass as the electron but the opposite charge. When a nucleus undergoes positron decay, the result is a new nuclide with 1 fewer proton, as well as the emission of a positron and a neutrino:

$$ {}^{A}_{Z}X \rightarrow {}^{A}_{Z-1}Y + e^{+} + \nu + Q \tag{1.1} $$

with X as symbol of the chemical element to which the nucleus belongs, Z is the atomic number, A is the atomic mass number i.e. sum of positrons and neutrons (which is also reduced by one after the decay) and Q is the energy released in the process [98]. A list of commonly used elements for PET studies is given in Table 1.1.

As a positron passes through matter, after losing enough energy and having traveled a distance in the neighborhood (depending on the initial positron energy, see Table 1.1), it will annihilate with a nearby electron and produce gamma quants:

$$ e^{+} + e^{-} \rightarrow \gamma + \gamma \tag{1.2} $$

Conservation of energy and momentum dictate that two photons (gamma quants) are emitted in opposite directions, each with an energy of 511 keV as shown in figure 1.2. These gamma quants reach the detectors and produce small light pulses in the detector

Table 1.1: Some commonly used radionuclides in PET imaging

Isotop	Element	Common compound	Half-life	Energy [KeV]	Range [cm]
^{124}I	Iodine		4.176 days	1.53, 2.14	
^{18}F	Fluorine	F-Glucose	109.77 min	634	1.0
^{11}C	Carbon	CO_2	20.39 min	961	1.1
^{13}N	Nitrogen	Ammonia	9.965 min	1190	1.4
^{15}O	Oxygen	Water	2.04 min	1732	1.5
^{82}Rb	Rubidium		1.273 min	3150	1.7

Sources: [87, 96]

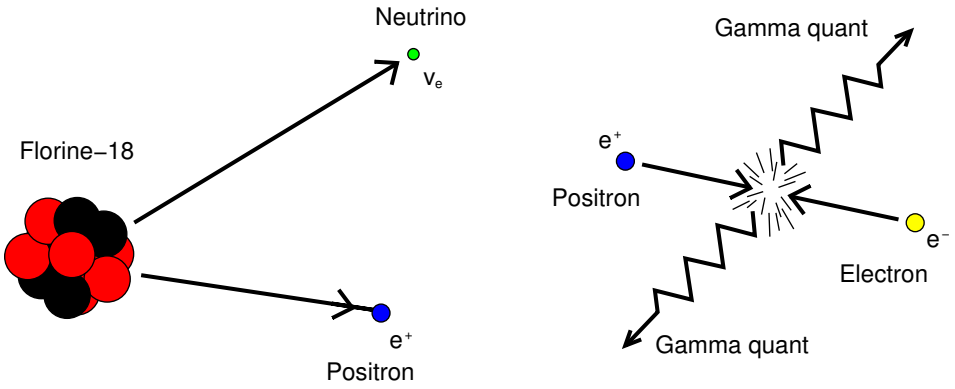

Figure 1.2: Production and annihilation of positrons in PET

material. Photo multiplier tubes (PMTs) are used to enhance these pulses and register them as an 'event'. The rate of events, however, is called 'counts per second' (or simply 'cps') and is a measure for the intensity of radiation emission from the object under study.

If two detectors 'fire' at the same time, we know that they probably belong to the same positron annihilation (but not always as we shall see later) and form a 'coincidence'. The exact position of the annihilation cannot be recovered due to measurement uncertainties. A line, rather a column, between the two detectors describes the area in which the annihilation could have taken place. This line is called the 'line of response' (LOR)[96].

The PET scanners thus consist essentially of a detector ring and a patient bed. The patient is injected with the radioactive substance. Depending upon the type of study this can be one hour before the actual scan, time which is needed for the body to absorb the substance with the marker and transport it to the organs and cells which are to be examined. In other cases this can be done while the patient is on the patient bed to observe the distribution of the marker and its metabolization.

Once the patient is on the patient bed and the scan is started, the patient bed is moved inside the detector ring. The activity is measured for some time and the patient bed is moved further to allow another part of the body to be scanned. Each such step is denoted by a 'bed position'. The whole scan thus consists of parts, whereby each part slightly overlaps with the previous one.

Figure 1.3: Biograph Sensation 16, the PET/CT scanner used in this study.

Basic knowledge about some steps of the image formation process in PET scanners and the terminology used for that is necessary for understanding the typical characteristics of the PET images and the difficulties attached with them. The image formation can be divided into two main parts:

- Formation of raw data.
- Reconstruction of the images.

We will describe these steps in some detail below.

1.2.1 Formation of the raw data

The storing of raw data from a PET scanner requires a number of steps as a pre-condition which include:

1. Event detection
2. Estimation of coincidence.

1.2.1.1 Event detection

Today, almost all PET scanners use special *scintillation* crystals to detect the gamma quants. The scintillators are transparent crystals that have the special property of emitting light when energy from particles or high energy photons is deposited in them. Scintillation crystals have some characteristic properties which include the stopping power i.e.

the distance that a high energy photon travels before it deposits its energy in the crystal, the brightness i.e. the amount of light they emit, and the decay time i.e. the interval needed to emit a light pulse [87].

An ideal crystal should have a large stopping power, so that most of the gamma quants passing through it may produce light pulses, it should have a large brightness value so that the emitted light signal is strong, and a short decay time so that it emits the light pulse quickly and becomes ready for the next event. Some of the commonly used scintillation crystals for PET scanners are given in Table 1.2. The scanner used in this study contains LSO crystals which have good density properties and a very high brightness value together with a short decay time.

Table 1.2: Some commonly used crystals in PET scanners

Crystal (common name)	Density (g/cm^3)	Brightness value (photons/MeV)	Decay time (ns)
NaI:Tl	3.67		230
$Bi_4Ge_3O_{12}$:Ce (BGO)	7.13	9000	300
Gd_2SiO_5:Ce (GSO)	7.71	8000	60
Lu_2SiO_5:Ce (LSO)	7.4	26000	40

Source: [87, 96]

Instead of using a PMT for each crystal, a number of crystals are combined together to form a block which is linked to four PMTs. Special logic is than used to find where the scintillation has taken place. The principle of this logic is shown in figure 1.4. The presence of this feature leads to the so called 'block effect', which is the result of errors in the readout system of the PMTs.

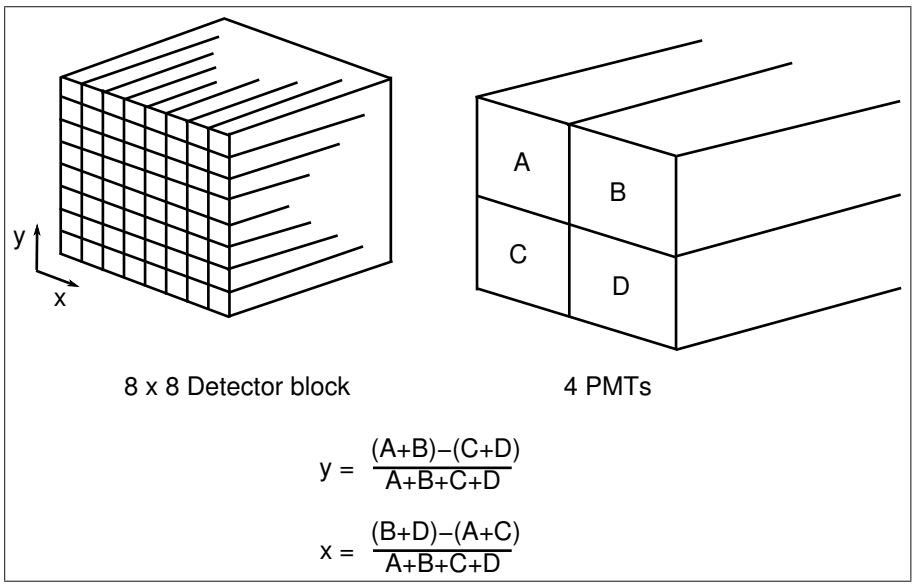

Figure 1.4: Block decoding, crystals connected to a smaller number of PMTs, Source:[107]

Only a fraction of the events can be detected in these crystals, as most of the gamma-quants simply leave the scanner without passing through the detector ring, or they pass through the detectors without scintillation or get absorbed in the body or get scattered. The number of events detected is typically less than 0.1% of the total possibly detectable events [96].

1.2.1.2 Estimation of coincidence

Two conditions are necessary to detect a coincidence: first the energy of the events should be within a window centered around 511 keV, and secondly the time between two events should be less than a threshold (e.g. the time needed by light to travel through the diameter of the detector ring).

The first condition is met by measuring the light output from the crystals. Higher energies lead to higher light output. Thus the light output can be used to assess the energy of the photon that induced the scintillation process. The second condition is met by using special coincidence time windows. When an event is detected in a detector, a timer is reset. If another event is detected within the time window, both events are assumed to belong to the same positron annihilation and build a 'coincidence' .

Besides these 'true' coincidences , there are a number of 'false' coincidences. These include random and scattered events [96].

Randoms A coincidence is measured when two detectors are hit at the same time by two gamma quants. This can only be accomplished in practice by assuming all events within a short time window to be happening at the 'same time'. Thus some of the unrelated or random events might also get registered as true, where in fact they are not related to the same decay event. The PET data has to be corrected for these random coincidences before image reconstruction. This is done at the hardware level by sorting time-delayed events into separate sinograms and subtracting them from the image sinograms [12].

The relationship between true and random coincidences is given by: [107]

$$R_r = 2 * \tau_c * R_1 * R_2 \tag{1.3}$$

where R_1 and R_2 are the rates of events in both the opposite detectors and τ_c is the time length of the coincidence window.

Scatter A part of the emitted gamma quants is deflected from the usual path due to the compton scatter and thus leads to falsification in the calculation of the line of response, see figure 1.5. As the photons loose some of their energy in compton scatter due to the collisions, the scatter can be reduced by using a narrow window of energy. There are also statistical methods to model and thus to calculate the scatter effect [121, 122]. Typically the scatter fraction is given by:

$$SF = \frac{C_s}{C_{tot}} \tag{1.4}$$

where C_s is the number of scattered events and C_{tot} is the total number of events. In 3D mode (see section 1.3), which is the mode the scanner was used in this study, the scatter ratio is around 50% [121].

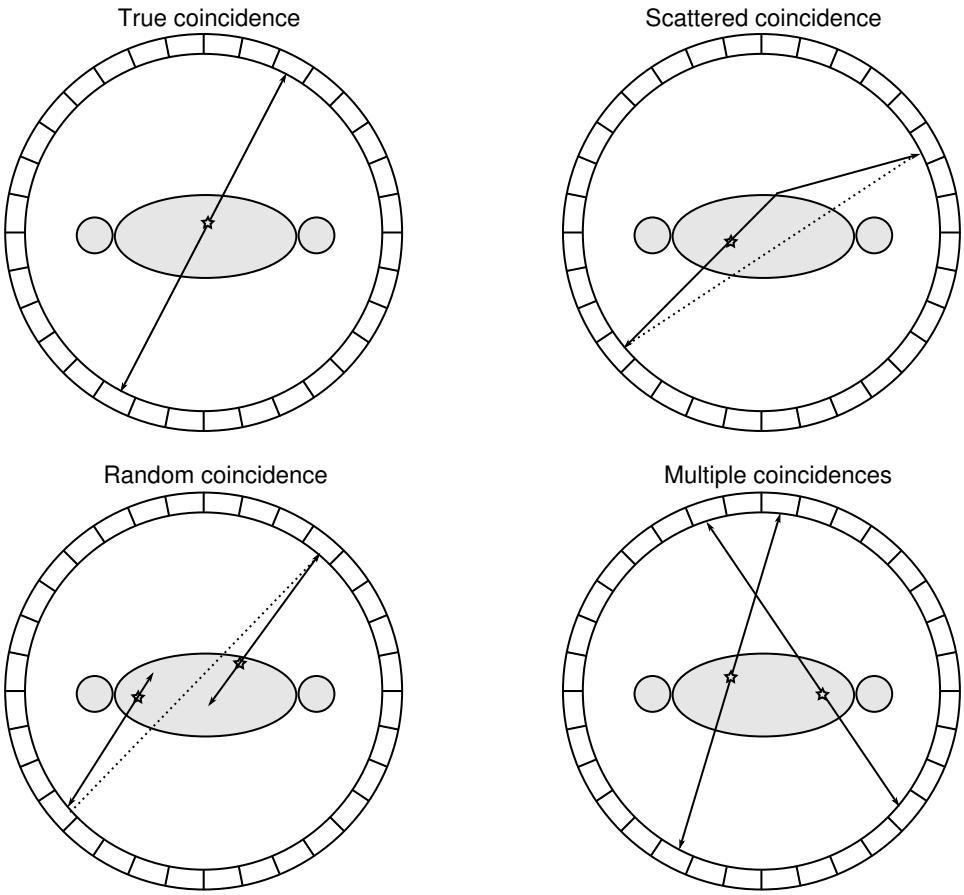

Figure 1.5: True, scatter, random and multiple coincidences.

Multiple events If only two detectors register a coincidence within the time-window used for measuring coincidences, the allocation of the line of response is easy. With increasing count-rates it is possible that more than one coincidences occur in the same time-window. In this case the allocation of the LOR becomes ambiguous. Normally, such multiple events are discarded [87]. Due to this reason some information is lost for the reconstruction of images.

1.2.2 Data formats

The raw data acquired by the scanners can be stored in two different formats. These are:

1. Sinogram format

2. Listmode format

This data is than reconstructed to give the images representing the distribution of activity in the object of examination. The reconstruction technique also depends upon the format the raw data is stored in.

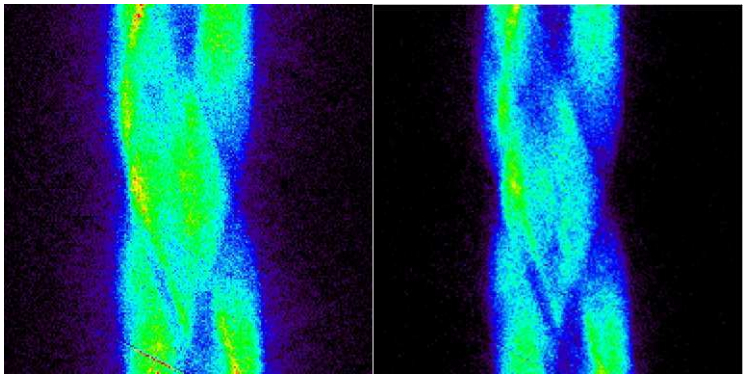

Figure 1.6: Scatter correction: After scatter correction (right) the activity outside the body is reduced because out of body activity comes mostly from scattered events.

1.2.2.1 Sinograms

In this format the coincidences are sorted with reference to the pair of detectors that define the LORs. The sorting criteria are the angle of the LOR and the distance of the LOR from the center of the detector ring, see figure 1.7. Every time an event is measured the value in the corresponding bin in the sinogram space is incremented by one.

As there are many detector rings, they build a 3D detector space. In this space rings very close to each other are sorted together to save space and time for reconstruction. A 'Michelogram' shows which detector combinations are sorted together (see figure 1.8).

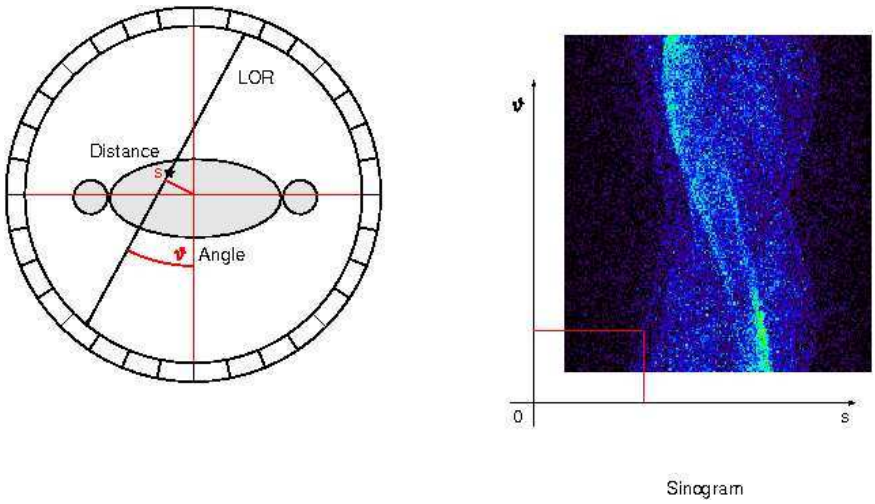

Figure 1.7: Left: A coincidence in a detector ring gives the line of response. Right: LORs from different detector pairs are sorted into a sinogram according to the angle and the distance of the LOR from the center of the detector ring.

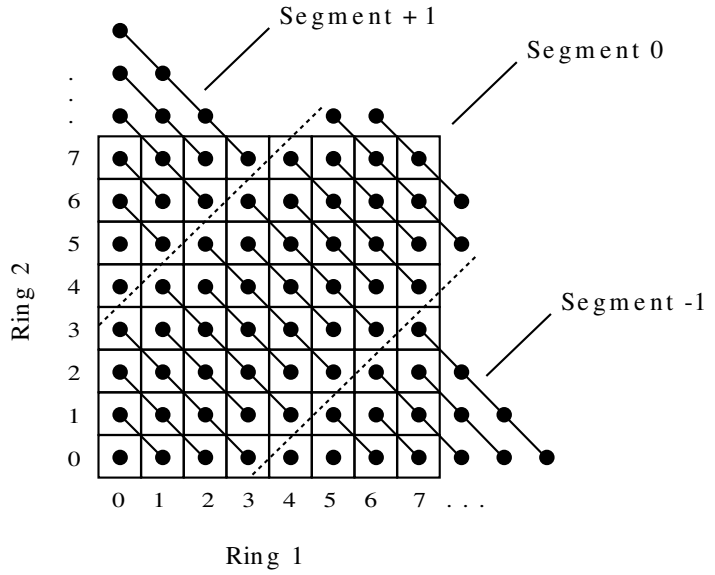

Figure 1.8: Part of a michelogram. Events detected in certain combinations, joined with lines, are sorted into same bins.

1.2.2.2 Listmode

In the listmode format the coincidences are not sorted into bins, they are rather recorded in the form of a list. In addition to the coincidences the total number of events (including those not belonging to any conincidence) is recorded. At pre-defined intervals (usually every milli-second) a time tag is also included.

A downgraded version of full listmode is also available which is called 32-bit listmode as opposed to the full 64-bit mode. In this mode, the events from some combinations of detectors are sorted together. The advantage of this mode is the smaller disk-space needed for storing the data. Additionally, the shorter time needed to write the data in 32-bit listmode format also reduced the system dead time (see section 2.1.2) as compared to the 64-bit listmode mode.

1.3 Acquisition modes

The modern PET scanners can be used in two different acquisition modes. They may be operated either in '2D' mode or '3D' mode. In 2D mode thin septa of lead or tungsten separate each crystal ring and coincidences are only recorded between detectors within the same ring or lying in closely neighboring rings (see figure 1.9). Coincidences between detectors in closely neighboring rings are summed or 'rebinned' to produce a dataset consisting of $2n + 1$ co-planar sets of LORs normal to the axis of the camera, where n is the number of detector rings. Such a dataset may be reconstructed into images using reconstruction algorithms as described in the next chapter.

In 3D mode, the septa are removed, i.e. retracted, and coincidences are recorded between detectors lying in all possible ring combinations. Usually more computationally intensive fully-3D image reconstruction techniques are employed to reconstruct the data from such acquisitions. The computational burden increases with the number of crystal

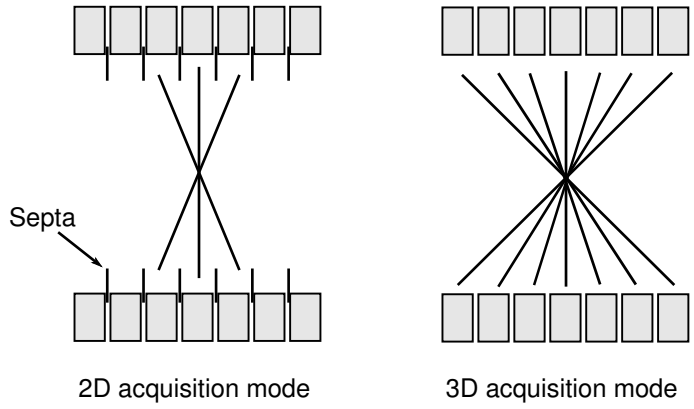

Figure 1.9: PET acquisition modes. In the 2D mode, only events nearly parallel to the detector rings are used. In the 3D mode events from all rings can be used.

rings used. For cameras with a large number of rings some degree of rebinning, i.e. recombining the closely neighboring LORs, may be applied to reduce the dataset to more manageable proportions - this process is known as 'mashing'.

1.3.1 Measured LORs

Removal of the septa allows the use of a much larger number of measured LORs for reconstruction. This increase depends on the number of crystal rings present in the scanner, a larger number of detector rings increases the number of LORs accordingly. Thus the probability that a particular event might be detected in the scanner increases. This probability is dependent upon the location of the event in the field of view (FOV).

1.3.2 Effect on scatter

In the presence of septa, only the photons scattered (see section 1.2.1.2 for scatter) in the plane of each detector ring (or near it) can be detected. When the septa are removed, it is possible to detect photons with a much greater range of scattering angles. As a result significantly more scattered events are detected in the 3D mode and thus the noise is increased.

1.3.3 Effect on randoms

When the septa are removed, the FOV for single events is increased. This can result in a significant increase in the number of random coincidences detected, particularly when imaging near organs which may contain significant amounts of activity, such as the brain, heart or bladder.

1.4 Factors limiting the resolution of PET

The spatial resolution of the PET scanners is limited by a number of physical factors related to the event detection. These include:

1. Positron range
2. Non-colinearity of gamma quants
3. Detector size

1.4.1 Positron range

As already stated, PET is based upon the emission of positrons. However not the positrons themselves, rather the gamma quanta which are produced by the annihilation of positrons are detected in the PET scanners. So what is actually located through back projection (LOR) is not the position of the emission of positron itself, it is rather the position of the annihilation of the positron. As the positrons are not immediately annihilated upon emission from the nucleus the distance the positrons travel before being annihilated results in error in determining the position of positron emission. This distance depends upon the energy of the positrons emitted by the radioactive isotops, the density of the material through which it is passing, the inelastic collisions it has with atomic electrons before annihilation etc. The energies and the half-lives of some isotopes commonly used in nuclear medicine are given in table 1.1. Typical average and maximum distance ranges for positrons emitted by some commonly used positron emitters are given in table 1.3.

Emitter	Max Range [mm]	Average Range [mm]
^{15}O	8.2	1.5
^{13}N	5.5	1.4
^{11}C	5.0	0.3
^{18}F	2.4	0.2
^{68}Ga	9.1	1.9
^{82}Rb	15.6	2.6

Table 1.3: Maximum and average ranges of positrons from some commonly used isotopes, Source:[97]

The positive part of the graphs in figure 1.10, calculated with the help of monte-carlo methods, can be well fitted with two exponential functions of the form:

$$P(x) = Ce^{-k_1 x} + (1 - C)e^{-k_2 x} \tag{1.5}$$

with the values for C, k_1 and k_2 as given in table 1.4 (see [59], also the correction of the values in Phys. Med. Biol. 45(2):2000 page 559).

Emitter	C	k_1	k_2
^{18}F	0.516	37.9	3.10
^{11}C	0.488	23.8	1.81
^{13}N	0.426	20.2	1.42
^{15}O	0.379	18.1	0.904

Table 1.4: Values of constants for equation 1.5

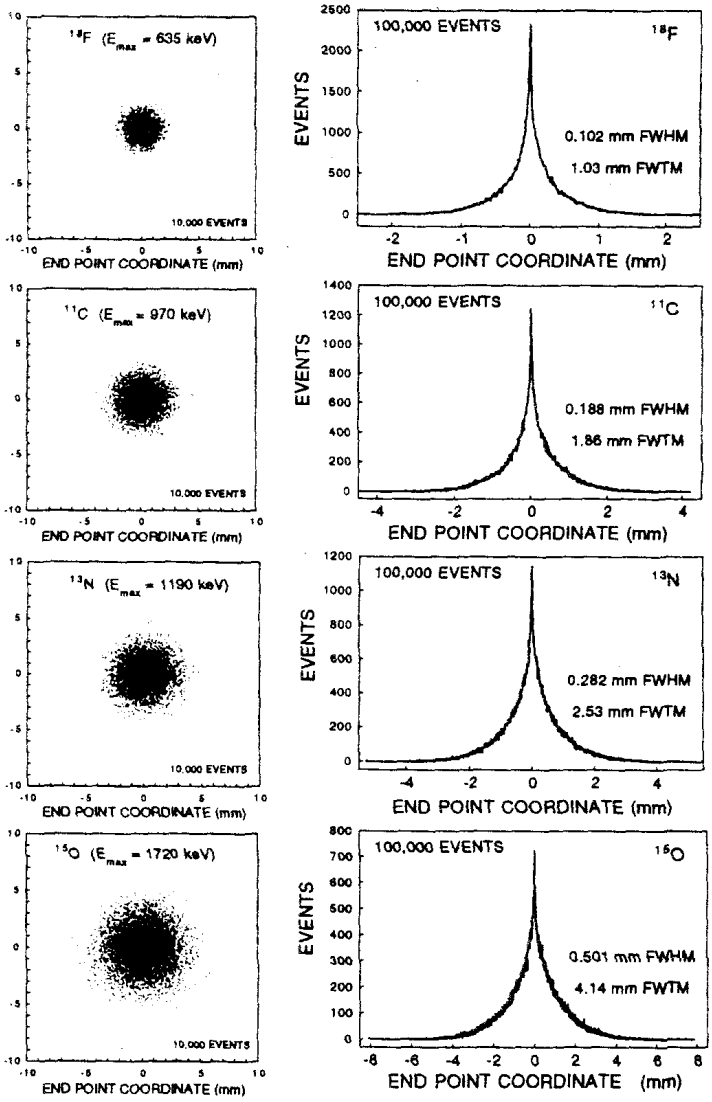

Figure 1.10: Spatial distribution of positrons from different isotopes, Source:[59]

We can now attempt to estimate how many positrons travel how far away from the point of emission in the PET. Integrating the equation 1.5:

$$\int P(x)dx = \frac{C}{-k_1}e^{-k_1 x} + \frac{(1-C)}{-k_2}e^{-k_2 x} \tag{1.6}$$

The equation 1.6, when calculated for the range x to ∞ and doubled (to account for the negative part of the graph), gives the part of positrons that fly past the distance x from the point of emission of positrons.

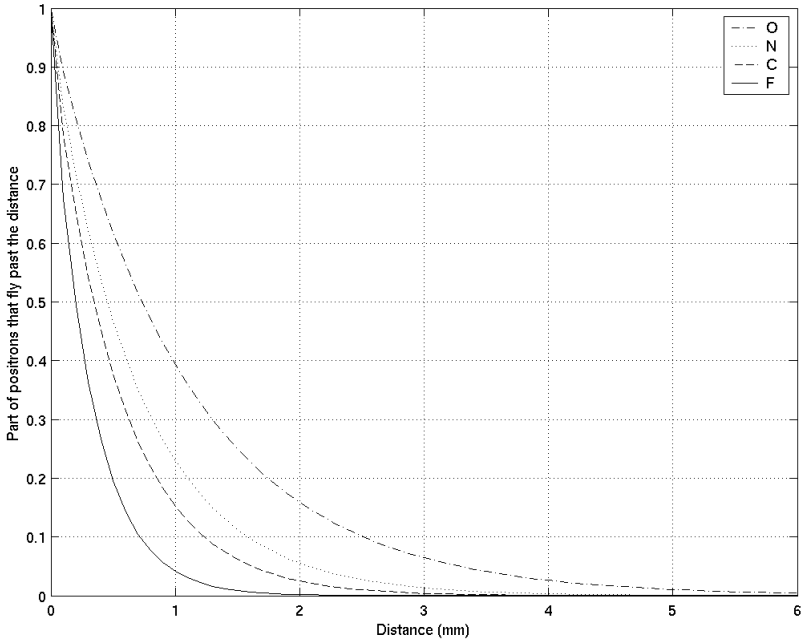

Figure 1.11: Part of positrons that travel beyond distance x from the point of emission

As expected the data for ^{18}F is best in this regard. Figure 1.11 shows that 39.30% of ^{15}O positrons exceed 1 mm before annihilation, whereas the same distance is covered by 23% of ^{13}N, 15% of ^{11}C and only 4% of ^{18}F positrons.

1.4.2 Non-Colinearity

As described earlier, the principle of coincidence is based on the assumption that the two gamma quants emitted at the positron-electron annihilation are anti-parallel to each other. This assumption is not always true because of different physical effects such as variation in the momentum of the positrons. This causes the emitted gamma quants to become non-colinear.

The principle of non-collinearity is shown in figure 1.12. The angel of deviation is at maximum 0.25°. The resulting blurring in the resolution will be [107]:

$$N = 0.0022 * D \tag{1.7}$$

where D is the radius of the ring and N is the loss in spatial resolution. The loss in resolution for common detector ring diameters of 80 cm to 85 cm will be 1.8 mm to

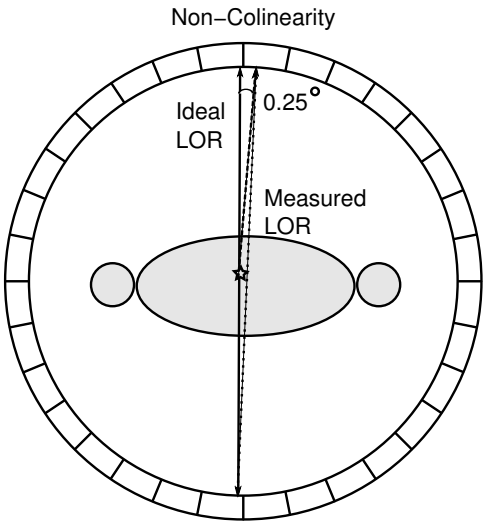

Figure 1.12: Non-colinearity occurs because the angle of emitted gamma quants varies by up to 0.25°.

1.9 mm. This effect is independent of the isotope used for the PET study and is only dependent upon the diameter of the scanner.

1.4.3 Detector size

The gamma quants emitted at the positron-electron annihilation are detected by scintillation crystals. However, it is not known where the gamma quants entered the detector thus the size of the detector limits the spatial resolution of the PET. All events detected in a crystal are assumed to have occurred at the center of the crystal. The error in resolution due to detector element size is given by [107]:

$$D = \frac{Detector\ Size}{2} \tag{1.8}$$

1.5 PET/CT

For a long time physicians used to overlay the results of PET and CT scans performed separately to identify and locate tumors or other anomalies. However, because a patient may not be positioned identically for both scans, the two images can be difficult to line up exactly, degrading the accuracy of the diagnostic information.

The combined PET/CT machines allow physicians to rapidly perform both scans in one session without moving the patient from one scanner to another. For this purpose usually the CT scan is performed first, which is followed by the PET scan. The patient remains on the patient bed during the whole session. The patient bed is moved in and out of the scanner for both scans automatically.

The hybrid PET/CT technology combines the anatomic data from a CT scan with the metabolic data from a PET scan to obtain a comprehensive snapshot of the internal organs and tissues of the body. The fused images provide far more detail in a single acquisition than conventional PET or CT scanners alone. With PET/CT, physicians are

able to more accurately detect tumors, evaluate reoccurrence and determine the patient's potential response to a therapy.

The special properties of PET/CT scanners include the following:

1. As the CT and the PET images are formed at two different speeds and modes of acquisition, different amounts of motion are present on both image datasets.

2. If the CT is performed in breath hold technique, which is commonly the case, the CT data does not correspond spatially to certain phases of PET data which is performed while the patient is freely breathing.

3. In PET/CT studies the CT images are also used for attenuation correction (see section 2.1.6). This leads to a new source of errors in attenuation due to motion artifacts.

1.6 Biograph Sensation 16

The PET/CT scanner used in this study is the Biograph Sensation 16 PET/CT Scanner manufactured by the Siemens Medical Solutions. The CT part of the scanner has 24 banks of parallel ultra-fast ceramic detectors with variable slice thickness of 0.610 mm, and a minimum rotation time of 0.5 s. The 50 cm transverse Field of View (FOV) can be extended up to 70 cm by means of a fitting algorithm.

The PET part of this scanner is a 3D-only scanner with 24 detector rings of 82.7 cm diameter. It consists of 144 block detectors, each block containing 8 x 8 LSO crystals. The crystals have a size of 6.45x6.45x25 mm^3 each. Each 8 x 8 block is attached to 4 photomultipliers. The axial and transverse FOVs are 16.2 and 58.5 cm respectively. This scanner system was supplemented with a special research package, 'Pico' electronics, by the manufacturer which contains faster electronics. The spatial resolution of the scanner is around 6.5 to 7.0 mm [69].

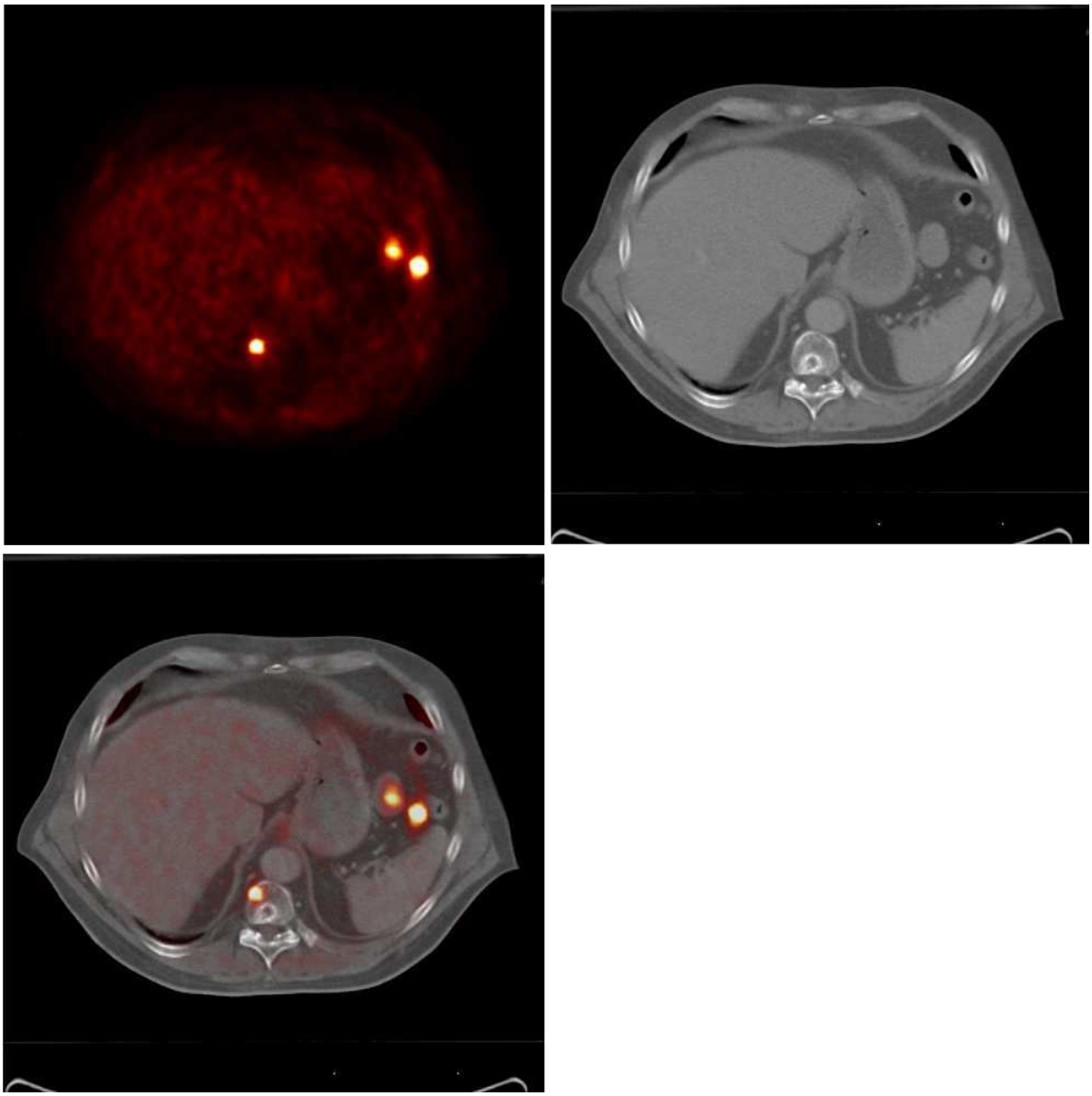

Figure 1.13: PET/CT. Top left: PET image, Top right: CT image. The fused image at bottom left shows both the metabolic information and the anatomic location of the lesion. Thus the exact location of the lesions becomes clear after fusion with the CT image.

Chapter 2

Image reconstruction

The PET data recorded and sorted in any form can be reconstructed with the help of special 'reconstruction algorithms'. The algorithm used in this study is described below. However, before the actual reconstruction of the acquired data can be performed, the PET data has to be corrected for certain distortions due to the image formation process.

2.1 Data correction

Distortions for which the PET data has to be corrected before image reconstruction include:

1. Decay correction
2. System Dead Time
3. Arc correction
4. Crystal efficiency normalization
5. Sensitivity due to scanner geometry
6. Attenuation correction

2.1.1 Decay correction

The substances used for PET imaging are radioactive and thus behave in accordance with the laws governing radioactive decay. With passing time the substance decays and therefore the intensity of the radioactive uptake decreases. This decrease in intensity is not a function of metabolism, rather a function of the radioactive isotope's half-life. The PET data has to be corrected for this apparent decrease in uptake for quantitative analysis. The decay correction becomes especially important in studies with long PET scans or with isotopes with short half-lives (see table 1.1). The law governing radioactive decay is given by:

$$N = N_0 * 2^{\frac{-t}{T}} \tag{2.1}$$

or equivalently:

$$N = N_0 * e^{\frac{-ln(2)t}{T}} \tag{2.2}$$

where N is the not yet decayed, N_0 is the total amount of radioactivity at the beginning of the measurement, t is the time passed since the beginning of the measurement, and T is the half-life of the isotope.

2.1.2 Dead time

During the process of gamma quant depositing its energy in the crystal, light emission, its amplification through PMTs, and its conversion into electrical signal no new events can be measured. If a new event takes place during this time the resultant signal of both events will be indistinguishable. This time denoted by τ is called the system dead time. The system dead time becomes more important when higher amounts of radioactivity are used.

Due to the system dead time, the observed counting rate (R_o) of the events is less then the true counting rate (R_t). The relation between both depends upon the question, if the system is paralyzable or not? In a paralyzable system each event induces its own dead time. Thus a succession of events, all taking place within the dead time of each other, would result in a long paralyzation of the system. The relation then will be given by:[106, 87]

$$R_o = R_t * e^{-R_t\tau} \tag{2.3}$$

In case of non-paralyzable systems, where the system dead time is not prolonged by events happening during the dead time, the relation is[106, 87]:

$$R_t = R_o/(1 - R_o\tau) \tag{2.4}$$

2.1.3 Arc correction

The LOR's placed at an offset from the center of the field of view become dense. To ensure an equidistant sampling of the PET signal this effect has to be corrected for by interpolation. This is called the arc correction of the data. It becomes more important with increasing detector ring radius. In modern iterative reconstruction algorithms, arc correction is usually not needed separately as the information about the position of the detectors is fed into the system-matrix of the scanner provided to the algorithm for reconstruction.

2.1.4 Crystal efficiency normalization

The ability of individual crystals to detect the gamma quants is not always same. With time some crystals may develop defects or loose efficiency otherwise. Thus the number of events detected in some crystals will be higher than others due to this effect. The PET data is corrected for this effect by using a normalization scan [87]. In this scan a known radioactive source is measured with the scanner. Due to efficiency differences the measured activity varies among the LOR's. These differences are used to calibrate the crystal efficiency.

2.1.5 Sensitivity

Annihilations taking place at the center of the field of view are at an advantage because they have a greater chance of being detected in the scanner than those happening at

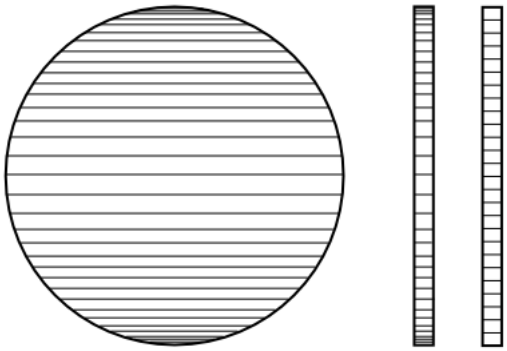

Figure 2.1: Arc correction. LOR's placed at an offset from the center of field of view become dense.

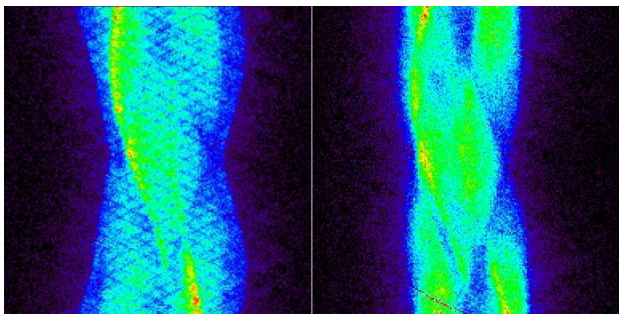

Figure 2.2: Normalization of PET data for crystal efficiencies. A sinogram without crystal efficiency normalization shows typical artifacts resulting from defective crystals (left). These are removed when the normalization for crystal efficiency is performed.

a short offset. This is due to the larger angle in which the gamma quants from an annihilation at the center can be detected. To correct the data for this effect a sensitivity map is utilized. This effect is only dependent upon the geometry of the scanner and is corrected by using a sensitivity map. An example of a sensitivity map is shown in figure 2.3.

2.1.6 Attenuation correction

The principle of PET is based upon the detection of gamma quants. In PET studies, some of the gamma quants emitted through annihilation of positron-electron pairs get attenuated or absorbed in the body. The degree of this attenuation depends upon the density of the tissue the gamma quants have to pass. Dense tissue, like bones, absorb a larger part of the photons than less dense tissue, like lungs. Therefore PET images without attenuation correction show apparently greater activity in areas with less density. This effect is corrected by scaling the number of photons registered in the scanner in accordance with the density of tissues.

In PET-only systems, a transmission scan is used for this purpose. A defined radioac-

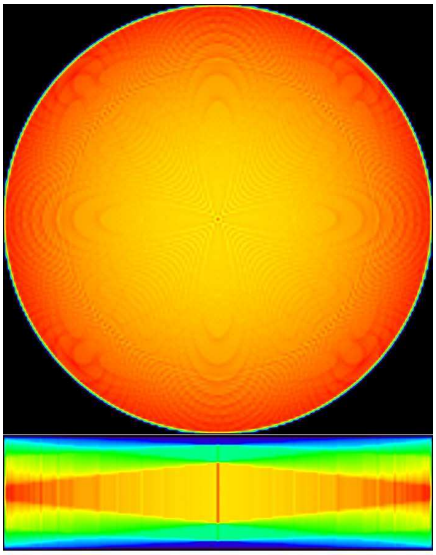

Figure 2.3: Sensitivity correction. Above: Transaxial view; sensitivity at the center of the detector tube. The detectors form a ring. Below: Coronal view; the detectors are present at the right and left edges of the image. Red points towards higher sensitivity and blue towards lower sensitivity.

tive source is rotated around the patient body at a defined distance. The radiation passes through the patient body and is detected at the opposite side. The decrease in the measured activity is used to correct the emission data. The transmission scan is performed before activity is injected into the patient[4].

In PET/CT systems the CT scan is also used for attenuation correction of the PET data as the CT scan provides the necessary density information[18, 49, 83, 84]. The information provided by the CT scan is first transformed to a μ-map by interpolating the CT data to an energy level of 511keV. This μ-map is than used to attenuate the PET data.

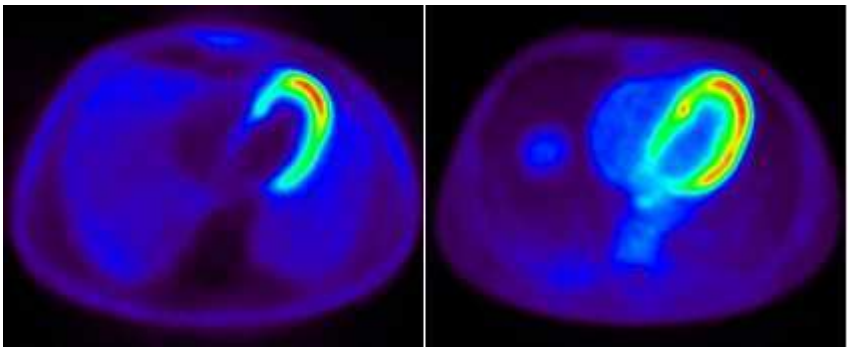

Figure 2.4: Attenuation correction, PET transaxial slice. Left: Image without attenuation correction shows high uptake in lungs and less uptake in heart. Right: The uptake differences have been corrected after attenuation was performed.

2.2 Reconstruction algorithms

After correction of the PET data for the effects described above, the images can be reconstructed with specific reconstruction algorithms. Many methods for reconstruction have been presented [74]. These include among others the inverse Radon Transform [75], Filtered Back Projection (FBP)[120], Maximum Likelihood Expectation Maximization (MLEM)[113] and its variants. In the following sections the radon transform, which is the basis of all tomographic projections, the FBP and the OSEM (a variant of the MLEM) algorithms will be described briefly. In this study only the OSEM algorithm is used.

2.2.1 Radon transform

The basis of all tomographic projections can be described by the radon transform which is named after Johann Radon. It is the integral transform consisting of the integral of a function over the set of all lines.

If a plane E in 3D space is given with:

$$E : x\sin\theta\cos\lambda + y\sin\theta\sin\lambda + z\cos\theta = \rho \tag{2.5}$$

or

$$E : \vec{x}\cdot\vec{\eta} = \rho \tag{2.6}$$

where

$$\vec{x} = \begin{pmatrix} x \\ y \\ z \end{pmatrix}, \quad \vec{\eta} = \begin{pmatrix} \sin\theta\cos\lambda \\ \sin\theta\sin\lambda \\ \cos\theta \end{pmatrix}, \quad |\vec{\eta}| = 1 \tag{2.7}$$

$$\tag{2.8}$$

The distance of E from the origin is:

$$\rho\vec{\eta} = \begin{pmatrix} \rho\sin\theta\cos\lambda \\ \rho\sin\theta\sin\lambda \\ \rho\cos\theta \end{pmatrix} \tag{2.9}$$

Then the radon transform is given by:

$$\mathcal{R}[f](\rho,\theta,\lambda) = \int_{-\infty}^{\infty}\int_{-\infty}^{\infty}\int_{-\infty}^{\infty} f(x,y,z)\cdot\delta(x\sin\theta\cos\lambda + y\sin\theta\sin\lambda + z\cos\theta - \rho)\,dx\,dy\,dz. \tag{2.10}$$

In the context of tomography the Radon transform data is often called a 'sinogram' because the Radon transform of a delta function is the characteristic function of the graph of a sine wave. Consequently the Radon transform of a number of small objects appears graphically as a number of blurred sine waves with different amplitudes and phases. Thus the radon transform describes the forward projection of an object through the scanner. Inverting the radon transform and applying it to the sinogram data should give the original distribution of activity in the object. However, this is practically not the case because of difficulties in numerical approximations.

2.2.2 Analytical reconstruction: FBP

The filtered back projection (FBP) is one method of reconstructing PET images which is widely appreciated for its speed. It was the first reconstruction algorithm to be used. This method provides accurate estimation of the radiotracer distribution when projection data are noise free. The basic principles are to perform the Fourier transform of angular projections, apply the ramp filter in the frequency domain, uniformly distribute the filtered data over the reconstructed matrix, and then to antitransform. This method is simple to implement and fast in performing sections reconstruction. However, the ramp filter used to eliminate the artifacts and improve spatial resolution also amplifies the noise component, which is particularly important at low counting statistics. To compensate for these effects, low-pass smoothing filters are applied to cutoff frequencies higher than a certain limit, thereby producing more blurred images and worsening spatial resolution.

The 2D FBP algorithm can be given as:

1. Take 1D Fourier transform of the first angle (row) in the sinogram
2. Multiply it with the filter function
3. Calculate the inverse Fourier transform
4. Backproject the filtered and modified projection
5. Repeat the procedure for all angles

For backprojection, the LOR defined by the detector-pair is selected and its path through the scanner is calculated. For each voxel intersected by the LOR the total number of counts measured for that LOR is weighted in accordance with the path length of the LOR through that voxel. Thus a voxel intersected in the middle gets a higher weight than a voxel whose corner is intersected by the LOR.

For the 3D case, which is the object of this study, the 2D FBP is extended and the following algorithm is used (see [76, 87] for details):

1. Extract 2D sinograms ($\theta = 0°$)
2. Reconstruct the 2D sinograms with 2D FBP
3. Forward project the image volume to calculate the missing LORs
4. Extract 2D projection data for θ, λ
5. Take 2D Fourier transform of the projection
6. Multiply with the 2D filter function
7. Calculate the 2D inverse Fourier transform
8. Backproject the filtered and modified projection
9. Repeat for all angles θ, λ

2.2.3 Iterative reconstruction: OSEM

Iterative algorithms are based on the attempt to maximize or minimize a target function determined by the particular algorithm used. The target function is reached through several iterations. A major advantage of this type of algorithms is the possibility of incorporating different a priori information, such as noise, attenuation, or characteristics of detector nonuniformity, for more accurate image reconstruction. However, the inclusion of additional parameters means increase in the processing time.

Depending upon the method, different numbers of iterations are required to reach the target function but too many iterations can lead to noise amplification with image quality deterioration. Different iterative algorithms are present in literature, some based on the methodologies of numeric linear algebra and others based on statistical approaches. To the latter class belongs the maximum-likelihood expectation maximization algorithm (MLEM), which is able to estimate more accurate radiotracer distribution. The MLEM is based on the maximization of the logarithm of a Poisson-likelihood target function.

The algorithm attempts to obtain a reconstructed slice whose forward projection generates a projection dataset almost equal to the original one. The main feature of this reconstruction algorithm is to update the image during each iteration by using a multiplicative factor assessed as the ratio between the original acquired projections and the newly estimated ones (see figure 2.5). Advantages of this iterative method are very low noise amplification without loss of spatial resolution and the fact that all reconstructed values will be positive because a non-negativity condition is imposed on the original data. The main disadvantage is the large number of iterations required to converge to an optimal solution and the long processing times, hampering its applicability in clinical routine.

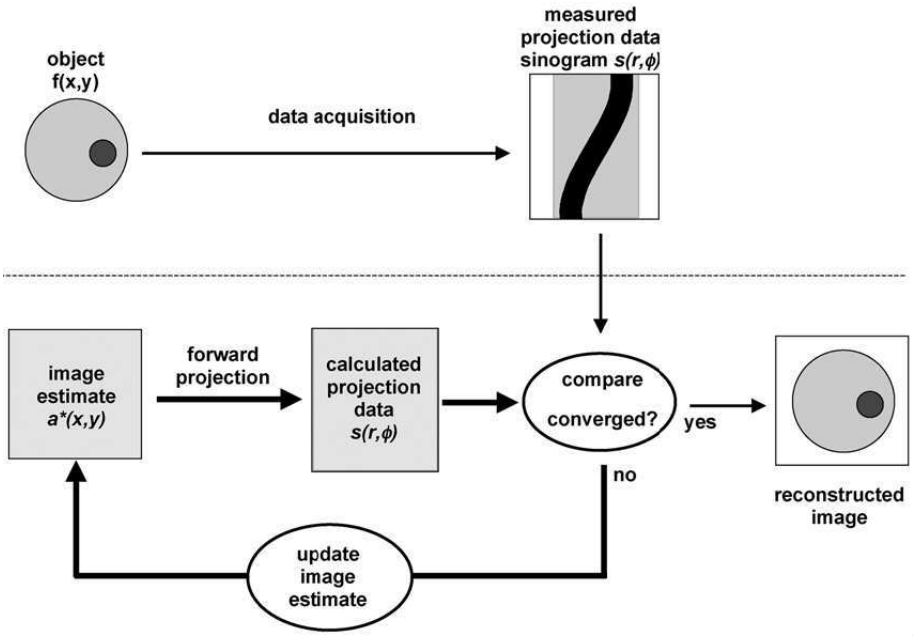

Figure 2.5: General scheme of iterative methods.

To overcome the problem of slow convergence rate, the ordered-subsets expectation

maximization (OSEM) algorithm was proposed in 1994, which is now the most widely used iterative reconstruction method in whole-body PET imaging. The OSEM is a modified version of MLEM (the target is still the maximization of the log-likelihood function) with the main difference being that projections are grouped into subsets having projections uniformly distributed around the volume to be imaged. Within each iteration the target function is updated as many times as the number of subsets, proportionally accelerating convergence [76, 87]. An optimization of subsets and iterations number is required when the method is applied to real, noisy data, because the algorithm can cycle without converging to the MLEM function.

More recently the row-action maximum-likelihood algorithm (RAMLA), which in some extension can be considered a special case of OSEM requiring sequences of orthogonal projections and a relaxation parameter to control updating of the log-likelihood objective at each full iteration cycle, has been proposed. Theoretically, these two conditions should guarantee a faster and better convergence to MLEM solution than OSEM [87].

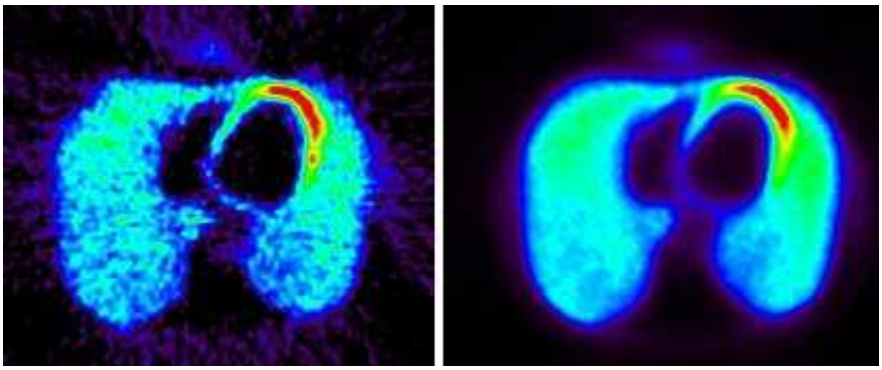

Figure 2.6: Comparison of the FBP (left) and the OSEM (right) reconstruction algorithms.

2.2.4 Listmode reconstruction

If the PET data is acquired in listmode format, the reconstruction can be done in two ways. Either the listmode data can be converted to sinogram space and the usual sinogram based reconstruction algorithms applied to it. The other possibility is to develop special algorithms that can be directly applied to the listmode data [94].

Denoting λ_j^{m+1} as the image intensity in voxel j at the $m+1$th iteration and p_{ij} as the probability of an event in voxel j being detected along the LOR i the Listmode reconstruction algorithm can be given as:

$$\lambda_j^{m+1} = \frac{\lambda_j^m}{\sum_{i=1}^{I} S_{ij}} \sum_{k=1}^{N} P_{i_k j} \frac{1}{\sum_{b=1}^{J} P_{i_k b} \lambda_b^m} \tag{2.11}$$

where i_k is the LOR along which the kth event is detected and N is the number of measured events. The factors S_{ij} are the geometrical probability of an event in voxel j being detected and are called the sensitivity correction factors. The normalization and attenuation can be built in this algorithm by weighting the voxels.

Chapter 3

Problem

The problem with which we are confronted in this study is that of respiratory motion in PET studies. Different kinds of motion are possible during PET/CT data acquisition. These include:

- Patient motion, which includes the motion of the patient during the CT or the PET scan as well as the motion of the patient between the two scans.
- Cardiac motion, during which the heart of the patient undergoes a complex sequence of contraction, dilation and torsion.
- Respiratory motion, which inflates and deflates the lungs and thus enables the patient to inhale and exhale air.

Before proceeding further, it will be useful to distinguish between two types of motion, the rigid motion and the non-rigid motion. A motion is considered rigid if the position of the organ as a whole changes, either through translation and/or rotation. The organ retains its shape and form under rigid motion. If the structure of the organ is deformed in addition to changing its position then the motion is considered non-rigid. Both the respiratory and the cardiac motions are non-rigid as the heart and the lungs not only show displacement and rotation, but also contract or expand during a cycle.

3.1 Cardiac motion

The cardiac motion in human thorax is due to the pumping motion of the heart. The cardiac motion that is independent of body (torso) motion is almost exclusively vertical and commonly consists of a slow upward drift that has been termed *upward creep*. Several reports have suggested that vertical cardiac motion (drift or bounce) is by far the most common type of motion. Subtle changes in respiratory pattern related to recumbence, more so than to stress may also play an important role in the etiology of upward cardiac creep[36].

The different phases of motion that the heart undergoes during its cycle can be recognized with the help of an ECG-signal (see figure 3.1). As this study is primarily concerned with respiratory motion correction, cardiac motion is not the focus of interest.

The displacement of heart due to motion is estimated to be 25 mm [112]. This motion has major impact on the quantification of cardiac studies in PET imaging. The impact

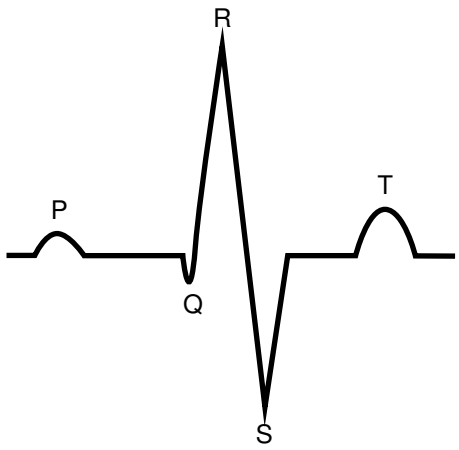

Figure 3.1: Electrocardiogram

on other organs is small as compared to the respiratory motion, described below. The interested reader is referred to studies such as [90, 108] etc. for further information.

3.2 Respiratory motion

The second important source of motion in the human thorax is the motion due to respiration. When air in inhaled the diaphragm moves down and the lungs expand along with the ribs and chest to allow for the increase in volume. At expiration a reversal of this motion takes place, the lungs contract and the diaphragm moves up. Due to this motion, some of the other organs in the thorax are also effected and move along with the lungs and diaphragm.

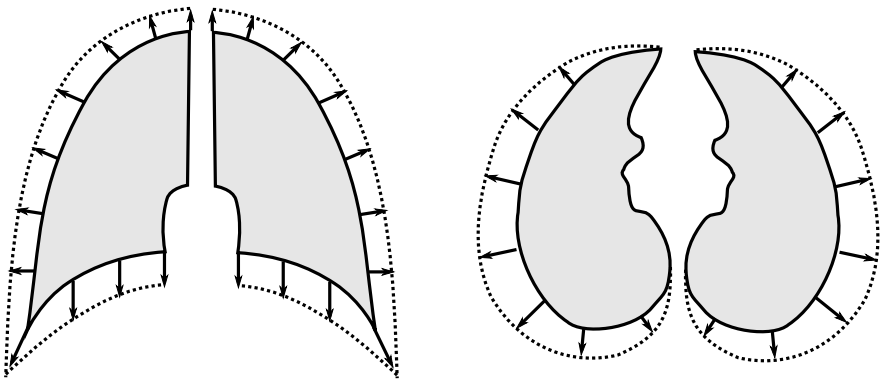

Figure 3.2: Movement of lungs during breath intake. Left: coronal view, right: transaxial view.

It is to be noted that during the inhalation phase, when air is taken in, the lungs expand in all direction and the lung base together with the diaphragm moves downwards (caudal-direction). During exhalation phase, when air is breath out, the lungs and the diaphragm move upwards (cranio-direction).

Until recently the effects of motion upon the functional images has been relatively small as compared to the image blurring due to attenuation effects, scatter etc. However with the advance in the estimation and removal of the effects of attenuation and scatter in medical images, the movement of organs due to respiration is becoming more and more important.

The diaphragm is a muscular mass attached to the bottom of the thoracic cage and moves downward like a piston when it contracts. During quiet expiration the pressure to force air from the lungs comes from the elastic expansion of the lungs and chest wall. This is significant in matching CT, and MR or PET studies, where the CT scan is acquired while breath is held, whilst MR and PET scans are acquired during normal respiration.

In a Magnetic Resonance Tomography (MRT) study the diaphragm motion due to respiration was found to be about 15-20 mm [100]. Due to this prime motion displacements of up to 23 mm are present in tumors depending upon their location. The heart and diaphragm respiratory motion was found to be approximately 15 mm on average in supine position (horizontally laying) and upto 20 mm in some patients [112]. The total range of the diaphragm motion in patients was found to be from as little as 4 mm to as much as 38 mm [114]. The respiratory motion of the diaphragm is also physically directly connected with the motion of the liver. Studies have shown that the liver tumors undergo a motion in the range of 7.5 to 17.5 mm due to respiration [8].

Table 3.1: Maximum respiratory motion of different organs

Organ	Motion [mm]	Reference
Diaphragm	38.0	[114]
Heart	23.5	[72]
Liver	25.0	[11]
Spleen	25.0	[11]

3.3 Problem of motion in PET/CT

The motion of inner organs in the thorax leads to two sources of possible artifacts in PET/CT. Firstly, wrong attenuation correction (Fig 3.3, see section 2.1.6 on attenuation correction) and secondly, image blurring (Fig 3.4). The respiratory motion of the patient does not lead to severe motion artifacts because both the PET emission as well as the PET transmission data contain the same amount of respiratory motion. However, the image blur remains. The problem of respiratory motion is enhanced in PET/CT scanners, which use the computed tomography (CT) data for attenuation correction [49, 26]. As the CT is acquired much faster (in seconds) than PET, it represents an almost instantaneous snapshot in comparison to the PET images. Therefore a part of the PET data is not in spatial correspondence with the CT data and will be wrongly corrected for attenuation (e.g. activity from heart may be corrected with lung density).

The second disadvantage of motion is image blur. The motion of the source of radioactive emission causes blurring on the PET images proportional to the magnitude of the motion. This leads to loss of contrast. It has been shown that the motion of lungs during the PET acquisition may lead to wrong staging of tumors [35]. Small tumors may

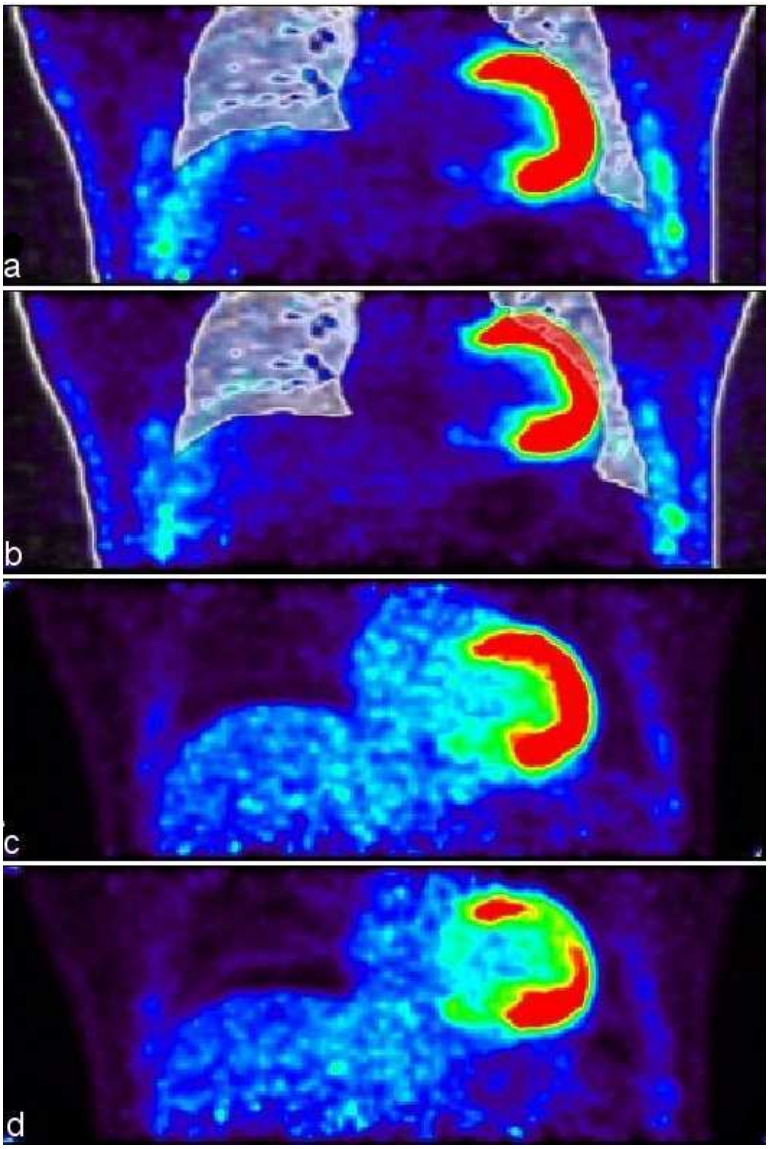

Figure 3.3: The problem of attenuation correction in PET/CT images (coronal slice of a patient dataset). a) The CT contour (white) laid over the original PET data (colored) shows that both correspond to each other spatially, b) In another respiratory phase, PET and CT data do not correspond to each other spatially. c) Attenuation correction of PET data from a) does not show any artifacts as PET and CT data are in correspondence, d) wrong attenuation correction occurs when PET and CT data do not correspond to each other b) and this results in large artifacts.

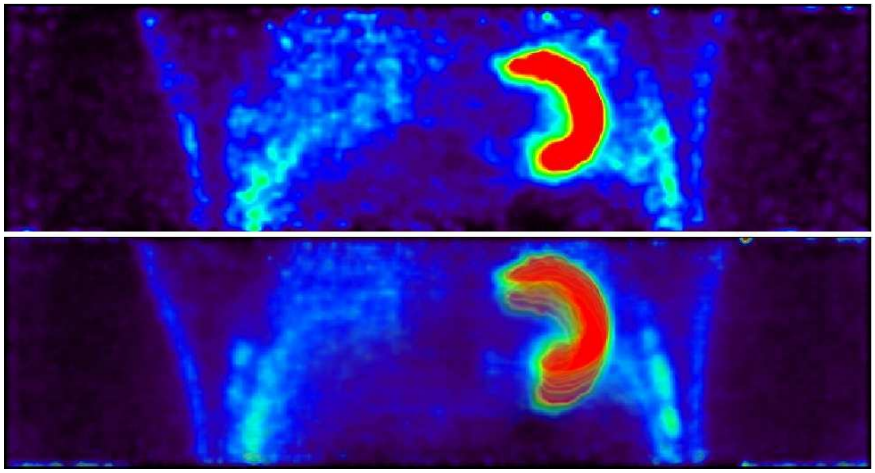

Figure 3.4: Above: single respiratory phase without motion, below: all respiratory phases superimposed artificially by image blending. The extent of respiratory motion is visible in the left heart ventricle (red in color). The level of noise in the single phase image is much higher due to the lack of statistics. All images were reconstructed with an OSEM algorithm.

even succeed in evading detection [85].

Thus the attenuation correction of PET images with CT may lead to significantly inaccurate localization of lesions [80], wrong attenuation correction, misstaging of tumors and wrong calculation of standard uptake values [73].

3.4 Previous attempts on solving the problem

Previous attempts to solve the problem of motion in pulmonary PET imaging largely followed the strategy of externally monitoring the motion of the patient with the help of external markers and video cameras. The images are then sorted in accordance with the motion of these external markers. Nehmeh et al [78] used an external block which is fastened to the patient's abdomen. The movement of this block monitored with video cameras and the position of the block is used for sorting the data into different gates. Only the first gate is used for reconstruction. Such a procedure reduces the motion on the images in each gate by some extent, however, most of the information is lost in the unused gates. To get the same statistics as in the ungated images, a proportionally larger amount of the radio-tracer must be administered to the patient which is not an option under normal clinical circumstances.

Nehmeh et al recognized this problem and proposed another method in [79]. This method is based upon the use of a radioactive ^{18}F-FDG point source which is present at the end of a low density plastic rod. This rod is fastened to a block of Styrofoam which is again attached to the abdomen of the patient. The whole apparatus is placed in a way so that the radioactive point source extends into the plane of the lung lesion. The data is acquired into 200 frames of 1 second each. A ROI is placed over the point source in any one frame by the user. Now all other frames in which the point source falls within the same ROI are selected. The corresponding sinograms of the selected frames are then summed up and the image is again reconstructed with this new sinogram. This method

utilizes more information then the first one. However, information on all frames in which the marker lies outside the ROI window is lost. Moreover, there is no motion correction, it is rather a selection of frames which are 'good'. Lastly, the position of the lesion has to be known *a priori*. Both of these methods are thus not a real solution to our problem.

Attempts were made at motion correction in PET images of other organs too, such as brain [88] or heart studies [50], but they represent a different case from ours. Head motion is not a periodic motion and it can be detected easily with the help of the skull. Also the motion inside the skull is uniform and only rotational or translational in nature. Even then, Picard et al [88] and following them Fulton et al [39] used video cameras to monitor the skull position externally. Even more recent attempts at motion correction in brain studies are based on external monitoring [16].

Klein [50] achieved motion correction in heart studies by using deformable elastic membranes as a model. But his method is applied to heart only as it attempts to simulate the elasticity of the heart muscle. Moreover it requires segmentation of the heart prior to motion correction, as the underlying equations change for each organ and fluid in accordance with the tissue type and its physiological properties. Lastly, it can neither motion correct different organs at the same time, if they are not already segmented and underlying elastic properties defined, nor can it motion correct organs which do not behave as elastic membranes. Lungs are an example in case, as they behave more like a filled and expanding balloon rather then a deforming membrane.

Another method, similar to the above one, was proposed by [124] et al. The main drawback of their method is again the use of elasticity properties of the tissue. For this the authors propose to use either tensile tests or to use special änchortesting images, made under laboratory conditions with no noise, with landmark correspondence to find out these physical properties. The accuracy of the method will critically depend upon the accuracy of this landmark correspondence. The method is 2D and no data on its qualitative goodness is provided, nor is it compared with any other method. Another drawback is that a global registration is a prerequisite to perform this method.

An elastic deformable registration method was proposed by He et al [46]. This method is essentially similar to a global optical flow method. The method uses four conditions to perform the deformable registration. All four conditions, intensity similarity, incremental transformation, smoothness, and error minimization are used in global optical flow methods. Thus the method suffers from the same disadvantages in presence of heavy noise as do other similar optic flow methods.

There have also been some attempts at correcting the motion in PET studies in the pre-image, i.e. directly in the sinograms [62] or by rebinning the listmode data [16]. The first method corrects the motion by detecting high intensity nodes (if they are present in the images) in the sinogram and can correct only the inplane motion via scaling, whereas the second method needs video monitoring with external markers to find the position of the chest and re-sort the bins accordingly.

Studies which try to estimate the motion of the organs on gated CT images, such as those by Manjeshwar[68], Qiao[92], Mair and Gilland[67], are not of further interest here, because they need to gate the CT phase of the scan, which goes hand in hand with an increase in radiation dose for the patient which is not justifiable for most routine patients. Moreover, these studies derive the motion information from the CT data, the noise and image content of which is much better than PET images. Our study, on the other hand, proposes a PET-images-only based method which does not causes an increase in radiation

to the patient and thus is applicable to all patients.

3.5 Our Approach

As the respiratory motion is continuous during the PET acquisition, it is proposed that as a first step the PET data be divided and re-sorted in a way which allows for reconstruction of many frames each with minimal amount of motion. Methods for doing this type of re-sorting are called 'Gating' methods. The gating methods are described in detail in the second part of the present study. Such an approach leads to reducing the amount of motion on the PET images, however, it leads to a corresponding increase in noise on the images. It should be re-called that the PET images are already very noisy. Thus selecting the best corresponding frame from many frames is not the complete solution to our problem as it will lead to good spatial correspondence between the PET and CT images but bad statistics on PET images as well.

This is where the second step of the solution helps. It is proposed to deform the gated images non-rigidly to the 'best' spatial position. This will allow for addition of all gates to obtain the full statistics along with good spatial correspondence with the CT images. Specific 'Optical Flow' methods are proposed for this task, which will be described below in the third part of the study.

The proposed method is applicable to the PET data without any prior segmentation or assumptions on the elastic properties of the different types of tissue present in the body. It encompasses all PET data without loosing any statistics. The proposed optical flow method is a hybrid local-global method which combines the advantages of both types of methods as described in the concerned chapter.

Part II

Gating

Chapter 4

Gating Methods

Gating is one of the methods used to reduce the effects of motion. In this approach the PET data is sorted into different gates with respect to a reference signal. This can be the respiratory signal or the ECG (Electrocardiogram) signal. Each gate thus contains only a part of total motion and will have reduced motion blurring. On the other hand, the gates contain only a part of the total number of events detected in the scanner which leads to more image noise. In this part of the study, we aim to analyze and compare different respiratory gating methods in PET/CT to assess the quality and applicability of different methods for motion detection.

Other methods of avoiding motion artifacts include usage of slow CT [119] or the use of an averaged CT [83]. The first method uses a very slowly rotating CT source, so that the breathing motion is averaged over the respiratory cycle in the acquired dataset. In the average CT method, the patient data is acquired for over one respiratory cycle for all positions at high speeds. Very low radiation doses are used in this process, so that the total dosis of radiation to the patient is not much higher than normal CT scans. However, in these methods the respiratory motion blur is still present on the images. The same amount of blur on PET and the CT data helps avoiding the drastic motion artifacts, but it cannot remove or reduce the motion itself. Thus we have opted for respiratory gating in this study, which actually divides the PET data into smaller parts, each with reduced motion.

The most commonly used methods for acquisition of the respiratory signal include video monitoring and the use of pressure sensors. In the first method a marker is fastened to the body of the patient and its motion, which is caused by and correlates to the breathing motion, is monitored by a video camera [77, 78, 60, 104, 42]. The second system is based on a pressure sensor attached to a belt which is placed around the waist of the patient. With the motion of the abdomen due to breathing, the pressure on the sensor is increased or decreased. This change in pressure is registered as the respiratory signal [29, 51]. Other methods of gating include the use of a temperature sensor, which controls the temperature of the breath and thus marks the start of each breathing cycle [10], use of radioactive markers [79] that are placed inside the field of view and thus visible on PET images, or the use of piezoelectric crystals [71].

Respiratory gating, i.e. sorting the PET data with respect to respiratory phase, can be done in two basic ways: (1) time-based and (2) amplitude-based[25]. The time-based methods divide the respiratory signal with reference to time in each breathing cycle. They sum up the PET data from corresponding time phases of each breathing cycle together.

However, the magnitude of respiration is not taken into account. Therefore maximum inspiration phases from two different cycles may be added together, even if they do not correspond to each other with respect to the position of the lung base, if they fall into the same time phase after beginning of the breathing cycles (see figure 4.1 for illustration).

The amplitude-based methods divide the respiratory signal with reference to the magnitude of the breathing signal. The idea is to sum up the PET data from different respiratory phases which correspond to the amplitude of the breathing signal. Thus maximum inspiration phases from different cycles will only be added together if they reach the same magnitude in breathing. It has been recently shown on phantom data that the amplitude-based gating is better than time-based gating with regards to capturing the motion of the organs [118]. Both of these primary methods can be further subdivided into two ways depending upon the method of selecting the gate width i.e. variable and equal. In variable gating methods, the width of each gate is calculated individually whereas in equal gating methods the width of all gates is equal. Thus variable amplitude based gating means that the gates are selected based upon the amplitude information where each gate width is variable. Equal time based gating, similarly, means that gates are selected with reference to time information and all gates have equal widths.

As the aim of this study was to evaluate and optimize different gating schemes on real patient data, a comparison of different time and amplitude based methods was performed with respect to their noise properties and their accuracy with respect to capturing the respiratory motion. The main goal was to find a gating method which best represents the respiratory motion in the reconstructed images while keeping the image noise at a minimum. This should improve cardiac imaging in PET/CT and also allow accurate tracking of the lung tumors accurately.

4.1 Respiratory signal acquisition: Hardware

The respiratory signal was acquired from the patient by laying a flexible belt around the abdomen of the patient. The belt had a black disc fastened to it, with a white spot in the center. The black disc provided strong contrast to the white spot and thus helped in focusing the camera on the white spot. A red light emitting diode (LED) was inserted at the center of the white spot and was used to synchronize the respiratory signal with the PET acquisition (see figure 4.2). The PET/CT scanner activated a signal at the start and end of the PET acquisition which was used to turn the LED on respectively off.

The white spot and the LED were tracked during the PET acquisition with the help of a video camera. The Panasonic NV-GS75 video camera with 3-CCD sensor chips and a resolution of 540000 pixels was used for this purpose. The camera allows upto 10x optical zoom, which was set to 5x for patient studies. It was connected to the acquisition computer via IEEE 1394 connector. The image frame rate was set to one frame every 0.2 seconds, which allowed real time processing while remaining much higher than the usual respiratory rate of one cycle per about 6 seconds in human beings. The camera was installed at the foot of the patient table at a suitable hight (see figure 4.4). As the camera is positioned on the patient table itself, motion of the latter does not change the relative position of the camera to the disc.

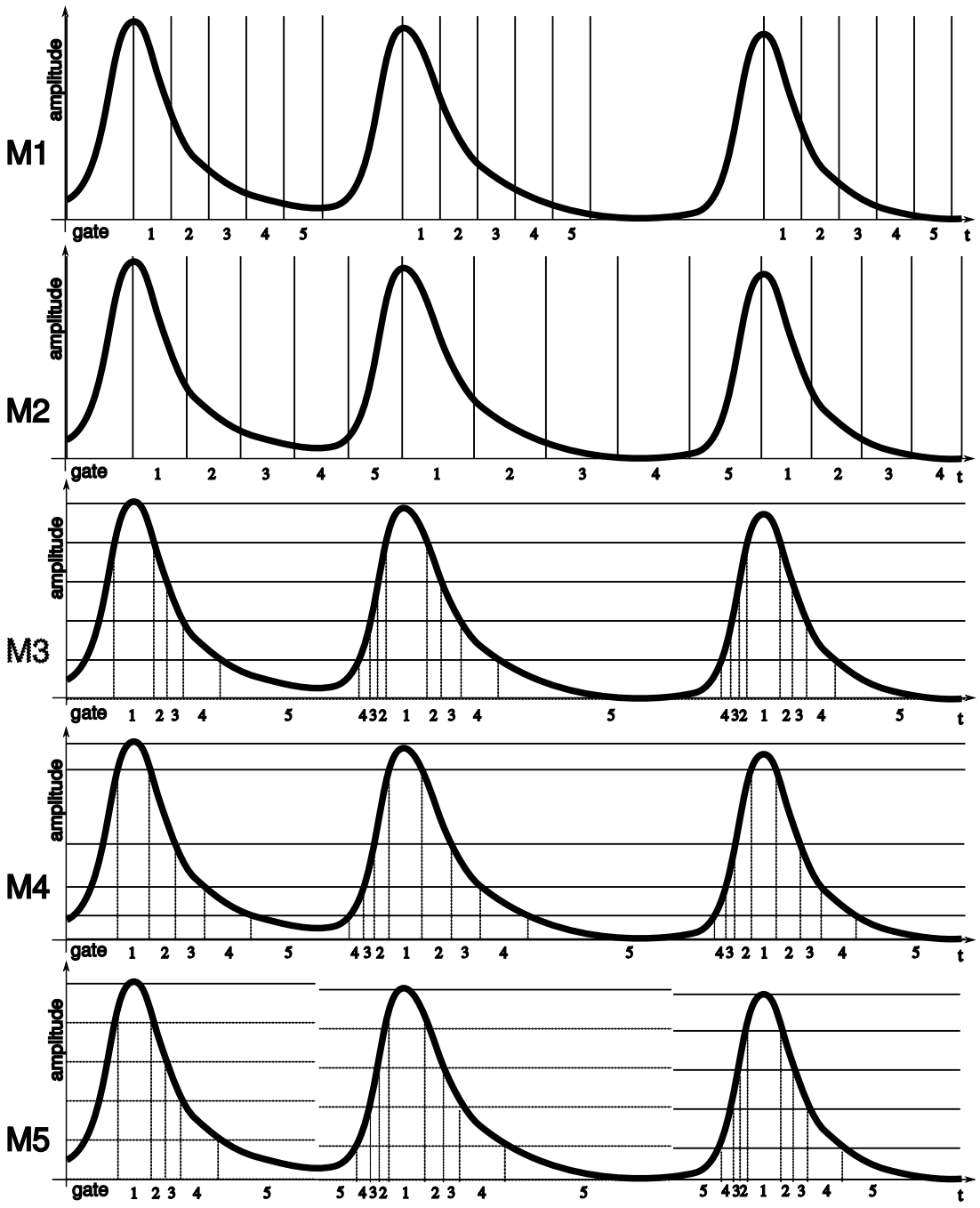

Figure 4.1: Principle of different time and amplitude-based gating schemes. From top to bottom: M1: time based equal gates, M2: time-based variable gates, M3: amplitude-based equal gates, M4: amplitude-based variable gates, M5: cycle-based equal amplitude gates. A five gate division is shown here for better visibility.

4.2 Respiratory signal acquisition: Software

Once the camera provided the images, they were processed with the help of dedicated software. This software was developed under Matlab while using Image acquisition and

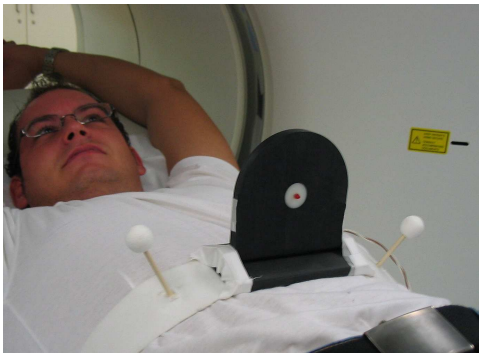

Figure 4.2: The disc used to estimate the position of the chest wall. The black disc is used as background with large contrast to the white spot. Center of mass of the white spot represents the chest wall position. The red LED in the center of the white spot is used to synchronize the respiratory signal with the PET data.

Figure 4.3: The camera used to acquire the respiratory signal of the patient.

Figure 4.4: The respiratory signal acquisition system. The camera is installed at the foot of the patient table.

image processing toolboxes. A region of interest (ROI) was selected on the camera image frames which was supposed to contain disc. All subsequent calculations were done on this

ROI, which was 80x80 pixel by default, with the option to change the parameters. For the first frame this was done manually by double clicking the white spot on the image shown on the user interface. As the disc moves with the abdominal motion of the patient, the white spot moves in the ROI. Therefore, the ROI is adjusted after acquisition of each frame. This ensures that the ROI remains focused on the white spot despite breathing motion and smaller movements of the patient, see figure 4.5.

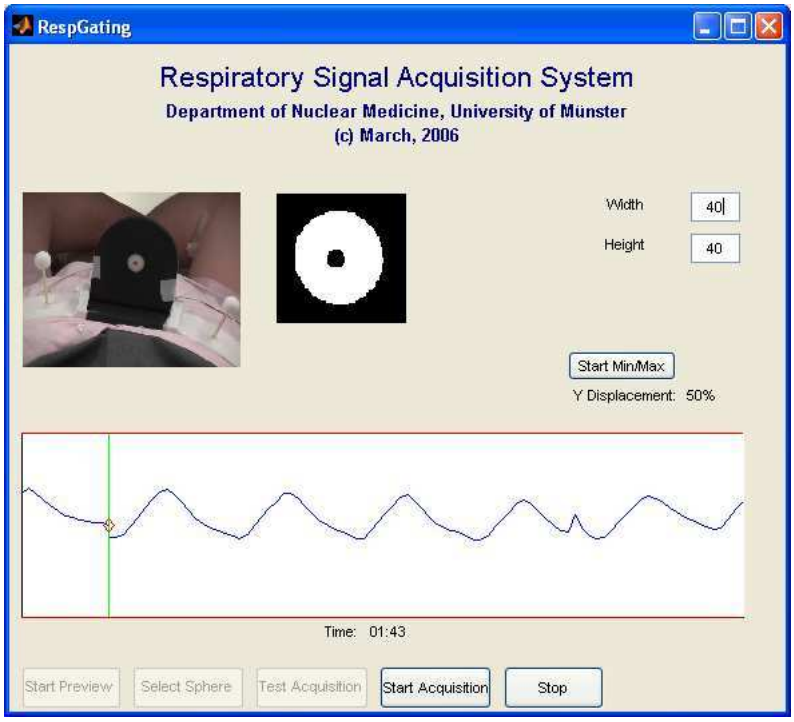

Figure 4.5: The user interface. The frame grabbed from the video camera is shown on the left. The segmentation results on the ROI are shown in a window in the middle. The position of the white spot, as given by its center of mass, is plotted below as respiratory signal. The current position is marked with the perpendicular line on the graph.

The global position of the white spot was used as reference for the respiratory signal. It was determined by calculating the center of mass of the white area, which can be easily found. For this, the white area was first segmented by automatically thresholding the ROI with the histogram based method of Otsu [82]. The center of mass of the white spot was calculated as the mean of the x and y positions of all pixels belonging to the segmented white disk. The size of the white spot (around 60x60 pixels) and the method of calculation make the center of mass relatively robust to noise and small distortions.

To reduce the influence of the LED light-rays on the segmentation and subsequent position estimation, only the blue channel of the video images was used. Similarly, to achieve maximum difference between LED-on and LED-off status, the red channel was used for monitoring the LED. Four values per video frame were stored in a file: 1. time elapsed since beginning of acquisition, 2. x-position and 3. y-position of the white spot and 4. the sum of red intensity values in the ROI. The real time nature of the software allows the user to monitor the patient's breathing pattern online, and give instructions

regarding respiration, e.g. when holding the breath is required etc.

After acquisition of the respiratory signal data, the listmode acquisition start and end times were found by searching for fast signal changes in the red intensity signal (LED on and off). These two positions were marked manually and the part of the data between the two on/off points was extracted. For that, the red intensity in the ROI was summed up and ploted against time. This allows the user to select a proper threshold for finding the LED-on and LED-off times by moving a red bar on the plot as shown in figure 4.6. The first time the signal trespasses the threshold is marked as the LED-on and the first time the signal falls below the threshold after LED-on is marked as LED-off position. Selecting the threshold should not be a problem due to the high light output of the LED and usage of the red channel of the camera for this purpose.

The y-positions of the center of mass were used for further analysis as they reflect the breathing motion of the patient [53]. Koch et al. found that the motion of lung vessels along the y-axis correlates highly with the motion of the abdominal wall. They tracked the motion of selected lung vessels and the skin of the patients with magnetic resonance imaging (correlation coefficient: 0.89). This system is very similar to some commercially available systems, such as the RPM respiratory tracking system from Varian (Varian Medical Systems, Charlottesville, VA, USA), which is also based on tracking a marker placed on the patients body.

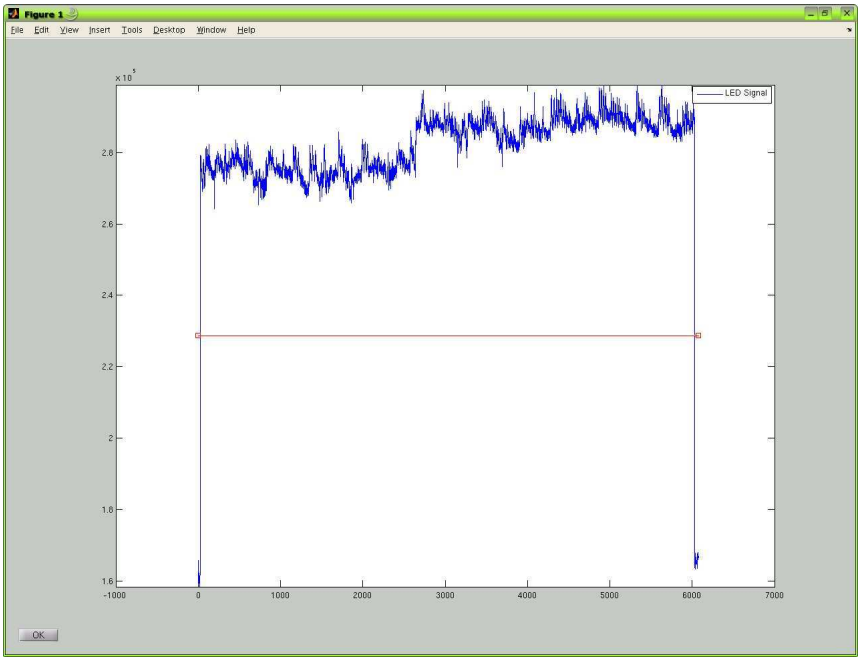

Figure 4.6: The user interface to select appropriate threshold for finding the LED-on and LED-off positions.

4.3 Respiratory gating methods

Seven different methods of sorting the PET data according to the respiratory status were studied. They can be divided into two main categories: 1. methods which are based

on time information and 2. methods based on amplitude information. Each of these two main types can further be sub-divided into two parts: 1. methods with fixed gate width (i.e., equal for all gates) and 2. methods with variable gate width (i.e., it varies with reference to some other function). In the following we will see that methods M1 and M2 are time based and M3 and M4 are amplitude based methods. Method M5 is a combination of both types and the last two methods M6 and M7 are variants of the amplitude based methods M3 and M4.

4.3.1 M1. Time based equal gates

In this method, the respiratory signal is first divided into individual breathing cycles with reference to a starting point, e.g., the beginning of the respiratory cycle. Starting with this point, a user specified number of gates is set in each cycle with all time gates having equal width, e.g. 300 ms. If a breathing cycle lasts longer than the total length of all gate widths, the remaining part of that cycle is discarded.

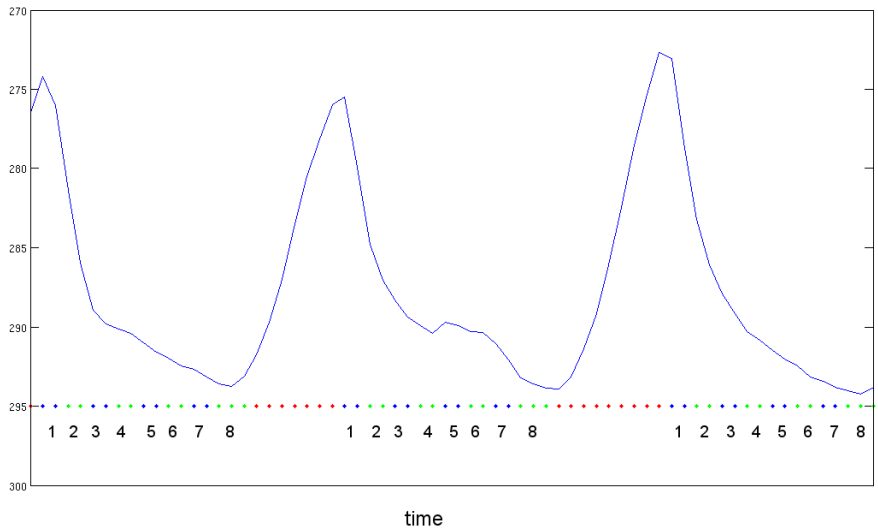

Figure 4.7: M1: The time based equal gates method. The information marked in red is lost as the length of the breathing cycles is greater than the sum of all gates. x-axis depicts time, y-axis the amplitude of the signal.

4.3.2 M2. Time based variable gates

This method is similar to method M1 with the difference that the signal from one reference point to the next (one breathing cycle) is individually divided into the same number of gates. Thus all PET data is used. However, depending on the length of each breathing cycle, the width of the respiratory gates in each cycle varies. We have used eight gates, which means that each breathing cycle was divided into eight equal parts. With changing width of breathing cycles, the width of the gates also changes, e.g. if the first cycle lasts 8 seconds and the second cycle 24 seconds, the gate width for the first cycle will be 1 second and that for the second cycle will be 3 seconds per gate.

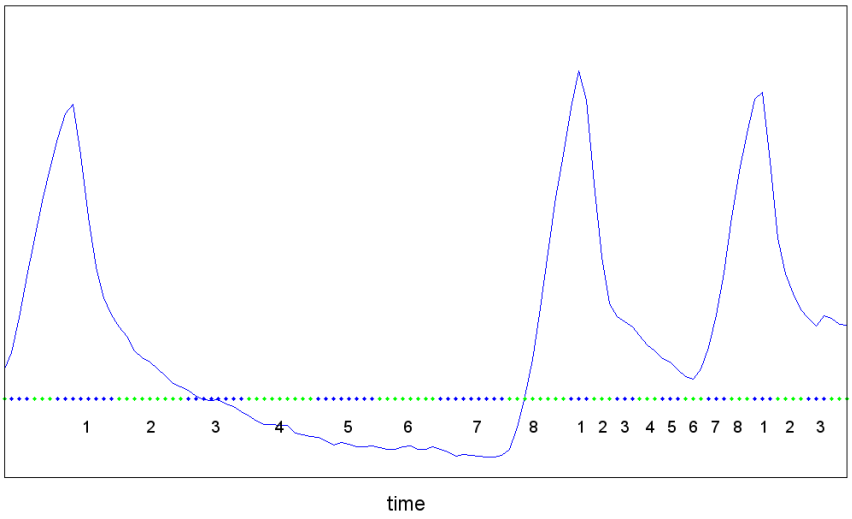

Figure 4.8: M2: The time based variable gates method. The width of the gates is adapted to the length of the breathing cycle. No information is lost. x-axis depicts time, y-axis the amplitude of the signal.

4.3.3 M3. Amplitude based equal gates

The respiratory signal is divided into a user-specified number of gates according to the amplitude. Each gate has the same height along the y-axis. As the whole respiratory signal is divided, no data is discarded. The amount of motion blur present in each gate is similar because the same amount of motion is present in all gates. Data from positions which do not correspond to each other spatially are sorted into different gates.

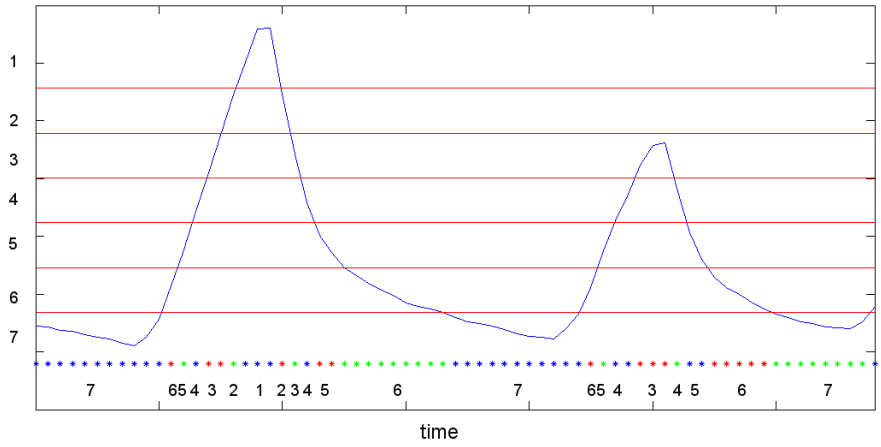

Figure 4.9: M3: The amplitude based equal gates method. The height of all gates is equal. No information is lost. Cycles with different breathing depths are sorted correctly. The x-axis shows time, y-axis the amplitude of the respiratory signal.

4.3.4 M4. Amplitude based variable gates

Again, the whole respiratory signal is used for gating; no data is discarded. However, the height of the gates varies with reference to statistics. Thus, we set the height of each gate depending on the total number of events in that gate. In the case of 8 gates, the height of each gate is selected so that 1/8th of the total events is contained in it. With equal number of events in each gate, the reconstructed images should have similar SNR because the amount of noise is dependent upon the number of events in the gate. This leads to another effect, namely the presence of variable amounts of blur in the gated images. To avoid this effect a sufficient number of gates has to be used. If respiratory signal shows an amplitude of 6 pixels, 8 gates may be used to remain on the safe side.

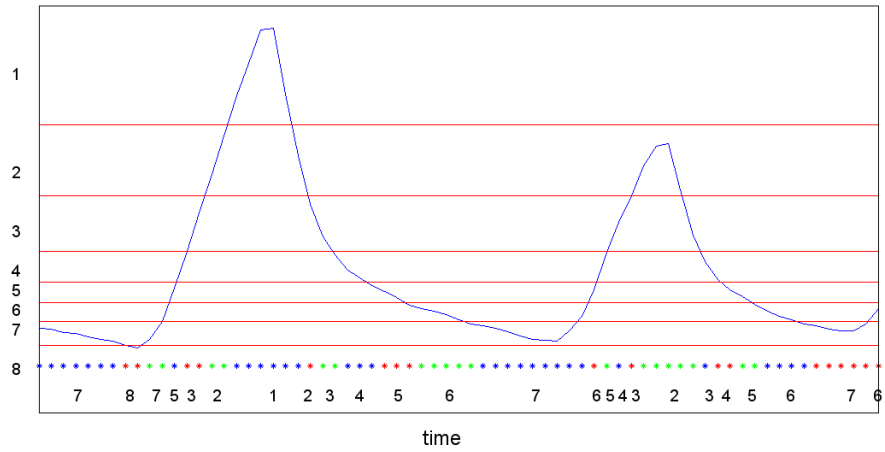

Figure 4.10: M4: The amplitude based variable gates method. The hight of each gate varies with the amount of events present in it. No information is lost. Cycles with different breathing depths are sorted correctly. The x-axis shows time, y-axis the amplitude of the respiratory signal.

4.3.5 M5. Cycle based equal amplitude gates

This method is similar to the method M2. The difference is that instead of dividing the whole respiratory signal into equally-heighted gates, each breathing cycle is individually divided into the gates. This leads to all the maxima of each cycle being sorted into one gate and so on.

4.3.6 M6+M7. Amplitude based methods with base line correction

These are variants of the methods M3 and M4. It was observed during the experiments that the respiratory signal tends to decline in amplitude baseline with time (see figure 4.11). This effect is possibly caused by muscle relaxation. Thus it may be appropriate to correct the respiratory signal for this shift in baseline of the amplitude before gating. In cycle-based methods this step is not necessary as each breathing cycle is separately gated. A simple method of base line correction was employed, which corrects the signal for shift by taking the center of mass for approximately 10 respiratory cycles and subtracting it from the signal.

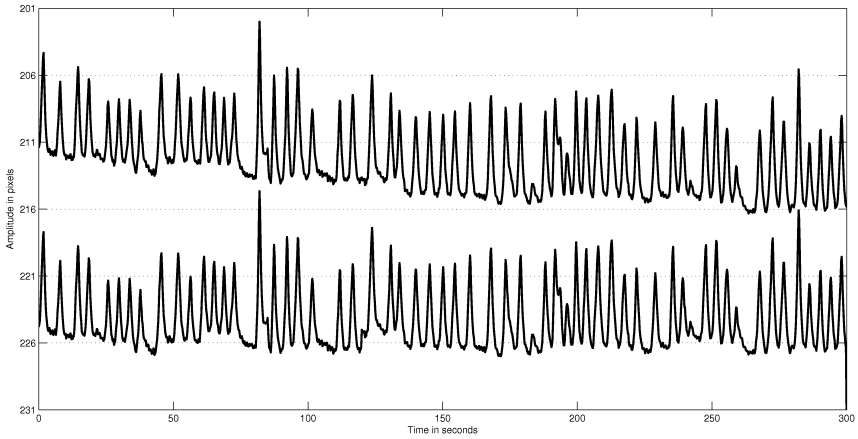

Figure 4.11: Example of a patient's respiratory signal. The base line drift in the upper graph is clearly visible. The lower graph shows the same respiratory signal after baseline correction. x-axis depicts time, y-axis the amplitude of the signal.

4.4 Patient data

Seven patients suffering from coronary artery disease were included in this study. A 20-min listmode PET acquisition was performed 1h post injection of ∼500 MBq ^{18}F-FDG. The raw listmode data were sorted into eight gates according to each one of the seven gating methods described above. The gated data was then reconstructed with an OSEM algorithm (4 subsets, 5 iterations) using the open source STIR package [1]. No attenuation correction was performed to avoid possible artifacts from CT-based attenuation correction. The size of the reconstructed 3D-images was 175x175x47 with the voxel size of 3.375 mm along all three axis. All images were normalized with respect to time. Thus images from one gate could be compared with images from another gate with longer or shorter total time duration.

4.5 Data analysis

Two parameters were considered to quantify the results of the different gating schemes: (1) motion and (2) image noise. Selection of motion is obvious as a metric, because that is the main motivation for the gating schemes, i.e. to obtain images with less motion. However, increasing the number of gates, each gate with lesser motion, by reducing the gate width leads to a problem: image noise due to lack of statistics. Thus the second metric selected was quantification of noise which throws light on the quality of the images. More noise means lesser quality and vice versa.

4.5.1 Motion

The first parameter is the amount of motion captured with any method of respiratory gating. The heart was selected to quantify the motion due to respiration, as it has a relatively large amount of ^{18}F-FDG uptake in the myocardium and thus the effects of noise, which is always present on PET images, are greatly reduced in line profiles through

the heart (see figures 5.1, and 4.13). The movement of the heart was measured along the y-axis on coronal slices as this is the axis along which maximum breathing motion occurs [53]. As the physical motion of the heart due to respiration is the maximum possible motion that can be detected on images it is implied in this study that the method with maximum measurable displacement of the heart should be the best method. In practice, always lesser amount of motion will be detectable and this deficiency will show the comparative strength or weakness of a particular method.

The heart undergoes two types of motion, respiratory motion and cardiac contraction. As the cardiac contraction is much faster than the respiratory motion (1 resp cycle≈6 sec, 1 cardiac cycle≈1 sec) and independent of the cardiac contraction, a 20 minutes scan means that the cardiac motion of the heart is averaged in each gate. Thus the effects of cardiac motion can be neglected in respiratory gated studies.

A coronal slice through the myocardium was selected individually for each patient and a line-of-interest was positioned on the lateral wall of the left heart ventricle. The activity profile was extracted along this line (from caudal to cranial) for each of the seven gating methods respectively (see figure 4.12). As the heart moves on the images, the position of the profile line shifts accordingly. The total motion of the heart can thus be determined by measuring the shift in position of the profile line. The shift in position was calculated at half of the maximum amplitude. The maximum displacement of the heart (MDH) was the difference between minimum and maximum positions on the ascending half of the plots, as that is where the heart is directly in contact with the diaphragm.

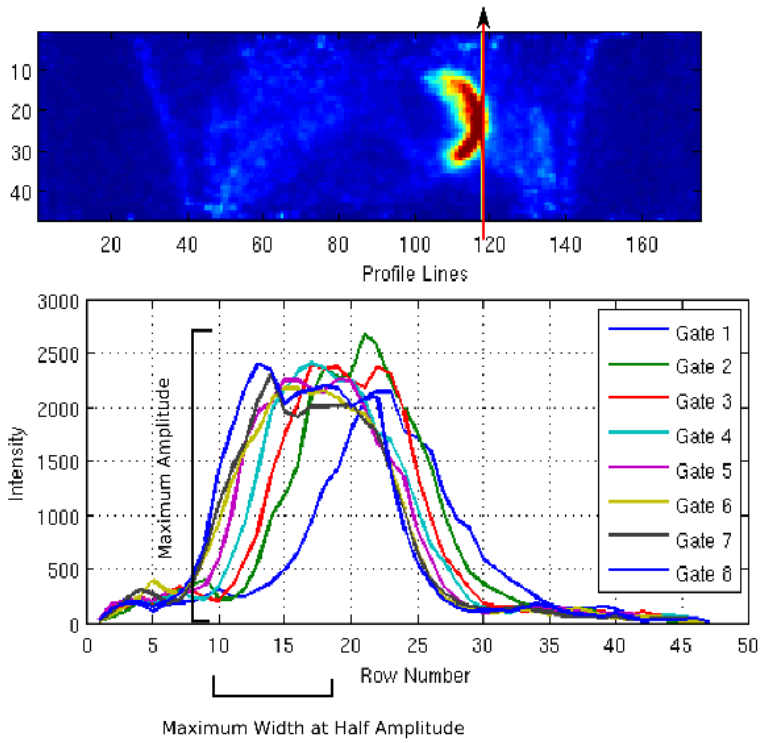

Figure 4.12: Intensity profile through heart of a patient. The position of the profiles is shown in figure above.

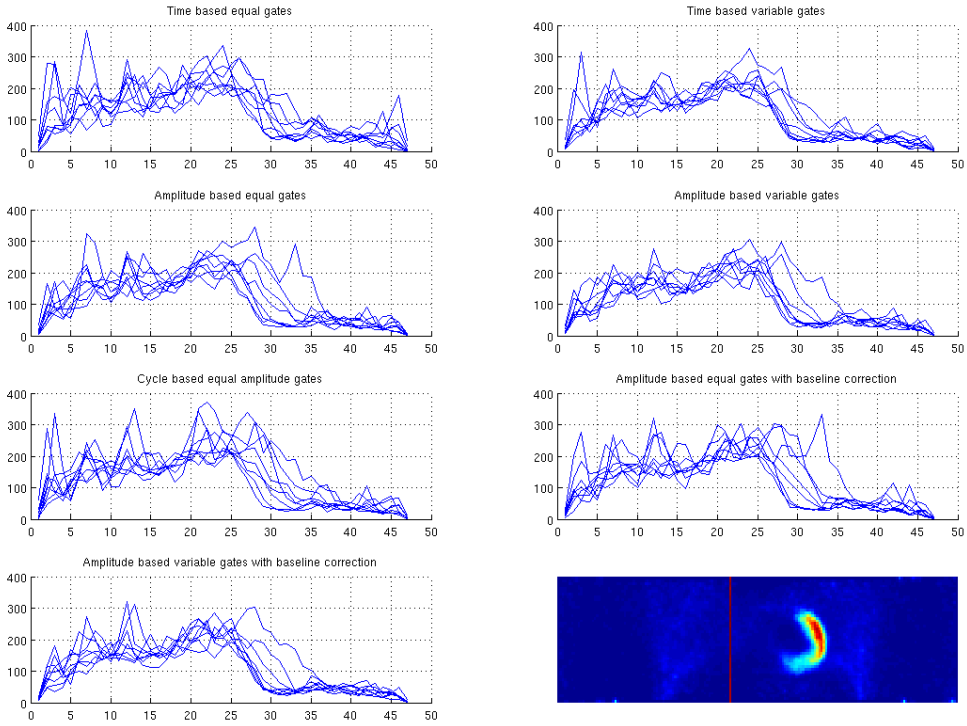

Figure 4.13: Intensity profile through lungs of a patient. The position of the profiles is shown in the image right below. The measurement of the motion is difficult and inaccurate on these noisy images.

4.5.2 Noise

The second parameter used is the amount of noise present on the images. Noise was defined as the standard deviation of the pixel intensities in a $20 \times 20 \times 10$ pixels ROI selected in the left-lung region. In the ideal case of noiseless images, the intensity of all pixels in this lung region should be same. However, this is not the case due to the presence of varying amount of noise. In gates with higher amount of noise, the variation among pixels intensities will be greater and vice versa.

Chapter 5

Results

The results of the experiments with different gating schemes with respect to the displacement of the heart and the noise properties of the images are given in the following sections.

5.1 Displacement of heart

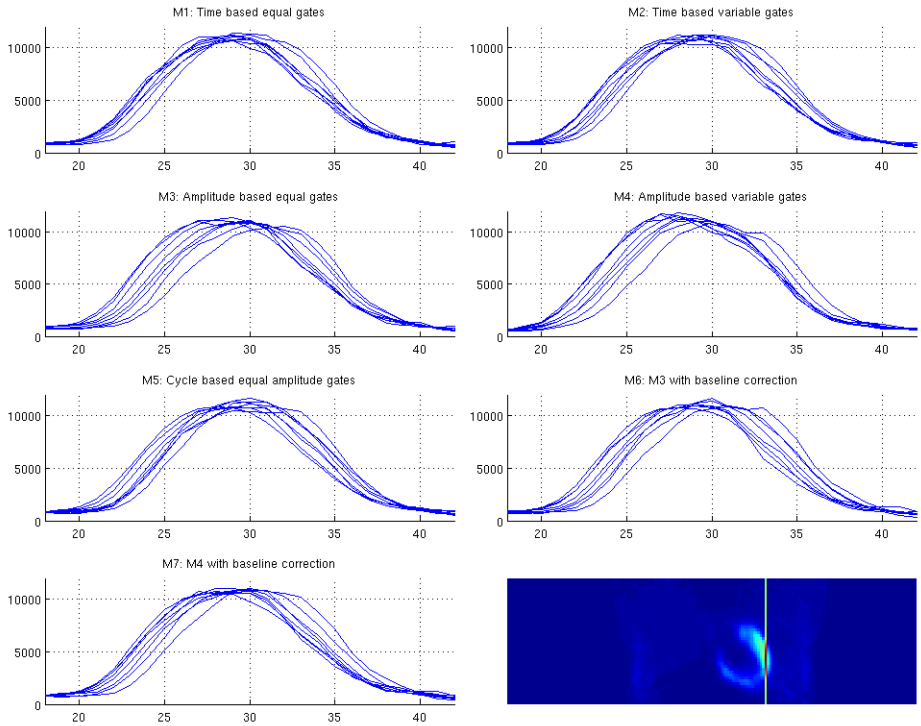

Figure 5.1: Intensity profile through heart of a patient. The position of the profiles is shown in figure right below. X-axis shows the slice transaxial numbers, and y-axis represent the non-attenuated uptake values.

An example of motion in a patient study is shown in figure 5.1, where the line pro-

files through the heart on a coronal slice are plotted for all seven gating schemes. The transaxial slice numbers are given along the x-axis of the plots, whereas the y-axis gives the uptake in arbitrary units. The maximum displacement between the eight gates at half of the maximum amplitude (MDH) is shown in Table 5.1. The rows show the MDH of a specific gating method for all seven patients whereas the columns contain the data for a single patient as given by different gating methods. The natural variation in breathing patterns of the patients is readily visible from the table. Some patients have smaller displacements, e.g. patient R has maximum MDH of 7 mm, whereas some others inhale much more deeply, such as Patient Ak with a heart displacement of up to 27 mm MDH.

The maximum displacement of the heart shows a global tendency for best results with the variable amplitudes method (M4) as this method gives the maximum MDH for all seven patients. The amplitude-based methods, with or without baseline correction, generally capture more motion than the time-based methods. Even the hybrid method of cycle-based equal amplitudes performs better than purely time-based methods in six out of seven cases. Among the amplitude-based methods, both equal amplitudes and variable amplitudes methods deliver similar results. Only in two of the seven cases does the variable amplitude method perform better, however, the difference is small. The hybrid cycle-based amplitude method performs much poorer. The baseline corrected methods do not give any better results as compared to the corresponding non-baseline-corrected methods. In all seven patients the baseline corrected methods show lesser or equal motion than their non-baseline-corrected partners. However, the results are better than those of the time based methods.

In the last row of Table 5.1, the variance of motion captured with the seven methods for all patients as ratio of the maximum to the minimum of the MDH with any of the seven methods is given. This shows how important the selection of the gating method is for getting accurate results. It is obvious from the data that the amount of motion captured by different techniques varies to a large degree. In six out of seven patients the MDH with the best method is over 150% of that of the worst method, e.g., the minimum MDH is 6 mm for Patient L whereas maximum is 10 mm. In two cases, patients R and Ak, the improvement is even greater than 200% (improvement of 4 mm resp. 14 mm) as compared with the worst case.

Table 5.1: Respiratory displacement of heart as captured with different gating methods

Patients	L	G	A	H	R	Ak	Hob
M1. Time equal	6	8	7	6	3	13	9
M2. Time variable	6	8	7	5	4	12	10
M3. Amplitude equal	10	11	11	6	6	27	17
M4. Amplitude variable	10	11	11	7	7	27	17
M5. Cycle equal amplitude	7	10	7	4	5	21	13
M6. Amplitude equal (BC)	8	10	9	6	5	25	14
M7. Amplitude variable (BC)	8	10	10	6	5	25	14
ratio of max to min	1.7	1.3	1.6	1.5	2.3	2.3	1.9

5.2 Noise properties

The analysis of the noise is given for one patient (Ak) in Table 5.2. The table shows that the noise in time equal images is much higher than in the time variable images. The noise level in the variable amplitudes method is almost the same in all eight gates, as expected, and is comparable to the times-variable method as both methods use all listmode events. Significant variation is visible in all methods except the amplitudes variable method (M4). The results for other patients show similar trends.

Table 5.2: Noise in reconstructed respiratory gates of patient Ak

Gates	G1	G2	G3	G4	G5	G6	G7	G8	Std
M1. Time eq	129.2	128.4	127.2	131.6	129.3	130.4	130.4	124.9	2.1
M2. Time var	104.2	108.4	109.8	112.3	112.5	110.4	109.1	105.2	3.0
M3. Amplitude eq	119.2	139.9	135.7	121.7	124.0	111.3	102.3	121.5	12.1
M4. Amplitude var	101.8	118.0	122.6	119.3	117.8	111.6	108.8	112.5	6.7
M5. Cycle amp eq	127.1	133.0	133.4	127.1	123.5	117.7	108.8	99.1	12.1
M6. Amplitude eq (BC)	119.6	141.6	132.8	123.5	118.6	106.9	101.5	120.5	12.8
M7. Amplitude var (BC)	120.4	107.7	114.2	115.9	112.8	108.8	109.9	119.1	4.7

Chapter 6

Discussion of Results

The experiments demonstrate that the amplitude-based methods are superior to both the time-based and the cycle-based methods. All seven patients examined in this study show larger amount of motion when amplitude-based methods are used. These results on real patient data confirm the work with phantom experiments by Wink et al [118] and extend it to various amplitude based gating methods.

6.1 Motion of heart

The primary motion of the heart is along the cranio-caudal direction. For example, the displacement for patient Hob was 1 mm in left-right, 2 mm in anterior-posterior and 9 mm in cranio-caudal directions for the method M1. This has also been demonstrated in a previous work using magnetic resonance imaging [53]. Although the motion of the heart may not be entirely along this line, the frequency and phase of the respiratory motion cycle should be the same for all organs along all axes. Moreover, the motion along the anterior-posterior and the left-right directions do not correlate with the abdomen motion strongly (see Koch et al. [53]). Since the respiratory monitor used in this study relies on the motion of the abdomen, the displacement along the cranio-caudal axis was calculated.

The variation in the amount of motion captured by different methods is surprising. As seen above, the difference between the best and worst method can be considerable. The source of this variation lies in the fact that the breathing cycle is neither symmetrical in shape nor consistent in amplitude over the whole period of acquisition. Both these parameters influence the gating scheme. A regular and sinus-function-like breathing signal will lead to almost similar results with any method of gating. If deep breathing phases are short, the time-based gating methods sort events from high amplitude phases with numerous small amplitude cycles into the same gate. Therefore they do not contribute much to the resulting images. Thus motion from these deep breathing phases is not detected on images reconstructed with these methods. The amplitude-based methods, on the other hand, bin all such deep respiration phases into separate gates and thus capture the motion more accurately.

Similarly, if the shape of the breathing cycle is not symmetrical with respect to the maximum amplitude axis, e.g., in a breathing pattern with extended end-expiration phase, most of the motion is sorted into the first couple of gates in time-based methods. The resulting reconstructed images will show the average position of the organs with blurring effects, similar to ungated images, in the first few gates and almost no motion in the

remaining ones. Thus, the difference between amplitude and time-based gating methods becomes large in patients who have an irregular and asymmetrical breathing pattern (see figure 6.1).

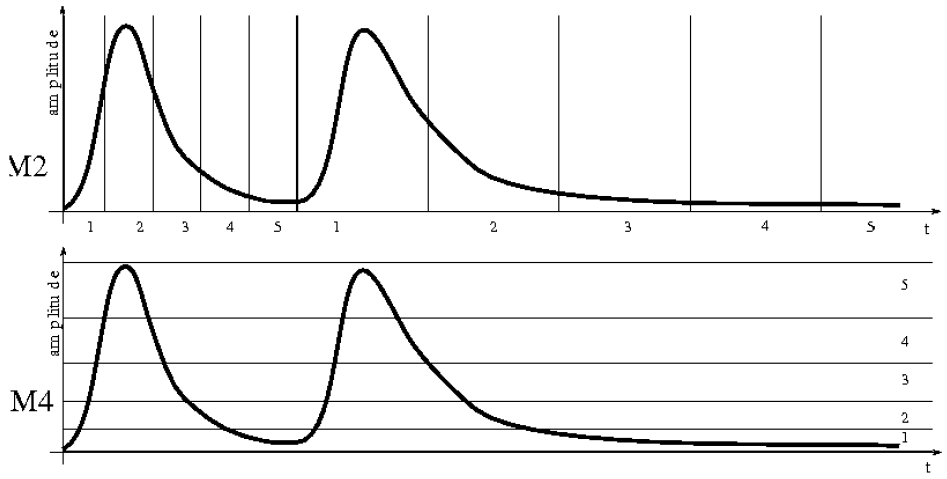

Figure 6.1: Asymmetrical respiratory signal. The time based method (M2) will sort all motion in the second cycle into first two gates. Only the amplitude based method can capture the motion correctly.

Both parameters do change considerably in most patients at irregular intervals. Figure 6.2 shows an example of a typical signal with short deep inhalation phases occurring at irregular intervals and figure 6.3 shows an example of extremely asymmetric breathing cycles where one breathing cycle is relatively short whereas the other cycle is very long due to an extended end-expiration phase.

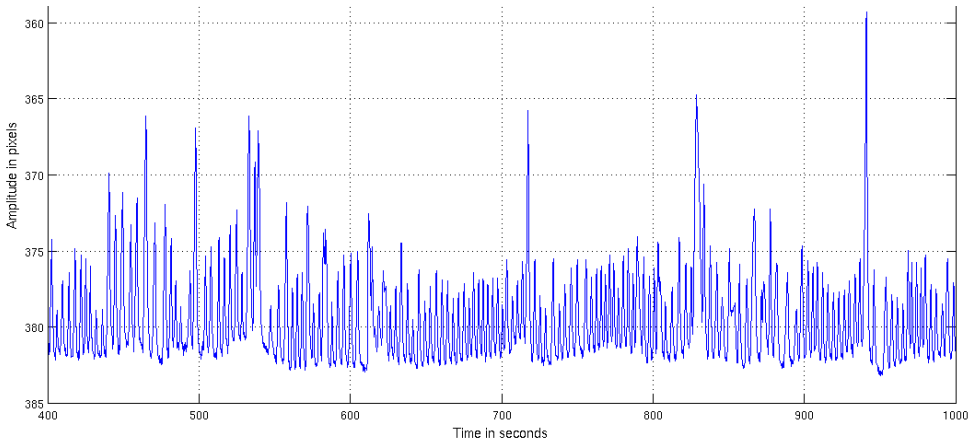

Figure 6.2: Respiratory signal of a patient. Note the deep inspiration cycles at irregular intervals and the variablity in their amplitudes.

In the time equal method (M1) (which is used by most commercial systems [78]) the sorting depends upon the window width. Thus not only important information is lost

with this method, but also information from different parts of cycles can be wrongly binned together if the length of cycles varies during the acquisition. The time based variational method (M2) may perform better due to its flexibility. But in breathing cycles with extended expiration cases even this method will sort almost all information from inspiration to expiration into one gate and divide the rest into the remaining seven gates resulting in large motion in one gate and almost no motion in the others.

6.2 Noise

The higher amount of noise present in M1 as compared to M2 (Table II) indicates that a part of events was discarded in M1 for reconstruction since the time length of each gate was pre-defined (fixed) and not individually chosen for each individual breathing cycle. Therefore, some data from the end of a breathing cycle may not be represented in the reconstructed data, leading to higher noise levels. However, this does not influence much the measurement of the heart displacement as given in Table I. This is due to the reason that the respiratory cycles were selected from maximum-to-maximum position. Thus, the maximum heart displacement is always present in the first gate. The end part of the expiration phase is relatively flat. Consequently the minimum heart displacement is always present in one of the late gates. This produces similar displacements for M1 and M2 while keeping the noise levels different.

Among the equal and variable time-based gating schemes, despite similar performance in capturing motion, there is significant difference in the quality of the reconstructed images with respect to noise. The time equal method discards information in breathing cycles that last longer than the sum of all gating windows width. Thus using lesser number of events leads to more noise in those images. M1 and M2 show the least variance in the amount of noise because these are time based methods and thus equal amount of events are sorted into every gate.

In all above mentioned cases the motion will be captured more accurately by amplitude-based methods (M3 to M7) as they are independent of the shape of the breathing signal with respect to time. Most patients seem to have irregular breathing patterns. That is the reason why amplitude-based methods perform generally better than time-based methods. However, as the lungs usually stay longer in the expiration state than in the inspiration state, the statistics in amplitudes based gates near the maximum expiration is much better than in other gates. This results in comparatively large amounts of noise in other gates when amplitude-based equal gates are used (M3).

It is advisable in certain applications to have similar amounts of noise in all gates. To overcome this disadvantage of the amplitude based gating, the method of variable amplitudes (M4) was devised. It ensures that gating is done with reference to the amplitude of the respiratory signal, however, equal number of events are sorted into each gate at the same time. Thus the results for this gating method show (Table 5.2) that the level of noise is almost constant among all gates.

The hybrid method of cycle-based equal amplitudes (M5) performs better than purely time-based methods, but worse than amplitude-based methods. This is caused by the fact that despite sorting the listmode data according to amplitudes within each cycle, the data from corresponding gates of all cycles are then added together and thus nullifies the advantage of amplitude-based sorting.

6.3 Baseline correction

Another important result is that the baseline correction of the respiratory signal (M6 & M7) does not lead to significantly better results. Table 5.1 shows that the baseline correction did not improve the performance of the gating schemes, it rather degraded the results by a small proportion. This may be due to the reason that the relaxation of the muscles is not confined to the anterior-posterior axis alone. As the muscles relax along the anterior-posterior direction (and lower the baseline of the disc motion), they may also relax along the cranio-caudal axis.

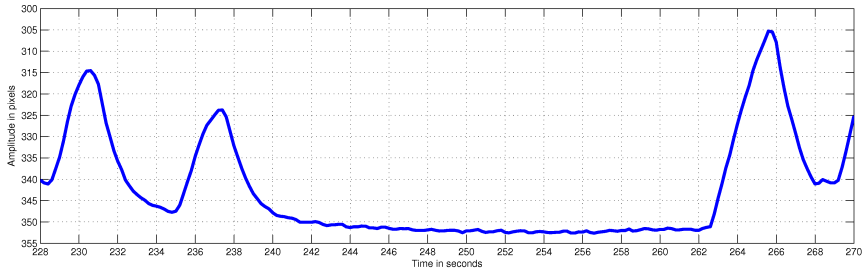

Figure 6.3: Variance in breathing cycles. The first cycle is much shorter than the second cycle with a prolonged end-expiration phase. Such cycles make the difference between variational or equal time-based gating schemes prominent.

Part III

Motion Correction

Chapter 7

Optical Flow Algorithms

In the second step of the proposed solution (see section 3.5), the individual frames or 'gates' are to be deformed to a user defined position in the breathing cycle. This position should be as near the attenuation map position as possible. The nature of the motion of the organs during PET acquisition makes it necessary to use methods of deforming or registering the individual gates to the target position with special properties. A brief introduction to registration methods might be helpful at this stage.

7.1 Registration Methods

Image registration algorithms are methods which try to find parameters, using which one image can be brought into spatial correspondence or alignment with another. Different terms are used for the image that is to be aligned and the one to which other images are aligned. In this study the image which is to be registered or aligned to another will be called the 'floating image' and the image with which the floating image is to be registered will be called the 'target' image. For example the floating images from seven respiratory gates can be registered with one target image to give eight images in spatial correspondence.

In cases where the imaging modality remains unchanged, such as in our case where all images are PET images from different gates, the problem of registration of two image volumes can be expressed mathematically as [13]:

$$I_2(x, y, z) = I_1(f(x, y, z)) \tag{7.1}$$

where f is a coordinate transformation function, i.e. $(x', y', z') = f(x, y, z)$.

The form of the function f determines the type of the registration method. Functions with simple translation and rotation (3 parameters for rotation and 3 parameters for translation) are called rigid registration methods.

Using α, β, γ as rotation and t_x, t_y, t_z as translation parameters, the rigid registration can be given as [117]:

$$T_r = A\vec{v}$$

where

$$A = \begin{pmatrix} \cos\beta\cos\gamma & \cos\alpha\sin\gamma + \sin\alpha\sin\beta\cos\gamma & \sin\alpha\sin\gamma - \cos\alpha\sin\beta\cos\gamma & t_x \\ -\cos\beta\sin\gamma & \cos\alpha\cos\gamma - \sin\alpha\sin\beta\sin\gamma & \sin\alpha\cos\gamma + \cos\alpha\sin\beta\sin\gamma & t_y \\ \sin\beta & -\sin\alpha\cos\beta & \cos\alpha\cos\beta & t_z \\ 0 & 0 & 0 & 1 \end{pmatrix}$$

and

$$\vec{v} = \begin{pmatrix} x \\ y \\ z \\ 1 \end{pmatrix}$$

Finding the unknown parameters is now the problem which can be solved by using different methods and similarity measures such as those described in [13],[65],[66],[89],[126]. An example of rigid registration is shown in figure 7.1.

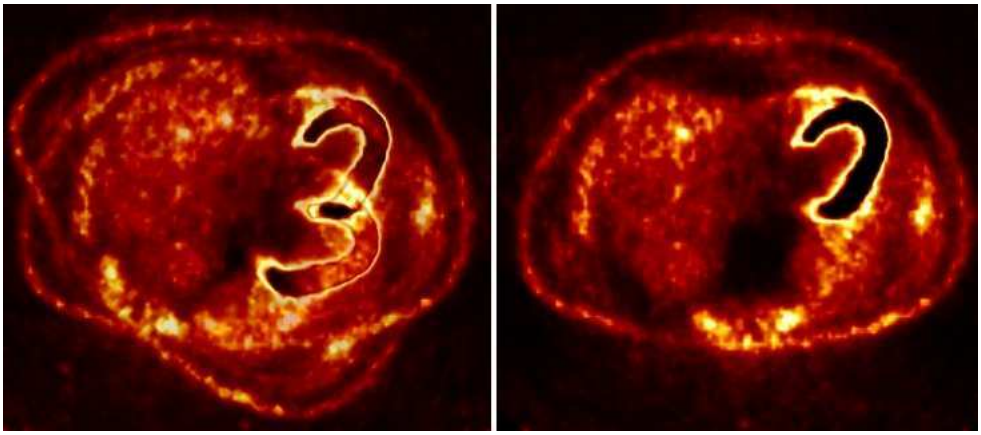

Figure 7.1: Rigid registration. The two images shown on the left are misregistered. After rigid registration with a rotation and a translation the images correspond spatially.

The rigid registration methods can align objects with translational and rotational motion. Thus lines will be registered with lines, and the angles between the lines will also be preserved i.e. a square will remain a square after such registration. Due to this property the rigid transformations fail if the objects in the images have a shear deformation and the angles between the lines are not preserved due to motion (see Fig. 7.2). To deal with such motion *affine* registration methods are required. These methods use additionally 3 parameters for scaling and 3 for the skew. They register parallel lines onto parallel lines and a square can be registered to a parallelogram.

7.2 Non-Rigid Registration

All of the above mentioned registration methods give a global transformation for the whole image. The same set of parameters is used to align all voxels on one image with the voxels in the other. As the body organs may undergo different types of motion, in different directions and with varying magnitudes at the same time, the methods needed in medical imaging should neither be organ specific nor rigid (see section 3). Rigid or even affine registration methods are thus not sufficient in our case. We require non-rigid methods which are able to register images with different objects performing different kinds of motion simultaneously. Also, it has been proved that in medical imaging rigid or affine registration methods are inferior to non-rigid registration methods in terms of accuracy [27].

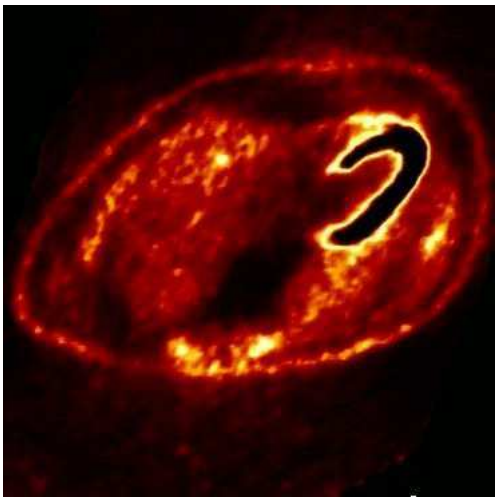

Figure 7.2: The image shown here has undergone an affine transformation. Rigid registration is not sufficient to correct such deformations.

The non-rigid registration methods register the images with the help of a vector field which is adapted to the deformations locally. The vector field has the same dimensions as the images to be registered, and each vector describes the motion of a single voxel in the floating image. Thus a line can be registered to a curve. Therefore, these methods are sometimes also called *elastic* registration methods.

The non-rigid registration algorithms can be classified according to the underlaying model that they use to estimate the deformations [23],[47]. Following this scheme of classification, there are three main categories of such algorithms: based on physical models, based on interpolation methods and based on transformation constraints. The algorithms of the first category use such physical models as stress-strain deformation or fluid flow equations. Optical flow algorithms, which will be used in this study, also belong to this category. Algorithms of the second category use basis functions such as splines, polynomial or wavelet functions whose coefficients are adjusted to give an approximation of the displacement field. The third category includes such methods which use transformation constraints. These include the transformation consistency i.e. the registration of A with B should correspond to registration of B with A or the transformation should be bijective etc. These methods may actually use one of the algorithms of the first two categories and add a constraint to it.

Simple elastic registration methods show disadvantages in case of localized deformations [126]. Interpolation and approximation based algorithms such as the splines based methods encounter problems at finer resolution scales [23] in addition to the fact that they do not model any physical or biological process. Thus optical flow methods were selected for motion correcting the PET data as they allow a higher degree of freedom in estimating the motion of different organs simultaneously and model the motion of a fluid.

7.3 Optical Flow

Optical flow is the change in the intensity pattern of the voxels between two image volumes. A vector field, called 'flow field', can be estimated by modeling the voxel intensity differences between the two image volumes as the flow of a fluid between two points. As this vector field describes the deformation between the two volumes, it can also be used to deform the floating volume so that it matches the target volume. The optical flow algorithms estimate this flow, or the the deformation between the image volumes, at the voxel level and thus belong to the category of the non-rigid methods of registration.

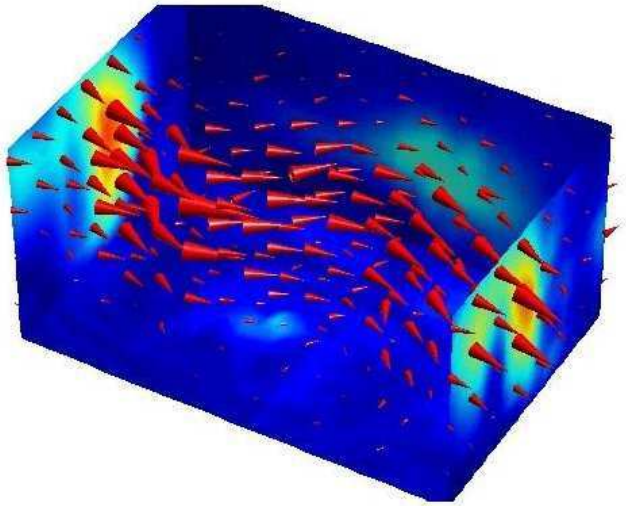

Figure 7.3: The optical flow. The deformations between two time frames can be visualized as the flow of a fluid.

7.3.1 Image Constraint Equation

Optical flow methods try to calculate the motion between two image frames which are acquired at times t and $t + \delta t$ at every pixel position. As a pixel at location (x, y, z, t) with intensity $I(x, y, z, t)$ will have moved by δx, δy, δz and δt between the two frames, following image constraint equation (also called brightness consistency constraint) can be given:

$$I(x, y, z, t) = I(x + \delta x, y + \delta y, z + \delta z, t + \delta t) \tag{7.2}$$

Assuming the movement to be small enough, we can develop the image constraint from equation (7.2) at $I(x, y, z, t)$ with Taylor series to get:

$$I(x + \delta x, y + \delta y, z + \delta z, t + \delta t) = I(x, y, z, t) + \frac{\partial I}{\partial x}\delta x + \frac{\partial I}{\partial y}\delta y + \frac{\partial I}{\partial z}\delta z + \frac{\partial I}{\partial t}\delta t + H.O.T$$

where H.O.T. means higher order terms, which should be small enough to be ignored. From these equations we achieve:

$$\frac{\partial I}{\partial x}\delta x + \frac{\partial I}{\partial y}\delta y + \frac{\partial I}{\partial z}\delta z + \frac{\partial I}{\partial t}\delta t = 0 \tag{7.3}$$

or

$$\frac{\partial I}{\partial x}\frac{\delta x}{\delta t} + \frac{\partial I}{\partial y}\frac{\delta y}{\delta t} + \frac{\partial I}{\partial z}\frac{\delta z}{\delta t} + \frac{\partial I}{\partial t}\frac{\delta t}{\delta t} = 0 \tag{7.4}$$

which results in

$$\frac{\partial I}{\partial x}u + \frac{\partial I}{\partial y}v + \frac{\partial I}{\partial z}w + \frac{\partial I}{\partial t} = 0 \tag{7.5}$$

where u, v, w are the x,y and z components of the velocity $\vec{V}$ or optical flow of $I(x, y, z, t)$ and $\frac{\partial I}{\partial x}$, $\frac{\partial I}{\partial y}$, $\frac{\partial I}{\partial z}$ and $\frac{\partial I}{\partial t}$ are the derivatives of the image at (x, y, z, t) in the corresponding directions. We shall write I_x,I_y,I_z and I_t for the derivatives in the following.

Thus

$$I_x u + I_y v + I_z w = -I_t$$

or

$$\nabla I \cdot \vec{V} = -I_t \tag{7.6}$$

This is an equation in three unknowns and cannot be solved as such. This is known as the aperture problem of the optical flow algorithms. To find the optical flow we need another set of equations which is given by some additional constraint. This is the main point where different optical flow algorithms differ from each other.

7.3.2 Optical Flow Methods

Many optical flow methods have been proposed to solve the image constraint equation. Three main categories can be used to classify these methods:

1. Block matching
2. Frequency domain correlation
3. Gradient based

In the block matching based optical flow algorithms, small blocks of one image are moved so that they matches with a block on the other image. The motion vector gives the transformation for this block only. All blocks in an image are moved until vectors are found that minimize some error function. It was shown by Davis/Freeman that block matching optical flow algorithms are equivalent to gradient based algorithms if the displacements are sub-voxel and the deformations are rigid body deformations [24]. Zhang/Lu have even combined both approaches to a hybrid block matching algorithm which utilizes gradient information [123]. Behar et al. combined block matching with gradient based optical flow in a small window [9]. Correlation based optical flow as presented by Duan et al. [32] is also a form of block matching.

One way of detecting motion on the images is to analyse their frequency transforms such as the fourier transform. The difficulty with such an approach is that the fourier transform is global and thus scenes including many objects undergoing motion render it not suitable for this task. Reed [95] uses a gabor filter based local frequency approach to overcome this problem and detect motion in the frequency domain of the images. A similar approach was already used by Fleet/Japson [37]. They use a decomposition of the images into band-pass channels and use a phase constraint equation in each channel to detect motion. Prince et al. use a combination of band-pass and gradient based optical flow [91]. Phase correlation based optical flow [110] also falls under this category.

There have been many proposals for the image gradient based methods of estimating optical flow. Lucas/Kanade proposed a solution which assumed the flow to be constant in a local neighborhood around the central voxel and used the least means of square approach [63]. Bab-Hadiashar improved the method by Lucas/Kanade by taking least median of squares approach at solving the over-determined linear equation system [5]. Instead of the least squares based methods, Horn/Schunck assumed a global smoothing function to solve the image constraint equation[48]. This method was improved by El-Feghali/Mitchie to preserve boundaries by weighting the smoothing term [33]. Deriche et al improved the Horn/Schunck algorithm by using a non-quadratic function for smoothing [28]. A different method was proposed by Alvarez *et al.* [2]. They improved the algorithm by Nagel/Enkelmann by using a brightness invariant term into consideration. Thus if two images differ in contrast by a constant factor, the method can still estimate the flow correctly. The local and global methods were combined by Vemuri et al. to register medical images [115]. Also Bruhn et al. [14] have given a framework for combined local and global optical flow.

Other approaches to optical flow estimation include the mass conservation method [93],[105], fluid mechanics based method [22], or approaches using higher order constraints on flow [38].

The gradient based algorithms for optical flow estimation achieve high accuracy and flexibility. It is thus no wonder that most of the research has been done in the area of gradient based methods. The gated volumes obtained from the PET data through gating contain equal amount of radioactivity. As all gates contain data from almost all breathing cycles, the basic image constraint equation is fulfilled in the PET data. Thus the gradient based methods can be applied to our problem readily.

7.3.3 Optical Flow applications

The optical flow methods present a strong instrument estimating the deformations between a set of images. Accordingly they have been used in many different areas. These include, stereo-vision, robot-vision, motion detection, image segmentation and medical imaging. Ignoring the application of optical flow to synthetic images, we describe in the following lines some instances of the use of the optical flow algorithms to different problems, especially to medical imaging.

The very first application of optical flow was to stereo imaging by Lucas/Kanade [63]. After that the main application field of optical flow has been the detection of motion e.g. Corpetti et al [22] used optical flow to detect the motion of water vapors on meteorological satellite images. Ancona/Poggio devised a detector on the basis of the optical flow to estimate the time-to-crash of a moving object [3]. If objects move on images, the optical flow can also be used to segment the objects from background e.g. by Galic et al. [40]. Another application was the tracking of sea ice on satellite images by Thomas et al. [110].

Medical imaging has also been a fertile field for the use of optical flow methods. Most of these applications are concerned with motion detection, registration and image segmentation on medical images. Modalities that have benefited from optical flow applications include, but are not confined to, Magnetic Resonance Imaging (MRI), Computed Tomography (CT), Positron Imaging Tomography (PET) and Ultrasound (US) imaging.

Hata et al. used optical flow to measure the deformations between magnetic resonance images of the brain taken before, during and after brain surgery [45]. Zientara et al. used optical flow to measure dilation and contraction of liver tissue during laser ablation on

MRI images [125]. Another application was to estimating cardiac displacements in tagged MRI images [30],[91]. Optical flow has been used to segment heart on gated MRI images by Galic et al. [40]. Recently successful tracking of endocardium on MRI images was shown by Duan et al. [31].

On the CT side, Song et al. [105] and Gorce et al. [43] used optical flow to estimate 3D velocity fields on CT cardiac images. A recent study by Torigian et al. suggests use of optical flow for assessing regional air trapping in lung CT images acquired in inspiration and expiration phases [111]. A method for prospective motion correction of X-ray imaging of the heart was presented by Shechter et al. [103].

Klein [50] was probably one of the first to apply optical flow to cardiac PET studies for motion correction. Vemuri et al. used optical flow to register medical images [115]. Dawood et al. have used Optical flow to correct PET images for the effects of motion [25][26].

Besides MRI, CT and PET optical flow has been also used in other medical imaging areas e.g. Behar et al. have used optical flow in echocardiography [9]. In the following sections five algorithms based on the gradient method are presented. To give an immediate and visual impression of the algorithms a hypothetical experiment with a cube and a sphere is conducted, whereby the sphere has to be transformed to the cube using optical flow based transformations (see figure 7.4). Along with the visual result, a middle slice out of the sphere is presented with the motion vectors. The motion in x,y and z directions is coded by red, green and blue colors respectively. The vectors will give additional clues to the comparative performance of the algorithms. Quantitative results will be presented in the results chapter.

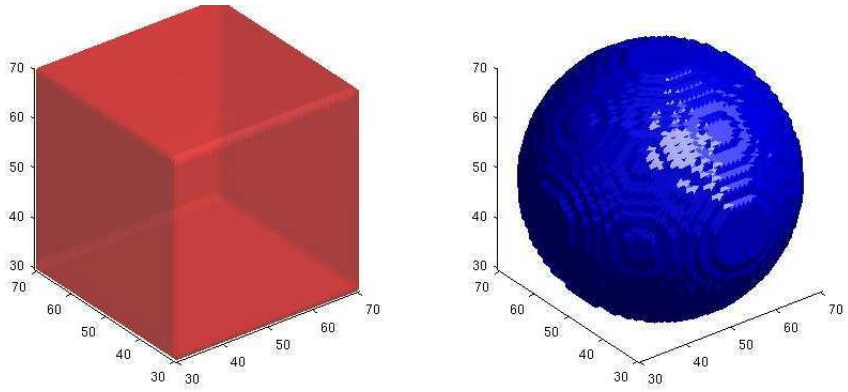

Figure 7.4: The sphere is to be deformed to the cube. The results with different algorithms are shown below.

7.4 Local optical flow algorithm

Lucas and Kanade use a non-iterative method which assumes a locally constant flow [63]. Evaluations and comparisons by Barron [6], Bruhn [15] and Galvin [41] have shown that the Lucas-Kanade algorithm is one of the best methods for calculating optical flow fields under different aspects, especially in presence of noise. As the PET data is inherently very noisy, we have chosen the Lucas-Kanade algorithm as the basis for our application. We use the 3D extension of this algorithm with a weighting function and a matched set

of smoothing and derivative filters, which will be described in more detail below.

Assuming that the flow (u, v, w) is constant in a small window of size $m \times m \times m$ with $m > 1$, which is centered at voxel x, y, z and numbering the pixels as $1...n$ we get a set of equations:

$$\begin{aligned} I_{x_1}u + I_{y_1}v + I_{z_1}w &= -I_{t_1} \\ I_{x_2}u + I_{y_2}v + I_{z_2}w &= -I_{t_2} \\ \vdots \qquad & \vdots \qquad \vdots \\ I_{x_n}u + I_{y_n}v + I_{z_n}w &= -I_{t_n} \end{aligned}$$

With this we get more then three equations for the three unknowns and thus an over-determined system. We get:

$$\begin{pmatrix} I_{x_1} & I_{y_1} & I_{z_1} \\ I_{x_2} & I_{y_2} & I_{z_2} \\ \vdots & \vdots & \vdots \\ I_{x_n} & I_{y_n} & I_{z_n} \end{pmatrix} \begin{pmatrix} u \\ v \\ w \end{pmatrix} = \begin{pmatrix} -I_{t_1} \\ -I_{t_2} \\ \vdots \\ -I_{t_n} \end{pmatrix}$$

or

$$A\vec{V} = -b$$

To solve the over-determined system of equations we use the least squares method:

$$A^T A\vec{V} = A^T(-b)$$

or

$$\vec{V} = (A^T A)^{-1} A^T(-b) \tag{7.7}$$

or

$$\begin{pmatrix} u \\ v \\ w \end{pmatrix} = \begin{pmatrix} I_x^2 & I_x I_y & I_x I_z \\ I_x I_y & I_y^2 & I_y I_z \\ I_x I_z & I_y I_z & I_z^2 \end{pmatrix}^{-1} \left(-A^T I_t\right) \tag{7.8}$$

This means that the optical flow can be found by calculating the derivatives of the image in all four dimensions. A weighting function $W(i, j, k)$, with $i, j, k \in [1, .., m]$ should be added to give more prominence to the center pixel of the window. Gaussian functions are preferred for this purpose. We have used a quasi Gaussian weighting scheme by using the square of the euclidean distance from the center pixel as a measure of weighting. Other functions or weighting schemes are possible.

One of the characteristics of the Lucas-Kanade algorithm, and that of other local optical flow algorithms, is that it does not yield a very high density of flow vectors, i.e. the flow information fades out quickly across motion boundaries. Figure 7.5 shows that the motion correction has been not accurate on the synthetic data due to the large magnitude of deformation present on the images. The edges have not been deformed properly and errors exist on the surface. The results lack smoothness due to the local nature of the method. The main advantage of this method is its comparative robustness in presence of noise [6], [14].

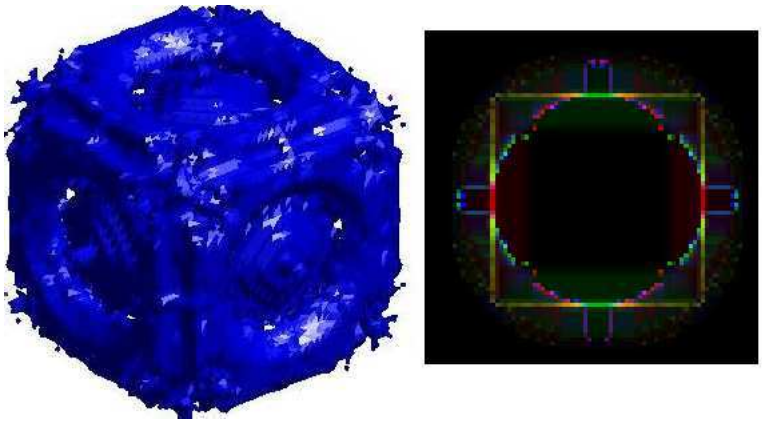

Figure 7.5: Result with Lucas/Kanade algorithm. The estimated vectors for the middle slice of the sphere are also shown. X-component in red, Y-component in green and Z-component in blue shades. The vectors show the lack of smoothness due to the local nature of the method.

7.5 Global optical flow algorithm

A global optical flow algorithm introduces the additionally required constraint by postulating a global condition. Horn was one of the first to develop an optical flow algorithm. Horn and Schunck algorithm used an image matching constraint assuming a global smoothness constraint on the flow field. This method was soon applied to medical imaging by Song et al. [105] to calculate the flow field in CT images of the heart. The function to be minimized is given by combining the image constraint (see equation 7.2) with a smoothing functional.

$$f = \int ((\nabla I \cdot \vec{V} + I_t)^2 + \alpha(|\nabla u|^2 + |\nabla v|^2 + |\nabla w|^2))\mathrm{d}x\mathrm{d}y\mathrm{d}z \tag{7.9}$$

The parameter α is a regularization constant. Larger values of α lead to a smoother flow. This problem can be solved by calculating the Euler-Lagrange equations corresponding to equation (7.9). These are as follows:

$$\begin{aligned} \Delta u - \frac{1}{\alpha} I_x(I_x u + I_y v + I_z w + I_t) = 0 \\ \Delta v - \frac{1}{\alpha} I_y(I_x u + I_y v + I_z w + I_t) = 0 \\ \Delta w - \frac{1}{\alpha} I_z(I_x u + I_y v + I_z w + I_t) = 0 \end{aligned} \tag{7.10}$$

where Δ denotes the Laplace operator so that
$\Delta = \nabla^2 = \frac{\partial^2}{\partial x^2} + \frac{\partial^2}{\partial y^2} + \frac{\partial^2}{\partial z^2}$.

Solving these equations with Gauss-Seidel for the flow components u, v, w gives an iterative scheme:

$$u^{k+1} = \frac{\Delta u^k - \frac{1}{\alpha} I_x(I_y v^k + I_z w^k + I_t)}{\frac{1}{\alpha} I_x^2}$$

$$v^{k+1} = \frac{\Delta v^k - \frac{1}{\alpha} I_y (I_x u^k + I_z w^k + I_t)}{\frac{1}{\alpha} I_y^2}$$
$$w^{k+1} = \frac{\Delta w^k - \frac{1}{\alpha} I_z (I_x u^k + I_y v^k + I_t)}{\frac{1}{\alpha} I_z^2} \tag{7.11}$$

where the superscript $k+1$ denotes the next iteration, which is to be calculated and k is the last calculated result. Δu can be obtained as:

$$\Delta u = \sum_{q \in N(p)} (u(q)) - u(p)) \tag{7.12}$$

where $N(p)$ are the six neighbors of the position p in 3D space. Analogue equations apply to the other flow components v, w.

An alternative algorithmic implementation is given by Barron [6] as:

$$u^{k+1} = \overline{u^k} - \frac{I_x (I_x \overline{u^k} + I_y \overline{v^k} + I_z \overline{w^k} + I_t)}{\alpha^2 + I_x^2 + I_y^2 + I_z^2}$$
$$v^{k+1} = \overline{v^k} - \frac{I_y (I_x \overline{u^k} + I_y \overline{v^k} + I_z \overline{w^k} + I_t)}{\alpha^2 + I_x^2 + I_y^2 + I_z^2} \tag{7.13}$$
$$w^{k+1} = \overline{w^k} - \frac{I_z (I_x \overline{u^k} + I_y \overline{v^k} + I_z \overline{w^k} + I_t)}{\alpha^2 + I_x^2 + I_y^2 + I_z^2}$$

where $\overline{u^k}$ refers to the average of u^k in the neighborhood of the current pixel position, and analogue for v, w.

Advantages of the Horn-Schunck algorithm include that it yields a high density of flow vectors, i.e. the flow information missing in inner parts of homogeneous objects is *filled in* from the motion boundaries. On the other hand, it is more sensitive to noise than local methods [14],[70]. The smoothness of results, in contrast to the results of the local method, is readily visible in figure 7.6 although errors still exist at the edges and especially at the corners. The vectors show, that the motion was detected at the edges and fades quickly across the more homogeneous regions.

7.6 Combined local-global optical flow algorithm

Keeping the characteristics of local and global algorithms in view, it is natural to combine both types of algorithms to get the best of both worlds. For this, Bruhn [14] has presented a mathematical framework which allows combinations of both Lucas-Kanade as well as Horn-Schunck algorithms into a single equation. Defining:

$$V = \begin{pmatrix} u \\ v \\ w \\ 1 \end{pmatrix} \quad , \quad \nabla I = \begin{pmatrix} I_x \\ I_y \\ I_z \\ I_t \end{pmatrix} \text{ and}$$
$$|\nabla V|^2 = |\nabla u|^2 + |\nabla v|^2 + |\nabla w|^2$$

we can rewrite the Lucas-Kanade algorithm as minimization of a function f_{LK}:

$$\begin{aligned} f_{LK} &= V^T (k * (\nabla I \nabla I^T)) V \\ &= k * (I_x u + I_y v + I_z w + I_t)^2 \end{aligned} \tag{7.14}$$

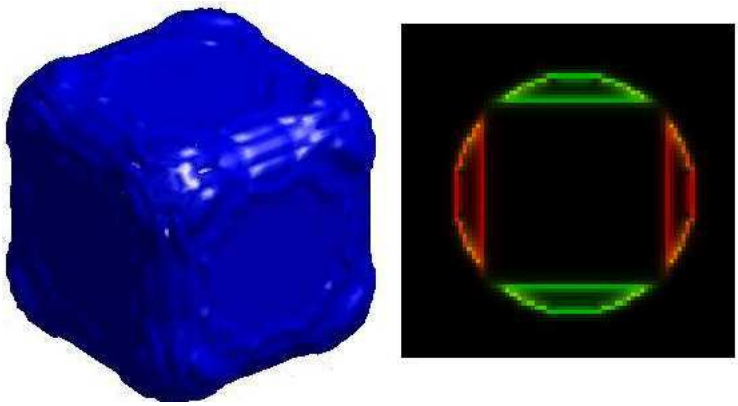

Figure 7.6: Result with Horn/Schunck algorithm. The estimated vectors from the middle slice are given with X-component in red, Y-component in green and Z-component in blue shades. The estimated flow is smooth but the parts away from the boundaries loose motion information quickly.

where k is a weighting function which is convolved with the image data. Minimization of equation (7.14) means $\partial_u f_{LK} = 0,\ \partial_v f_{LK} = 0,\ \partial_w f_{LK} = 0$.

Similarly the Horn-Schunck algorithm can be rewritten as minimization of a function f_{HS}:

$$f_{HS} = \int (V^T \nabla I \nabla I^T V + \alpha |\nabla V|^2) \mathrm{d}x\mathrm{d}y\mathrm{d}z \tag{7.15}$$

Combining both functions gives us the local-global function:

$$f_{LG} = \int (k * V^T (\nabla I \nabla I^T) V + \alpha |\nabla V|^2) \mathrm{d}x\mathrm{d}y\mathrm{d}z \tag{7.16}$$

The first term in this function is dependent upon the image gradient and can be called the data term whereas the second term is the smoothing term. The solution of the Euler-Lagrange equations is then analogous to equations (7.11). The results may be seen in figure 7.7, which shows that the visual results have become poor than with the previous algorithms. The motion information is missing in areas away from the boundaries and the edges show errors. The magnitude of vectors at the edges varies from voxel to voxel, meaning some of them are deformed more heavily than others, this shows the inconsistencies in the heavy penalization of the outliers.

7.7 Non-Quadratic approach to minimization of f_{LG}

In the Lucas-Kanade, Horn-Schunck and the Local-Global methods the minimization of the corresponding energy functions f_{LK}, f_{HS} and f_{LG} is based upon quadratic optimization methods, thus outliers are penalized heavily. To avoid this, Deriche [28] proposed to use a non-quadratic method. Using a function ψ_i, suggested originally by Charbonnier [20], we get the function:

$$f_{NL} = \int \{\psi_1(D) + \alpha \psi_2(S)\} \mathrm{d}x\mathrm{d}y\mathrm{d}z \tag{7.17}$$

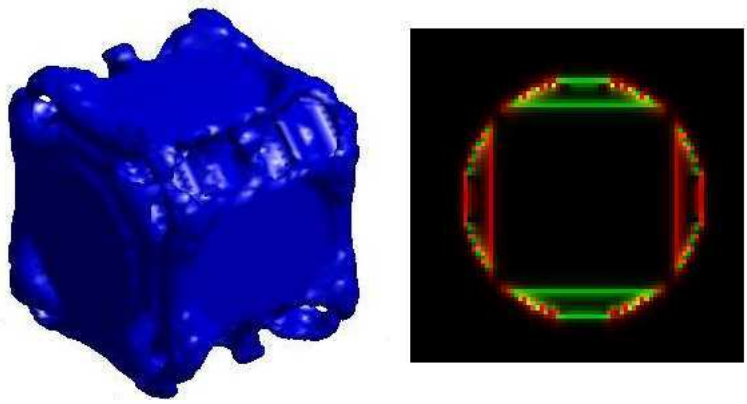

Figure 7.7: Result with Bruhn-Simple algorithm. Apparently the results have become poor than HS at the outer edges, the motion information is missing in areas away from the boundaries.

where $D = k * V^T(\nabla I \nabla I^T)V$ and $S = |\nabla V|^2$. The functions ψ_i are given by:

$$\psi_i(s^2) = 2\beta_i^2\sqrt{1 + \frac{s^2}{\beta_i^2}}, i \in 1, 2 \tag{7.18}$$

With this improvement the function f_{LG} becomes convex in s and thus has a unique solution; β_i is a scaling factor [14].

The corresponding Euler-Lagrange equations for our non-quadratic combined local-global function are:

$$\begin{aligned}
\mathrm{div}(\psi_2'(S)\nabla u) - \frac{1}{\alpha}\psi_1'(D)I_x(I_x u + I_y v + I_z w + I_t) = 0 \\
\mathrm{div}(\psi_2'(S)\nabla v) - \frac{1}{\alpha}\psi_1'(D)I_y(I_x u + I_y v + I_z w + I_t) = 0 \\
\mathrm{div}(\psi_2'(S)\nabla w) - \frac{1}{\alpha}\psi_1'(D)I_z(I_x u + I_y v + I_z w + I_t) = 0
\end{aligned}$$

The algorithmic iterative solution is then given by:

$$u_i^{k+1} = \frac{\sum_{j\in N}\frac{\psi_{2i}'+\psi_{2j}'}{2}u_{x_j}^k - \psi_{1i}'\frac{h^2}{\alpha}f_{x_i}\left(f_{y_i}v_i^k + f_{z_i}w_i^k + f_{t_i}\right)}{\sum_{j\in N}\frac{\psi_{2i}'+\psi_{2j}'}{2} + \psi_{1i}'\frac{h^2}{\alpha}f_{x_i}^2}$$

$$v_i^{k+1} = \frac{\sum_{j\in N}\frac{\psi_{2i}'+\psi_{2j}'}{2}v_{y_j}^k - \psi_{1i}'\frac{h^2}{\alpha}f_{y_i}\left(f_{x_i}u_i^k + f_{z_i}w_i^k + f_{t_i}\right)}{\sum_{j\in N}\frac{\psi_{2i}'+\psi_{2j}'}{2} + \psi_{1i}'\frac{h^2}{\alpha}f_{y_i}^2}$$

$$w_i^{k+1} = \frac{\sum_{j\in N}\frac{\psi_{2i}'+\psi_{2j}'}{2}w_{z_j}^k - \psi_{1i}'\frac{h^2}{\alpha}f_{z_i}\left(f_{x_i}u_i^k + f_{y_i}v_i^k + f_{t_i}\right)}{\sum_{j\in N}\frac{\psi_{2i}'+\psi_{2j}'}{2} + \psi_{1i}'\frac{h^2}{\alpha}f_{z_i}^2}$$

with

$$\psi'_{1i}(D) = \frac{1}{\sqrt{1 + \frac{(I_{x_i}u_i + I_{y_i}v_i + I_{z_i}w_i + I_{t_i})^2}{\beta_i^2}}} \tag{7.19}$$

and

$$\psi'_{2i}(S) = \frac{1}{\sqrt{1 + \frac{|\nabla u_i|^2 + |\nabla v_i|^2 + |\nabla w_i|^2}{\beta_i^2}}} \tag{7.20}$$

where i is the current pixel position.

The updated elements of the flow should be immediately used for the next step, as required by the Gauss-Seidel method. Thus only one variable array is needed for the calculation which is constantly updated. The results of this algorithm are shown in figure 7.8. It is readily visible that the motion information is more smoothly spread out in homogeneous regions. Thus the vectors do not fade out quickly at the boundaries as in all previous examples. There are still small visible defects at the edges and the motion is spread out inside the cube as well because discontinuities are not preserved so strictly.

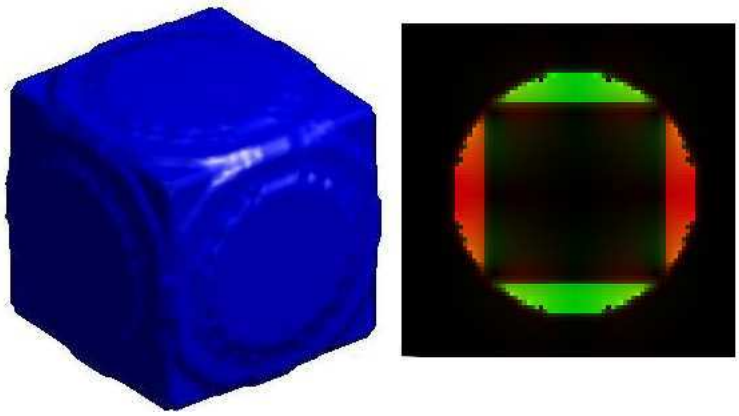

Figure 7.8: Result with Bruhn-Nonlinear algorithm. The motion in parts away from boundaries is filled in correctly. There are small defects at the edges and the motion information is spread out inside the cube as well.

7.8 Preserving discontinuities

The smoothing term in the above algorithm ensures high density in the optical flow but it has the negative impact of smoothing out the flow across the boundaries of moving objects. In the case of medical images, which are being used here, smoothing across organ boundaries is not meaningful. Physiologically the organs in human body do perform different types of motion but they never mingle with each other in the sense that the tissue of one organ flows inside the other. Thus keeping the flexibility of optical flow, it is necessary to accentuate the organ boundaries which amounts to preserving discontinuities in the flow.

A whole range of methods has been proposed for preserving these discontinuities. The techniques include using variable values for α or selecting only a part of equations in case

of local methods [7] or to use a function that tries to preserve discontinuities by weighting the smoothing term [14], [28], [33]. With this approach the equation for the optical flow, f_{LG}, can be transformed into:

$$f_{DP} = \int \{\psi_1(D) + \alpha\psi_2(\kappa, S)\} \mathrm{d}x\mathrm{d}y\mathrm{d}z \tag{7.21}$$

The appropriate weighting function κ should have the property of reducing the effect of the smoothing term in areas of discontinuity, i.e. at object boundaries, but to retain the effect in areas of homogeneous flow such as inside the objects. We have thus adopted a function in accordance with the needs of our problem of PET/CT motion correction by weighting the the smoothing term in accordance with the image gradient. Thus places where edges are present will be smoothed less than areas inside organs which usually have lesser number of edges and with a lower gradient. This function is given by:

$$\psi_2(\kappa, S) = \psi_2(|\nabla I| * |\nabla V|^2) \tag{7.22}$$

The convolution in this case is to be understood as applied to the corresponding components. This in turn leads to the reformulation of equation (7.20) as:

$$\psi'_{2i}(S) = \frac{1}{\sqrt{1 + \frac{|I_x|*|\nabla u_i|^2 + |I_y|*|\nabla v_i|^2 + |I_z|*|\nabla w_i|^2)}{\beta_i^2}}} \tag{7.23}$$

The discontinuity preserving algorithm uses coupled pairs of equations. The optical flow is calculated iteratively in a double loop. The outer loop updates the ψ variables and the inner loop updates the u, v, w optical flow components. The algorithm in pseudo code can be described as follows:

```
initialize u, v, w, psi_1, psi_2
for outer loop
  for i,j,k {pixel positions}
    update psi_1'   as in equation 5.18
    update psi_2'   as in equation 5.22
  end
  for inner loop
    for i,j,k {pixel positions}
      update u
      update v
      update w
    end
  end
end
```

The results of this modification on our example are shown in figure 7.9. The spread of motion information to the parts away from the boundaries due to the smoothing functional is as strong as in the previous example. However, the discontinuity preservation leads to quick suppression of smoothness inside the cube. The errors at the boundaries have also become fewer than before.

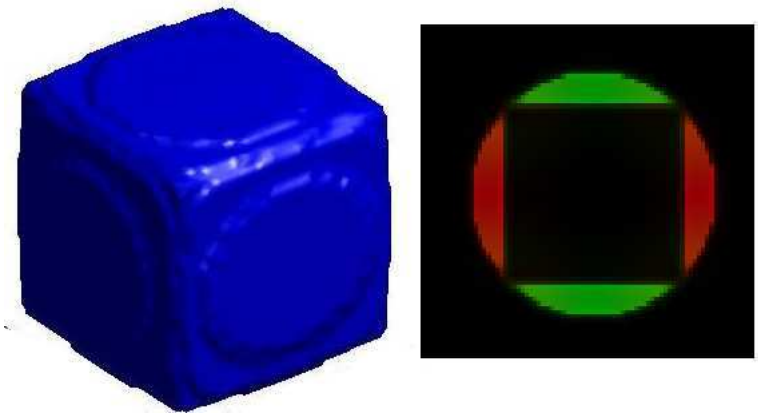

Figure 7.9: Result with Discontinuity Preserving algorithm. The information is filled in the parts away from the boundaries. However the discontinuity preservation leads to suppression of smoothness inside the cube.

7.8.1 Complexity

The algorithm consists of a double loop structure as visible from the pseudo code given above. The flow variables are updated only in the inner loop whereas the variables ψ_i are updated only in the outer loop. Thus the total complexity can be given as the sum of individual complexities for calculating the variables. Using n as the number of voxels in the image volume:

$O(n)$ for the calculation of ψ_i and

$O(n^2)$ for the calculation of the flow variables u, v, w.

Thus the total complexity can be given by:

$O(n^2)$

The algorithm was implemented in Matlab (The Mathworks, Natick, USA). A part of the algorithm, the update function, was written in C and then embedded in a framework with Matlab interface. This allowed the algorithms to be executed at a much higher speed than pure Matlab code, although not as fast as a pure C implementation. The size of the volumes was 175x175x47 voxels as mentioned earlier. The time on a standard PC for optical flow calculation between two such image volumes was around 20 seconds.

7.9 Correcting for motion

Once the motion is estimated, it can be removed by inverting the motion vectors at every pixel position and deform the 3D image according to the motion vector field. As the motion vectors obtained from the optical flow algorithms are not always integers e.g. $(u, v, w) = (0.2, 0.03, 1.05)$, interpolation has to be employed [64],[57],[109],[58],[86]. A tri-linear interpolation method was used in this study. All motion-corrected gates can then be summed up to get the PET data with minimal motion. Thus each PET gate is transformed to the target position (Fig. 7.10).

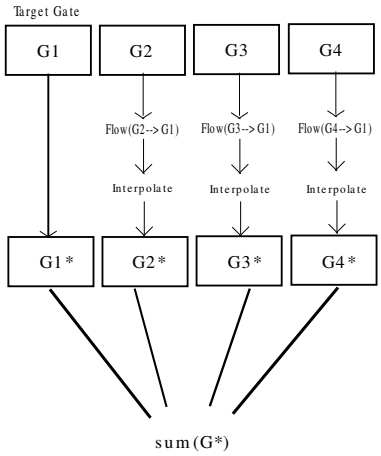

Figure 7.10: The process flow (eight gates were actually used, only four are shown here for simplicity).

7.10 Parameter optimization

The parameters for all algorithms were determined automatically as follows: The optimal parameters were found with the help of the genetic algorithms. For this the Genetic Algorithm and the Direct Search toolboxes of the Matlab software package were used. All parameters were optimized individually for each dataset for each algorithm separately. The correlation coefficient served as the fitness function. The population size was set to 10 and the number of evolution steps to 50 generations. The first generation was chosen randomly. Experiments showed that the optimal parameters for the algorithms were already found after around 15 generations and there was no significant change in the parameters thereafter. However, the number of generations was kept at 50 to ensure optimal results. The parameters optimized for each of the algorithms are given in table 7.1. The optimized values for the algorithms are summarized and discussed in the discussions section.

7.11 Test data

Two types of data have been used to evaluate the methods: software phantom data and real patient data. The software phantom data is only used to demonstrate the principle. The evaluation of the performance is done on real patient data.

7.11.1 Software phantom data

The NCAT software phantom is a computational model of the human torso for tomographic simulations. It is widely used in nuclear medicine for simulating emission tomography images [101]. The phantom models the major thoracic structures and organs such as lungs, heart, liver etc. based on NURBS (non-uniform rational B-splines). Uniform radioactivity numbers can be assigned to each organ so that all voxels belonging to a certain organ will have the same radioactivity level. The images represent the results

Table 7.1: Parameters optimized for each algorithm

Algorithm	Parameters
Lucas-Kanade	w: window size
Horn-Schunck	α: smoothness, n: number of loops
Bruhn-Simple	α: smoothness, n: number of loops
Bruhn-Nonlinear	α: smoothness, β_1, β_2: scaling parameters, ω: convergence parameter n_i: number of inner loops, n_o: number of outer loops
Dis. Preserving	α: smoothness, β_1, β_2: scaling parameters, ω: convergence parameter n_i: number of inner loops, n_o: number of outer loops

of an ideal emission tomography scan (perfect spatial resolution, no noise). Attenuation inside the phantom should also be considered to make the simulation more realistic. However, it should not be corrected during the reconstruction since the use of attenuation correction before motion correction leads to artifacts on the reconstructed images [81]. The image data was corrected for attenuation inside the phantom by forward-projecting the attenuation maps produced by the NCAT phantom software into the sinogram-data-space and attenuating the PET emission data with it using the open-source STIR (http://stir.hammersmithimanet.com/) software package.

The phantom data was used to obtain eight respiratory gates for the simulated patient study. The duration of the respiratory cycle was set to 5 seconds, the extent of diaphragm motion to 2 cm. The anterior-posterior expansion of the lungs was 1.2 cm. The images from the center of the torso, containing the heart, were forward projected to get sinograms. Poisson noise was then added to the sinograms to make the data more realistic. Poisson noise is dependent upon the statistics in the data, if the statistics on the phantom data are comparable to that of the patient data, the noise level should also be similar. The number of counts in the phantom data was 24 million per gate which is roughly similar to our normal human FDG PET studies with about 25 million counts per gate for a 20 minutes study.

Further data processing, as described below, is needed to provide a PET simulation. The resulting noisy sinograms were reconstructed with the help of an OSEM reconstruction algorithm [113] using 4 subsets and 5 iterations. The reconstructed images had a voxel size of 3.375 x 3.375 x 3.375 mm^3. The STIR software was used for forward projections and reconstructions. The limited resolution of the clinical scanner was taken into account during the reconstruction with the STIR program. Scanner specifications as used in patient data reconstructions were also used for reconstruction of the phantom data. The activity in different organs was set as follows. Myocardium: 75kBq/ml, blood pool: 2kBq/ml, liver: 75kBq/ml, lungs: 4kBq/ml, ribs: 2kBq/ml, background activity inside the body: 2kBq/ml. The limited resolution of the clinical scanner was taken into account

during the reconstruction process.

Figure 7.11: Coronal view of the NCAT software phantom simulating PET data.

7.11.2 Patient data

Sixteen patients with known coronary artery disease were included in this study. Patients were routinely referred to the ^{18}FDG PET scan for evaluation of myocardial viability prior to revascularization. A listmode dataset was acquired for 20 minutes, 1 hour post injection of [^{18}F]-FDG (4 MBq/kg). One ^{13}N-Ammonia study for evaluation of myocardial perfusion is also included in the database. The age of the patients (15 men, 1 women) varied from 37 years to 75 years and their weight from 56 kg to 99 kg. To enhance FDG uptake in the heart, patients underwent a hyperinsulinemic euglycemic clamp technique prior to and during the scan [116][52]. All patients received β-blockers to slow down and stabilize the heart rate during CT examination.

The Siemens Biograph Sensation 16 PET/CT scanner (Siemens Medical Solution) with a dedicated listmode research package was used in these studies. The respiratory signal for gating was acquired during the PET listmode acquisition. The listmode file contains the coincidences along with the time of occurrence. This information together with the respiratory information was used to sort the data into respiratory phases. The PET scanner has a spatial resolution of around 6 mm [34]. The data was not attenuation corrected as explained before.

To evaluate the influence of noise on the optical flow results, all sixteen patient datasets were reconstructed with 100%, 75%, 50% and 25% of the total listmode datafile. The lower amount of events in these reconstructions leads to higher amount of noise on the reconstructed images (see Fig 7.12). Noise supressing filters were set to 'off' during the reconstruction to retain the noise statistics.

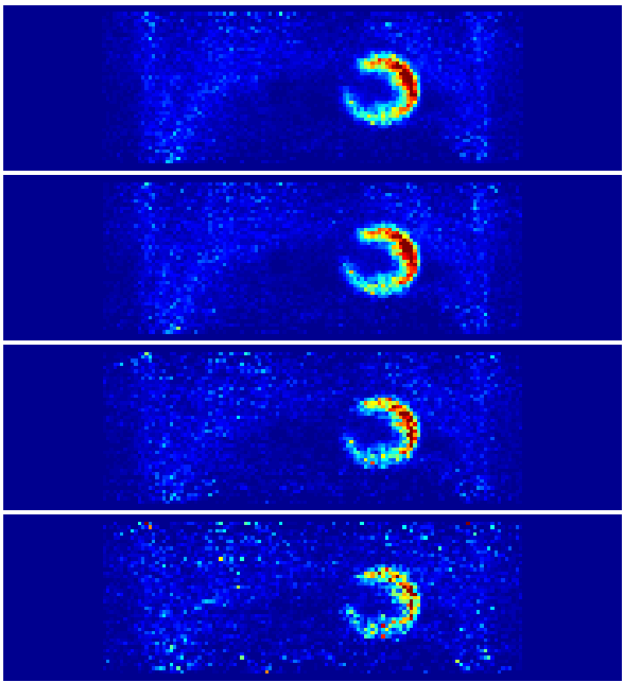

Figure 7.12: Example of PET images (coronal slices, patient P2), artificially degraded by reconstructing 100%, 75%, 50% and 25% of listmode files from top to bottom

7.12 Criteria for measuring improvement

The evaluation of the performance of the different optical flow methods is important to quantify the results. Many such evaluation methods have been proposed before [99]. Three different and independent criteria were selected in this study to objectively assess the quality of the motion correction. These are the displacement of the heart, the correlation coefficient, and the noise.

7.12.1 Displacement of the heart

The heart moves up and down due to respiratory motion of the lungs and diaphragm. Thus heart motion is an indicator of respiratory motion. In typical FDG PET images, the heart is mainly visible in the form of the left ventricle, as the myocardium shows maximum uptake of the radioactive tracer in that tissue region. The reduction of heart motion, therefore, serves as an indicator for the performance of the motion correction technique.

Eleven patient datasets were selected for this analysis. The remaining five patients could not be evaluated since the myocardium did not show FDG uptake. A simple thresholding method [82] was used to segment the heart. After segmentation, the center of mass of all pixels belonging to the left ventricle of the myocardium was calculated as the average value of all x,y and z coordinates. Taking the average from a large number of pixels makes this method relatively robust to noise and small threshold variances. The movement of the heart can now be assessed by observing the motion of the center of mass through all gates.

The results given by this method of assessment take the 3D aspect of the data into

account. They can thus be considered objective and relatively precise. Displacements of heart are absolute as the reduction in motion can be measured directly and in absolute units i.e. in millimeters. This method is local in nature as it only considers the left heart ventricle.

7.12.2 Correlation coefficient

The second measure used for assessment of the performance is the correlation coefficient. The correlation coefficient (CC) is defined as:

$$cc = \frac{\sum_i (x_i - X)(y_i - Y)}{\sqrt{\sum_i (x_i - X)^2 \sum_i (y_i - Y)^2}} \tag{7.24}$$

where x_i, y_i are the intensity values from two datasets at position i, and X, Y are their mean values. The correlation coefficient was calculated on the whole 3D image volumes.

The correlation coefficient considers all pixels in the 3D volume. It is more prone to noise than the heart motion method. As the mean of the dataset does not change by addition of gaussian noise with mean 0, the CC is sensitive to the noise variance. Thus, the CC is global in nature. The correlation between the uncorrected images is relatively high (CC in the range of 0.8) since most pixels in the volume do not move, e.g. those pixels outside the body. Although the results given by this method do not relate to improvements in absolute numbers (e.g. millimeters), the analysis of the CC is a measure of the relative performance of the different algorithms.

Mutual information, which is widely used in registration methods, was not found to be adequate to discern the differences properly. Mutual information has a sharp maximum in the proximity of ideal registration only. With increasing distance, it approaches the asymptotic limit more rapidly than CC and thus is not able to distinguish between the images. Secondly, mutual information is more sensitive to noise than correlation coefficients[65].

7.12.3 Noise

The amount of noise present on the images can also be used to assess their quality. To measure the amount of noise on the PET images, a region of interest ($16 \times 16 \times 10$) was selected inside the lungs. The standard deviation of all voxel values in this region was used as an indicator of the noise level. A fully noise free image should have same brightness values in the homogeneous region selected as the ROI. The standard deviation would be equal to 0. As soon as noise comes into play, the standard deviation of the voxels increases. Thus this measure indicates the extent to which noise is present on the images.

7.12.4 Significance test

Using small sets of data can lead to many a wrong conclusion. It is therefore necessary to apply statistical significance tests to the results before quantitative conclusions can be drawn. In statistics, a result is called statistically significant if it is unlikely to have occurred by chance. Many such tests have been devised, they include the Chi-square test, the students-t test, the binomial test, the F-test, etc. (see [44]).

Among these tests the Students-t Test has found widespread application in the medical field. A particular form of this test, the paired student's t-test [19], was applied to assess the significance of the results. This test gives the probability of the Null-Hypothesis for a population before and after the application of some method e.g. a medicine was given to a number of patients and their blood sugar level was observed before and after the use of the drug. The students-t test can then tell us, how significant the difference in blood sugar levels was.

The Null-hypothesis assumes that there is *no* significant difference between the results before and after the application. This means that low values of probability for the Null-Hypothesis translate into high probability values for significant differences in the results. In the present study, the same test is applied to the PET image data before and after the application of the motion correction algorithms. The results will show if the correction was significant. The confidence level of the test was set to 95%. Probability values (p-values) *less* than 0.05 indicate that the data differ from each other significantly.

Chapter 8

Results

In this chapter the results of the Lucas-Kanade (LK), the Horn-Schunck (HS), the hybrid local-global algorithm by Bruhn (B-S), the non-linear version of Bruhn simple (B-NL) and the discontinuity preserving (DP) optical flow algorithms are evaluated with respect to their ability to reduce the motion on the images. First the proof of principle is given with phantom data in section 1. Sections 2 and 3 give the results of heart displacement analysis and the correlation coefficient analysis on the original patient datasets. The results on the reduction of noise given in section 4. Lastly, section 5 gives the results on the impact of different noise levels on the performance of the algorithms.

8.1 Phantom data: Proof of principle

Figure 8.1 shows the visual results of the DP motion correction algorithm on software phantom data. The top image shows the target gate (G4). The blur caused by the respiratory motion, which is present on the uncorrected images at the lung base and the heart (Fig. 8.1, middle), has been corrected to a great extent (Fig. 8.1, bottom). As the respiratory cycle was divided into eight gates in the NCAT phantom simulation, the lungs are at end-inspiration phase at the start of the respiratory cycle, they contract to end-expiration and return to end-inspiration phase at the end of the cycle.

The intensity profiles through the lung base (Fig. 8.1 top, white line) at the position with maximum respiratory motion are displayed in figure 8.2. The large displacement of the lung base is visible before motion correction (Fig. 8.2, left). The individual respiratory phases proceed from gate 1 to 4 or 5, depending upon the position, and then return to the start position. After motion correction the diaphragm is almost stationary with the profiles from all gates falling together at the correct position (Fig. 8.2, right). The displacement of the heart analysis on the phantom data showed the extent of motion to be 20.7, 3.9, 2.6, 2.2, 1.8, 2.0 millimeters for the original, LK, HS, B-S, B-NL, and the DP algorithms respectively.

The CC results before and after motion correction with all algorithms on the phantom data are given in Table 8.1. The CC improves in all respiratory phases after motion correction to values closer to 1. The values after motion correction are relatively constant over the respiratory phases and do not decrease much with increasing distance from the target gate. The last line of the table shows the average CC calculated over all gates. The average shows that B-NL and DP algorithm give practically same results. No significant differences could be found between the results given by the different algorithms per the

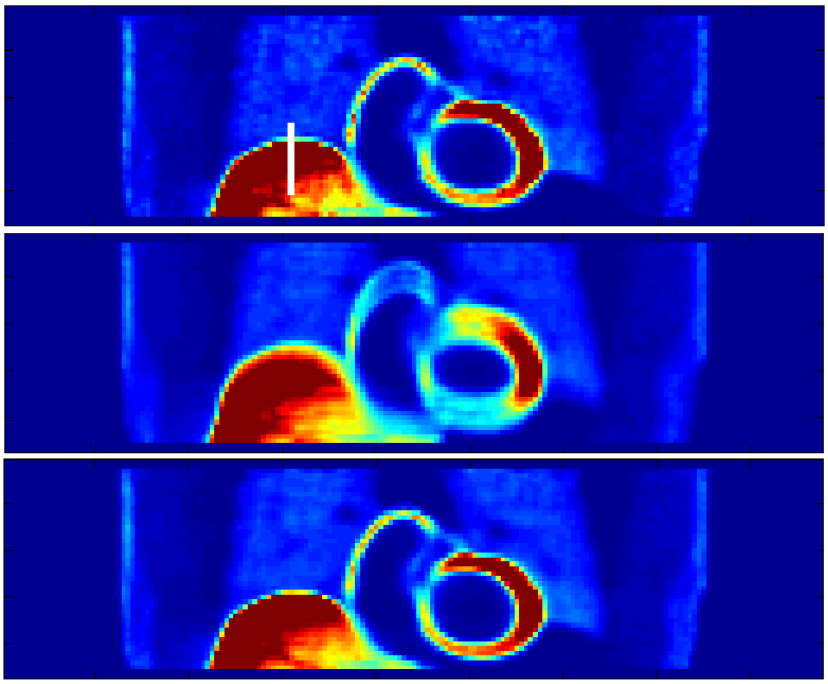

Figure 8.1: The results of motion correction using the DP algorithm on NCAT phantom. A coronal slice showing the liver and the heart. Top: The target image, the gray line shows the position of profiles given in figure 8.2. Middle: the summed image without motion correction. Blur at the base of the lungs and the motion of heart are clearly visible. Bottom: The summed image after motion correction. The blur as well as the heart motion has been corrected to a large extent.

paired student's t-test as all results are very similar to each other (0.9751 ± 0.0029).

8.2 Patient data: Heart displacement

The results of the heart displacement on the real patient datasets are given in Fig 8.3. The columns show the maximum motion of heart among all eight respiratory phases for each of the 11 patients. The twelfth dataset gives the average values. The heart displacement (in mm) is shown for the uncorrected data as well as for the motion-corrected data. The average motion before motion correction was 9.9 mm. It was reduced to 2.9 mm for LK, 2.7 mm for HS, 2.6 mm for B-S, 2.5 mm for B-NL, and 2.5 mm for DP algorithm. The one-voxel resolution is marked with an extra dotted-line. The p-values for the significance of the results given by the HS B-S, B-NL, and DP algorithms against the previous work by the authors (LK algorithm) were 0.248, 0.194, 0.052, 0.041 respectively. Significance values for the DP-algorithm against all other methods were 0.041, 0.045, 0.381, and 0.451 respectively. These results are discussed below in the discussions part. The exact values are given in the Table 8.2.

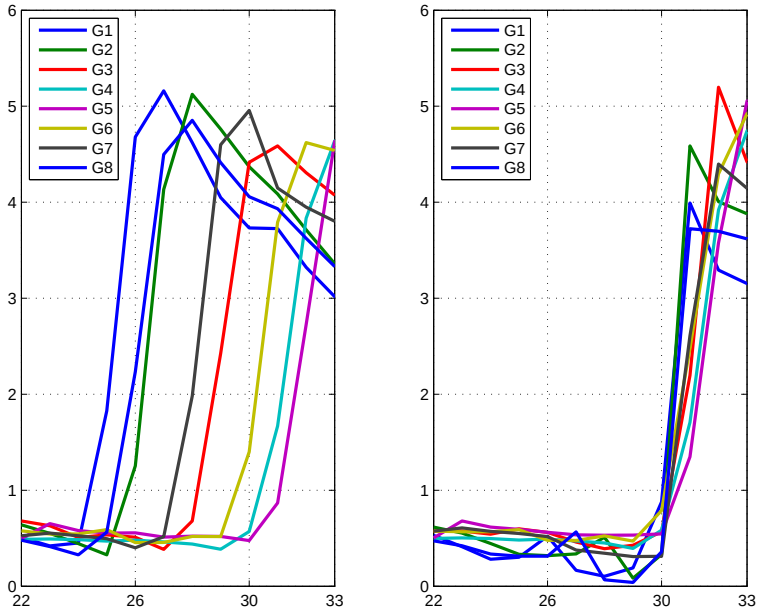

Figure 8.2: Line profiles of the phantom data along the line shown in Fig. 8.1. Left: before motion correction, right: after motion correction. G4 was selected as the target gate.

8.3 Patient data: Correlation coefficient

The CC results of one representative patient dataset are shown in Table 8.3. Gate G4 was selected as the target gate. As expected, gates which are farther away from the target gate have lower CC values. This remains true after motion correction. The performance of the algorithms on this single dataset can be judged by the average CC values given in the last row of the table.

The CC results for all sixteen patients included in the study are given in Table 8.4 and shown in Figure 8.4 for better visual assessment. The x-axis shows the patients whereas the y-axis shows the CC of the first gate with the target gate (G4). The average of all sixteen datasets is given in the last column. Results for the Original, LK, HS, B-S, B-NL, and DP algorithms are plotted in the graph. The average CC for all patients were 0.9404, 0.9825, 0.9844, 0.9830, 0.9846, and 0.9845 for the Original data, the LK, HS, B-S, B-NL and the DP algorithms. The results are also given in the Table 8.4.

The p-values of significance of HS B-S, B-NL, and DP algorithms against the LK algorithm were 0.044, 0.585, 0.005, and 0.006 respectively. Similarly, the significance values of the results of the DP-algorithm against the other algorithms were 0.006, 0.757, 0.046, and 0.055. The CC results are also shown in the form of a plot in the Fig 8.4. It is readily visible from the figure that the improvement in the CC is large between the original images and any of the motion corrected datasets. Also, that the CC after motion correction with any of the methods has become more or less similar for all patients as compared to the large variance in CC among the patients on original, not motion

Table 8.1: Correlation Coefficients with DP algorithm on Phantom Data

	Original	LK	HS	B-S	B-NL	DP
G1	0.7534	0.9296	0.9352	0.9335	0.9423	0.9423
G2	0.7943	0.9530	0.9509	0.9468	0.9608	0.9608
G3	0.9124	0.9901	0.9895	0.9886	0.9909	0.9909
G4	1.0000	1.0000	1.0000	1.0000	1.0000	1.0000
G5	0.9895	0.9954	0.9953	0.9962	0.9963	0.9963
G6	0.9772	0.9941	0.9937	0.9948	0.9949	0.9949
G7	0.8680	0.9841	0.9738	0.9756	0.9831	0.9833
G8	0.7820	0.9458	0.9468	0.9421	0.9951	0.9553
Avg	0.8846	0.9740	0.9731	0.9722	0.9779	0.9780

Table 8.2: Displacement of Left Heart Ventricle [mm]

Patient	Original	LK	HS	B-S	B-NL	DP
P1	21.5	6.8	5.2	5.0	5.0	5.1
P2	8.7	2.4	2.4	2.0	2.4	2.4
P3	4.3	1.3	1.3	1.2	1.3	1.2
P4	11.2	3.0	3.1	3.4	2.9	2.9
P5	3.9	1.1	1.1	1.4	1.1	1.1
P7	13.7	3.1	2.9	3.2	2.9	2.8
P8	8.6	2.4	2.4	2.0	2.3	2.3
P9	6.6	2.1	1.9	1.6	1.8	1.8
P10	10.0	4.2	4.4	4.3	3.5	3.5
P14	13.5	3.5	2.9	2.7	2.7	2.6
P16	6.6	1.7	1.7	1.8	1.7	1.6
Average	9.9	2.9	2.7	2.6	2.5	2.5

Table 8.3: CC Results for Patient P11

Gate	Original	LK	HS	B-S	B-NL	DP
G1	0.9284	0.9415	0.9659	0.9690	0.9706	0.9708
G2	0.9665	0.9704	0.9778	0.9778	0.9782	0.9783
G3	0.9665	0.9703	0.9779	0.9781	0.9782	0.9783
G4	1.0000	1.0000	1.0000	1.0000	1.0000	1.0000
G5	0.9657	0.9709	0.9780	0.9779	0.9779	0.9777
G6	0.9691	0.9727	0.9779	0.9778	0.9782	0.9783
G7	0.9667	0.9715	0.9780	0.9781	0.9783	0.9783
G8	0.9373	0.9505	0.9724	0.9713	0.9732	0.9735
Average	0.9625	0.9685	0.9785	0.9787	0.9793	0.9794

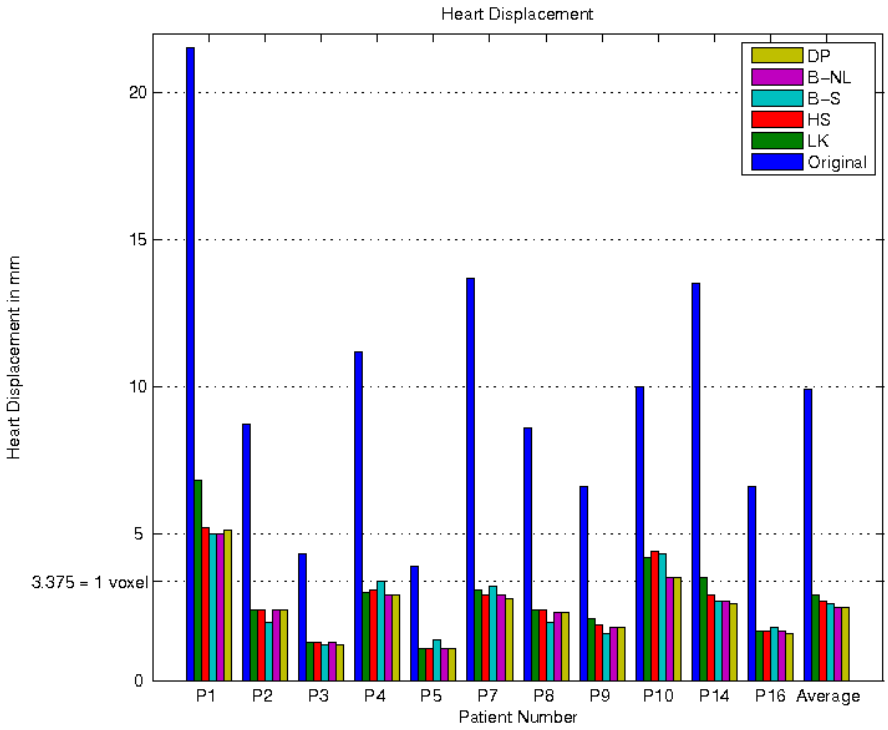

Figure 8.3: Motion of the heart in mm as measured with the center of mass of the left ventricle on patient data. Results for 11 Patients and the average are shown along the x-axis.

corrected, images. Further discussion of these results is presented in the discussions section.

8.4 Patient data: Reduction in noise

Table 8.5 shows the noise values on all sixteen patient datasets for the target gate, as well as the values for the sum of all gates before motion correction and the sum of all gates after DP based motion correction. The results for all other algorithms were essentially the same. As expected, the amount of noise decreases in both summed images. After motion correction the noise level is similar to that of the uncorrected summed image.

8.5 Patient data: Impact of noise

Results of the performance of different algorithms in presence of varying amount of noise are given in Fig 8.5. Only the average CC for all sixteen patients is given for better readability. It is obvious from the figure, that the CC values decrease with increasing noise levels. The results for the HS, B-S, B-NL and the DP algorithms are always better than the LK algorithm. The performance of the B-NL and the DP algorithms is virtually the same the difference being less than 0.0003 for any noise level. The results can also be seen in Table 8.6. The values are given in table 8.6.

Table 8.4: CC Results of all Patients. See also Fig 8.4

Patient	Original	LK	HS	B-S	B-NL	DP
P1	0.8436	0.9619	0.9702	0.9667	0.9722	0.9719
P2	0.9422	0.9851	0.9860	0.9843	0.9849	0.9847
P3	0.9722	0.9882	0.9891	0.9890	0.9895	0.9894
P4	0.9348	0.9822	0.9832	0.9804	0.9827	0.9826
P5	0.9674	0.9881	0.9883	0.9887	0.9889	0.9889
P6	0.9522	0.9778	0.9811	0.9813	0.9818	0.9817
P7	0.8622	0.9812	0.9856	0.9740	0.9826	0.9829
P8	0.9445	0.9871	0.9880	0.9866	0.9880	0.9880
P9	0.9621	0.9936	0.9939	0.9931	0.9936	0.9936
P10	0.9440	0.9759	0.9853	0.9844	0.9801	0.9801
P11	0.9779	0.9834	0.9788	0.9803	0.9838	0.9838
P12	0.9693	0.9900	0.9907	0.9907	0.9913	0.9912
P13	0.9446	0.9818	0.9841	0.9833	0.9840	0.9840
P14	0.9282	0.9698	0.9701	0.9701	0.9733	0.9729
P15	0.9418	0.9860	0.9859	0.9866	0.9872	0.9870
P16	0.9594	0.9885	0.9895	0.9887	0.9900	0.9899
Avg	0.9404	0.9825	0.9844	0.9830	0.9846	0.9845

Table 8.5: Noise on PET Images

Patient	target gate	uncorrected sum	DP corrected sum
P1	250	119	114
P2	165	80	74
P3	250	110	101
P4	355	184	189
P5	166	87	80
P6	570	250	235
P7	120	65	64
P8	215	114	111
P9	89	46	45
P10	206	130	116
P11	231	142	131
P12	632	373	365
P13	303	160	148
P14	383	201	193
P15	152	85	86
P16	286	158	166
Average	273	144	138

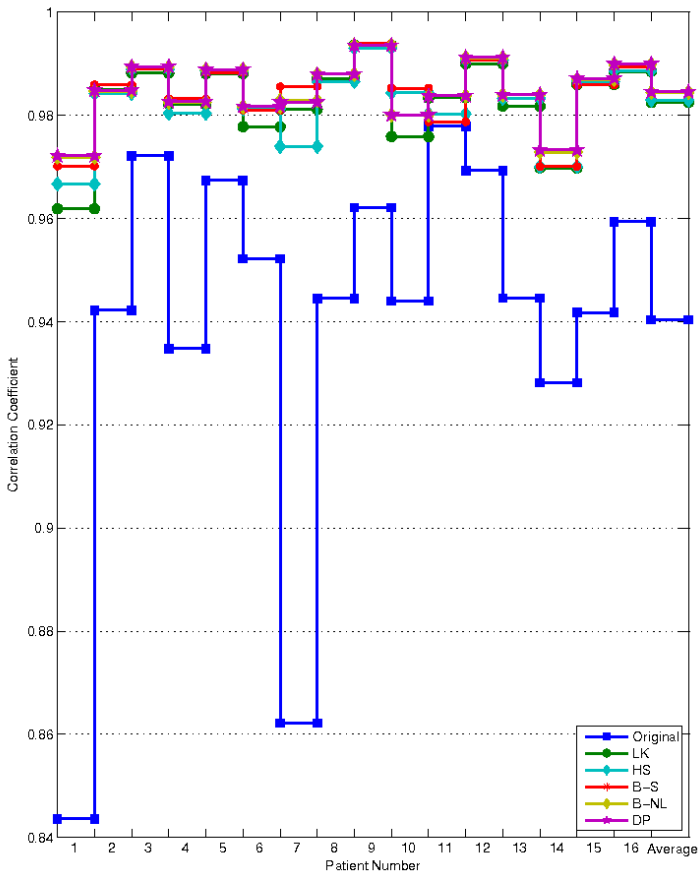

Figure 8.4: The results of the CC analysis for all sixteen patients for the Original data, and the LK, HS, B-S, B-NL, and DP algorithms.

Table 8.6: CC Results on Noisy Data

Noise level	Original	LK	HS	B-S	B-NL	DP
100	0.8849	0.9348	0.9389	0.9379	0.9389	0.9386
75	0.8523	0.9133	0.9191	0.9178	0.9188	0.9186
50	0.7997	0.8718	0.8781	0.8777	0.8792	0.8788
25	0.7036	0.7988	0.8097	0.8093	0.8101	0.8095

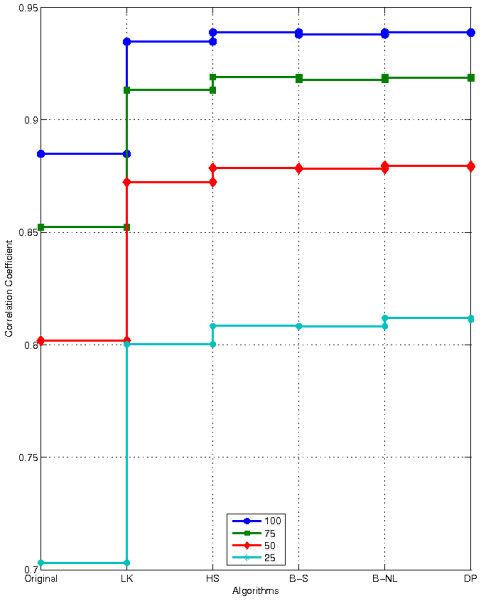

Figure 8.5: The correlation coefficient results on 100%, 75%, 50% and 25% of PET data. The correlation increases after motion correction at all noise-levels. The performance of the algorithms relative to each other is not influenced by the noise level.

Chapter 9

Discussion of Results

The results presented previously are now discussed in the following sections.

9.1 Phantom data

The results on the phantom data show that the motion of the heart in the images is reduced by over 90% by the advanced (B-S, B-NL, DP) algorithms, whereas the reduction is 81% with the LK algorithm. The differences between the advanced methods are minimal (2.0±0.2 mm) when seen against the image resolution of 3.375 mm. There were no significant differences between the results by any of the motion correcting algorithms on phantom data. This may be due to the good performance of the algorithms on phantom data. The results varied by less than 0.3% around the mean (0.9751). Although no significance can be found according to the student's t-test, probably because of the low number of datasets, a tendency towards higher CC is visible for the B-NL and the DP algorithms (0.9779, 0.9780).

9.2 Patient data: Heart displacement

The displacement of the heart on patient data shows that the heart motion was reduced substantially by all motion correction methods. It also shows that all methods perform well (motion reduced from 9.9 mm in average to 2.6 mm). The advanced algorithms (B-S, B-NL, DP) performed almost equally, as expected, because they are all derived from the HS algorithm and thus similar to each other. The advanced DP algorithm performs significantly better than the LK and the HS methods, as shown by the student's t-test. The B-S algorithm performs better on some datasets (Patients 1,2,3,8,9,14), whereas poorer than LK algorithm on others (Patients 4,5,10,16). We think that more datasets are required to clearly decide the significance of the results by B-S algorithm. The B-NL algorithm showed results similar to DP algorithm. The good performance of B-NL and DP algorithms is due to the advantages of both LK and the HS algorithms which are contained in them. The improvement in motion reduction is independent of the magnitude of motion. Thus the DP-algorithm performed similarly on data from patient P1 with 21.5 mm motion (improvement 76.3%) and on patient P3 with 4.3 mm motion (improvement 72.1%).

The heart motion was corrected to 2.64 mm on average which is less than the voxel resolution of our images (3.375 mm). With an intrinsic PET data resolution of around

6 mm in our studies, we can consider the motion to have been corrected sufficiently as the residual motion is much lower than both the intrinsic PET resolution and the pixel resolution of the images.

9.3 Patient data: Correlation coefficients

As with the displacement of heart criterion, the advanced algorithms show better performance than the LK method. There are individual differences in the results from both analysis. For example in P2 the best performance, according to the heart displacement analysis, was shown by the HS algorithm, whereas the best performance on correlation analysis is shown by the B-NL and the DP algorithms. This and other such differences might be caused by two factors. First, the heart motion method is calculated on segmented images, whereas the correlation is performed on whole data volumes. Secondly, other organs and especially the noise have large influence on the correlation analysis, whereas they are not present on the images for heart displacement analysis. Despite small differences the tendency for the advanced algorithms to be better than the LK algorithm is visible as all algorithms (except B-S) are significantly better than LK. Significance analysis shows the DP algorithm to be better than LK and B-S algorithms. Strangely, the results against the HS algorithm were not found to be significantly better.

9.4 Influence of interpolation on CC

The CC values are influenced by the interpolation methods used to deform the images to the target position because they also depend on the voxel intensities. To estimate the influence of interpolation methods on the results achieved by motion correction the following method was adopted. First the motion vectors were calculated. The image volume was than deformed with these motion vectors using interpolation. The CC of this deformed volume against the original volume was then calculated. In the second step, the already deformed volume was moved back to the original position using the same interpolation method and the CC was calculated again. The resulting image volume was thus twice interpolated. The method was applied to all datasets. Average CC of the moved images with one interpolation step against their original position was 0.9130, which indicates large deformation. The average CC of the images moved back to the original position and thus with two interpolation steps was 0.9949. Thus, the two interpolation steps degraded the CC value by 0.0051. A single move, respectively one interpolation step, would therefore change the CC by about 0.0025. This means that the improvement in CC values after motion correction (0.0434 on average, see results section) cannot be attributed to interpolation as it is over 17 times larger than the effect of interpolation. It should be noted that even this influence is not crucial to our findings as we compare the results of different algorithms relative to each other containing the same interpolation methods.

9.5 Reduction in noise

It was assumed earlier that motion correction leads to improved image quality when all respiratory phases are combined. The analysis of reduction of noise on the images, which

is an indicator of the image quality, supports this assumption. The standard deviation of voxel intensities in a homogeneous region of interest for the target gate was 273, that for the motion corrected images was 138, which is similar to the uncorrected summed image (144). Thus, motion correction does really improve the quality of the images with respect to noise. The slight decrease (1%) in noise level on the sum of motion corrected images, as opposed to the sum of the uncorrected images, is probably due to the effects of smoothing performed during motion correction.

9.6 Impact of noise

The analysis of the data for all patients and all noise levels for all algorithms (4 noise levels, 16 patients, 8 respiratory phases per patient) showed that the advanced algorithms are significantly better than the LK algorithm (p=0.000, 0.005, and 0.003 respectively). The increasing distance between the noise levels is the simple result of the fact that offsets of different length were used to remove the beginning part of the listmode-data to get the noise levels. As the radioactive substance decays lesser number of events are registered in the scanner and this the noise increases additionally due to the radioactive decay.

These results are in accordance with our expectations, as the advanced algorithms perform better in presence of large amounts of noise. The DP algorithm and the B-NL algorithm virtually the same as there is only a small theoretical difference between them. The tendency towards better results for the DP algorithm in presence of larger amount of noise, indicated by increasing significance against LK algorithm, is probably caused by the modified smoothness term in the DP algorithm.

9.7 Parameter values

As described before (see section 7.10), the parameters or the algorithms were optimized automatically with the help of genetic algorithms. As it is not possible to give the optimized values for all parameters for all algorithms and for each patient separately, the average of optimized values are given in table 9.1.

Table 9.1: Average of Optimized Parameters, see table 7.1 for further description

Algorithm	window size	α	β_1	β_2	ω	inner loops	outer loops
LK	3						
HS		312				96	
B-S		399				199	
B-NL		54	4	4	1.4	112	4
DP		60	3.4	4.6	1.4	115	3

The parameters show some properties which allow interesting conclusions. The parameters for the B-NL and the DP algorithms are very similar to each other. Thus α is 54 for B-NL and 60 for the DP algorithm. The parameter ω is same in both and the number of inner loops and outer loops is also very similar. This result is in accordance with the expectations as both algorithms are based upon the same mathematical equations. In the

same way the parameters for the HS and the B-S algorithms also show some similarity, although it is not so strong as that between the B-NL and the DP algorithms. Thus the parameter α is 312 for the first and 399 for the second method. It is also interesting to note that these values are significantly different from the values for the B-NL and DP algorithms. This fact may be explained by the basic difference in the underlaying equations as B-NL and DP algorithms use the non-quadratic whereas HS and B-S methods use the quadratic penalization of the outliers. Apparently the quadratic penalization coupled with the absence of the scaling term β leads to a stronger need for smoothness.

Chapter 10

Multi-Resolution Method

The DP algorithm as presented so far is robust enough to be used with noisy images. However, owing to the basic definitions of optical flow i.e the image constraint equation (eq. 7.2), all optical flow algorithms become inaccurate in estimating the deformations with increasing motion as the taylor expansion of the equation uses only the first terms and neglects the higher order terms. With large motion, however, the higher order terms become important and the optical flow calculated with present methods inaccurate. This fact is depicted in figure 10.1 where the result of an optical flow deformation with large displacement is shown.

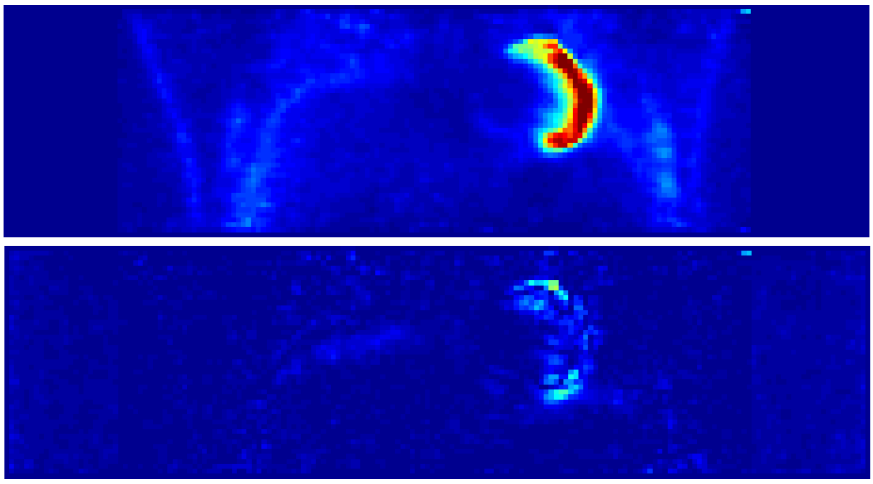

Figure 10.1: Estimates of deformation are inaccurate when large displacements are present on the image volumes. Top: Deformed image with large displacement showing miscalculations at the top and the bottom of the left heart ventricle. Bottom: The absolute differences between the deformed and the target image show the extent of errors. See also figure 10.6.

10.1 Large Motion on PET Images

Before making an attempt to solve the problem of large motion on PET images. It would be helpful to consider how often such large motion is present on real patient data. Every

type of motion that exceeds 1 voxel per frame is considered 'large motion' for optical flow algorithms. Keeping this definition, it can be seen from the results presented in the table 8.2 that out of 11 patients, where the displacement of the heart could be calculated, all eleven showed larger motion than 1 voxel (= 3.375 mm). This total motion was divided into eight gates non-uniformly by the application of the 'Variable Amplitudes' based gating method. As the motion between the target and the floating gates is always estimated directly, the above mentioned facts require estimation of large motion among some gates i.e. those which are farther away from the target gate.

These findings on our data are also supported by other researchers. Brandner et al. [11] measured the motion of different organs in the abdomen in 13 patients. Their results show that all 13 patients had motion larger than 4 mm for the liver. Similar results were found for the kidneys and spleen. Seppenwoolde et al. [102] measured the motion of tumors due to respiration and found that out of 21 patients, 9 patients had motion greater than 3.375 mm.

In view of above findings, it can be safely assumed that large displacements exist in most cases on the respiratory gated data. Thus it is necessary to extend the algorithm in some way to accommodate larger displacements of objects on the images.

10.2 Solution for Large Displacements

The problem of large motion for optical flow estimation can be dealt with using two options:

10.2.1 Larger Window Size

Using a larger window size for the estimation of derivatives allows the algorithm to consider larger displacements. However, this approach has a negative impact. In the Lukas/Kanade part of the algorithm, it is assumed that the flow is constant in a small window. Increasing the window size contradicts with this assumption. Thus the window size cannot be increased above a small limit.

10.2.2 Multi-Resolution approach

The problem can be divided into smaller parts by using a coarse-to-fine model. The total displacement present on the images, which is large, is automatically divided into smaller parts, in terms of voxels, when the resolution of the images is degraded. Thus a displacement of 4 voxels on the original images will be reduced to 2 voxels if the resolution is reduced to one half, whereas increasing the resolution to twice the original will lead to 8 voxels in displacement. Using the results calculated at a coarser level to modify the images at the finer level allows the problem to be solved step-by-step.

As this is the approach used by the most recent studies ([56],[110],[14],[2]), it will be applied in this study too. Lee et al.[56] use a image-pyramid approach. Thomas et al.[110] use a quad tree decomposition of the original image to apply multi-resolution optical flow, whereas Bruhn et. al[14] and Alvarez et al.[2] apply a full multi-scale approach which allows free choice of resolution steps by convolutions with a gaussian function. For PET data, the image-pyramid approach is sufficient due to the inherent low resolution of the images, as will be proved by the results.

The motion or displacement on original images can thus be given as:

$$f(I_o) = f(I_l) + f(I_h) \tag{10.1}$$

where $f(I_o)$ denotes the motion on original images, $f(I_l)$ denotes the motion estimated at the lower resolution and scaled up with the same factor, and $f(I_h)$ denotes the *remaining* motion present on the images in original size, already corrected for $f(I_l)$.

The multiresolution strategy is implemented in this study along the following lines (see also figure 10.2). In the first step the images are reduced by one half in resolution, thus also reducing the object displacements by one half in terms of voxels. As the optical flow algorithms can deal with the reduced displacements much more accurately than with the original larger displacements, the flow vectors are calculated on these reduced-resolution images with the help of the DP, or any other, algorithm. The deformation vectors obtained from the algorithm are now magnified by a factor of two and applied to the original images. Thus the motion on the original images is reduced by the part that was calculated in the first step on low resolution images. The remaining motion is than estimated on these motion corrected and full resolution images and corrected per normal procedure.

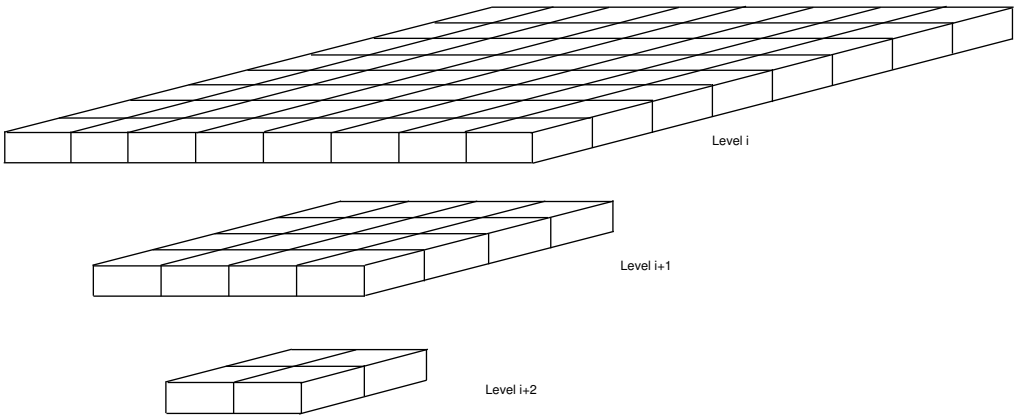

Figure 10.2: Multi-Resolution Scheme.

The algorithm can be given for two levels as follows:

```
reduced_img_vol = Reduce(img_vol)
reduced_vectors = Optical_Flow(reduced_img_vol)
upscaled_vectors = UpScale(reduced_vectors)
new_img = Deform(img_vol,upscaled_vectors)
vectors = Optical_Flow(new_img)
Result= Deform(new_img, vectors)
```

10.3 Reduction of resolution

Many methods of reduction in resolution can be conceived. In the case of unweighted reduction, every second voxel is selected to get the next level. However, this leads to artificial edges with high gradients at the organ boundaries as can be seen in figure 10.3. Therefore the so-called Gaussian-Pyramid method [17] was used in this study. In this

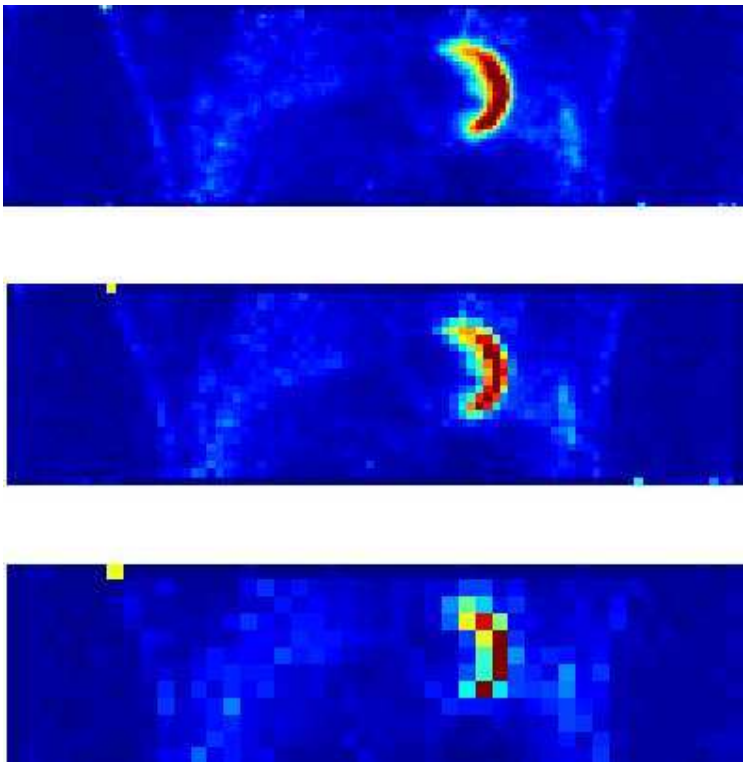

Figure 10.3: Effect of resolution reduction on images. From top to bottom: Original resolution, half and one fourth resolution PET images. In this case the reduction was done without any weighting.

method the images are reduced using a weighted sum of adjacent voxels. The weighting function selected for this purpose is a Gaussian-kernel. The sum of five adjacent pixels is used to create the next level of low-resolution images in the 1D case. In the 3D case, a $5 \times 5 \times 5$ matrix is used. The results of such a reduction scheme can be seen in figure 10.5. The difference in the lowest level of resolution between the two methods is clearly visible in the figures 10.3 and 10.5.

It should be noted that the smoothing effect of the Gaussian-Pyramid scheme does not effect the results in terms of voxel intensities. This is due to the simple reason that the final deformation is done on the original images and not on the reduced images.

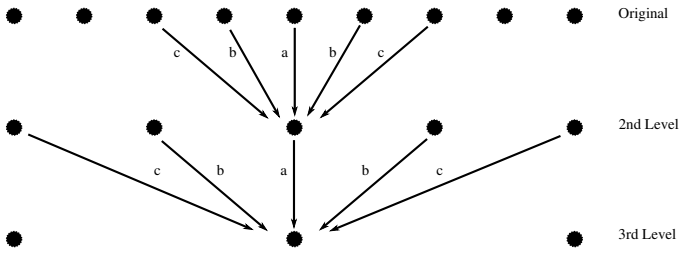

Figure 10.4: 1D Gaussian Reduction Scheme. The weighted sum of the five neighboring pixels is used to create the next level of reduced images with one half of the original resolution.

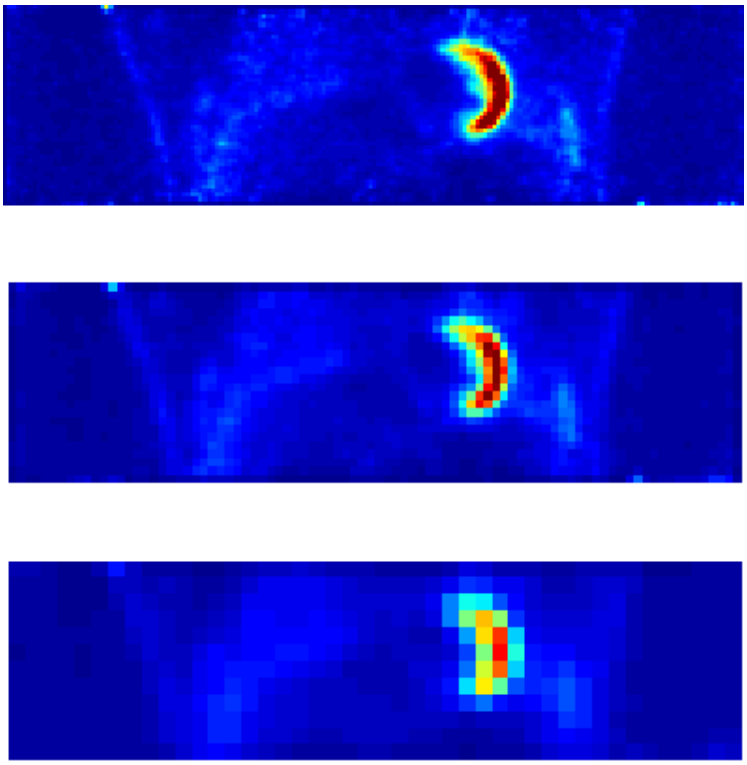

Figure 10.5: Resolution reduction with the Gaussian-Pyramid method, reduction factor is 2.

10.4 Upscaling the flow vectors

The vectors estimated at the lower resolution images have to be upscaled, in our case by the factor 2, to be applied to the next higher level of resolution. After comparing different methods, linear interpolation was used to achieve this, as this method gave the best results. The flow vectors have not only to be interpolated to find the values between adjacent vectors at the lower resolution, but also to be magnified by the resolution factor. This is necessary, as the displacement of 1 voxel at lower resolution corresponds to a displacement of 2 voxels at the next higher resolution level.

10.5 Results

The original resolution of the images used for the multi-resolution analysis was $128 \times 128 \times 64$. Each additional level of resolution reduced the resolution by half in all three dimensions. In the following tests the 3D images were motion corrected by using, one, two, and three levels of resolution with the help of the Gaussian-Pyramid algorithm described above in the section 10.3. The results of the multi-resolution approach can be seen in figure 10.6.

The parameters, such as the smoothing parameter α, the scaling parameters β_i, the number of iterations etc, used for motion correction were optimized for each patient manually. For all experiments with a particular patient dataset, the parameters were kept constant, only the number of levels was varied.

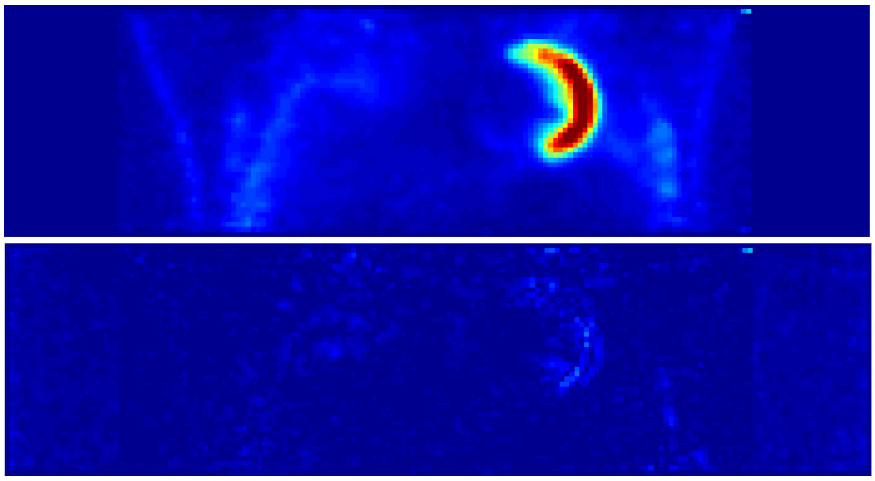

Figure 10.6: The results of the Multi-Resolution-DP algorithm. Top: Deformed image with large displacement showing that the motion estimation was correct. Bottom: The absolute differences between the deformed and the target image show that the errors are minimal. See also figure 10.1.

Table 10.1: Correlation Coefficients with Multi-Resolution-DP algorithm on Patient P 4 [in %, target gate=1]

	G 1	G 2	G 3	G 4	G 5	G 6	G 7	G 8	Avg
Original	1.00	0.9524	0.9015	0.8432	0.8229	0.8279	0.7634	0.7337	0.8556
1 level	1.00	0.9859	0.9819	0.9802	0.9787	0.9790	0.9731	0.9733	0.9815
2 levels	1.00	0.9911	0.9896	0.9876	0.9873	0.9878	0.9856	0.9854	0.9893
3 levels	1.00	0.9915	0.9906	0.9900	0.9899	0.9901	0.9896	0.9894	0.9914

10.5.1 Correlation Coefficient

The results for the correlation correlation measure for a typical patient are reproduced in Table 10.1 (see also Fig 10.7). The correlation of the target gate with itself is of course 100% and it decreases as we move towards gates farther away from the target gate until it reaches 85.56% for gate number 8. For any given gate, except the target gate itself, the correlation increases with increasing number of levels used for the multi-resolution algorithm, e.g. it is 85.56% for the uncorrected data for gate 8 and increases to 98.15% for one level, to 98.93% for two levels and to 99.14% for three levels. Same results are seen in all other gates.

Table 10.2 gives an overview of correlation coefficient results for all eight patients, see also Fig 10.8). In this table only the correlation coefficients for Gate 8, which is the farthest from the target gate, are shown for all patients. Thus the correlation of Gate 8 with the target gate was 91.03% for Patient 6 before motion correction. It increased to 97.89% after motion correction. This result was further improved by using 3 levels of resolution to 99.28%.

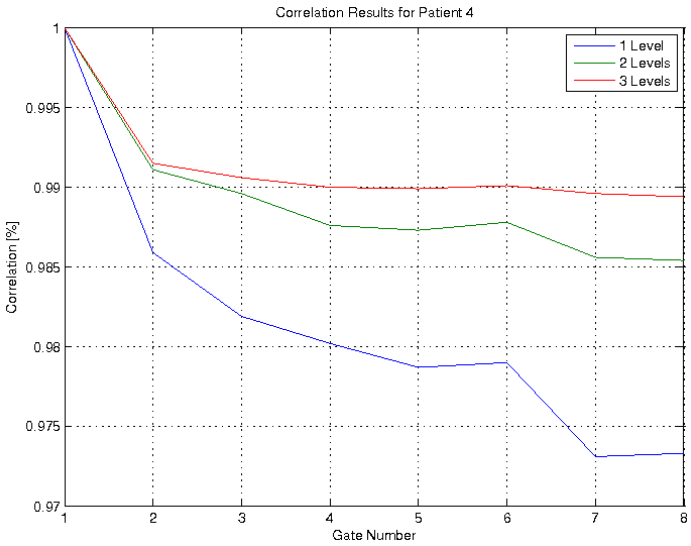

Figure 10.7: The results of the Multi-Resolution-DP algorithm for Patient P 4 presented in a plot for easier comparison.

Table 10.2: Correlation of Gate 8 with the Target Gate [target gate=1]

	P 1	P 2	P 3	P 4	P 5	P 6	P 7	P 8
Original	0.6422	0.8398	0.8580	0.7337	0.8626	0.9103	0.7926	0.8770
1 Level	0.9040	0.9542	0.9681	0.9733	0.9811	0.9789	0.9634	0.9559
2 Levels	0.9176	0.9740	0.9732	0.9854	0.9838	0.9907	0.9676	0.9637
3 Levels	0.9174	0.9777	0.9739	0.9894	0.9849	0.9928	0.9672	0.9650

10.5.2 Displacement of Heart

Lastly the results for the displacement of the heart criteria are given in Table 10.3(see also Fig 10.9). The results show that the displacement of the heart is reduced significantly when motion correction is applied to the images. In most patients the displacement is further reduced by using the multi-resolution approach to almost 1 mm when two levels of resolution are used. The residual displacement is halved by using three levels.

10.6 Discussion of Results

Table 10.1 makes it clear that the results of motion correction depend upon the amount of motion present in a particular gate. Thus gates which lay farther from the target gate show lower correlation with the target gate before motion correction. This correlation is increased after motion correction in all gates. However, the results for gates nearer to the target gate are better than those for the gates farther away. The average correlation of all gates with the target gate was 85.56% before motion correction and 98.15% afterwards. The result for Gate 2 is 98.59% whereas that for Gate 8 is 97.33%. The good news is that using the multi-resolution strategy of the DP-algorithm can resolve this problem to a

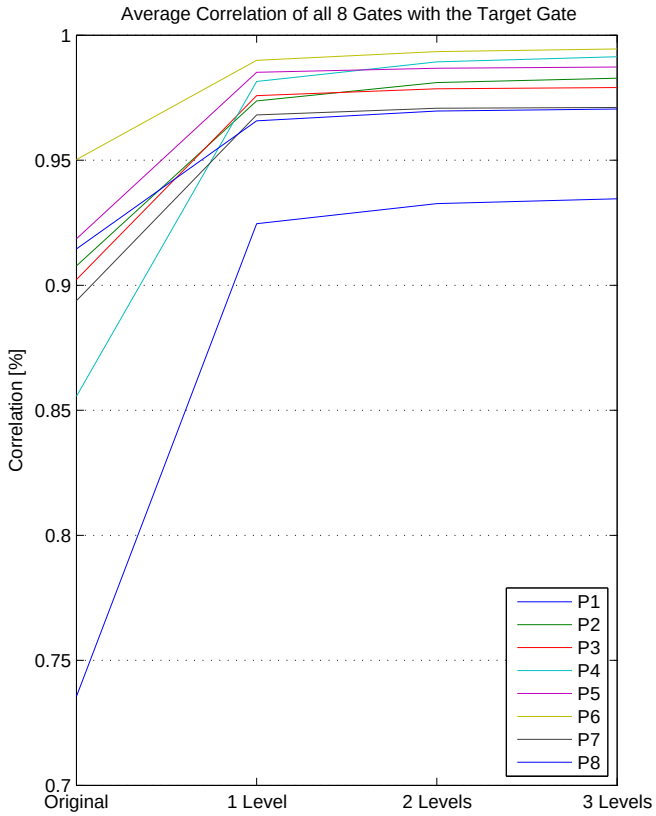

Figure 10.8: The mean correlation of all gates with the target gate for all patients.

large extent. The average correlation is not only increased to 99.14%, but also the results for all gates become much more similar. This can be seen more readily in Fig. 10.7 where the plotted curve for multi-resolution algorithm with three levels is almost horizontal for Gates 2 to Gate 8. Similar results were seen in all other patients.

Table 10.2 shows that the results mentioned above are not confined to a single patient. For all patients the results are improved by using the multi-resolution based approach. The improvement in the results is not that large as between the original and the motion corrected data. This may be due to the simple reason that the DP-algorithm is robust enough to deal with most of the motion by itself. The incremental benefit seems to vary from patient to patient, as can be concluded from figure 10.8. It is important to note that the correlation is increased in almost all datasets by using the multi-resolution approach.

Lastly, the results of the quantitative measurement of heart displacements shows how effective the multi-resolution approach is as compared to the single level application of the DP-algorithm. The motion of the heart was about 10.7 mm on average among the eight patients. This was reduced to around 3.0 mm after application of the single level DP-optical-flow-algorithm. At a voxel resolution of 3.375 mm^3 this means that the motion was reduced to less than a voxel on average. However, we can see that in patients with very large motion (patient 1, 21.6 mm) the residual motion is still large (9.3 mm). In

Table 10.3: Maximum Displacement of the Heart with the Multi-Resolution-DP algorithm [in mm, target gate=1]

	P 1	P 2	P 3	P 4	P 5	P 6	P 7	P 8	Avg
Original	21.6	8.6	12.4	13.6	8.8	6.8	6.9	6.5	10.7
1 level	9.3	2.0	2.8	3.1	1.6	1.5	1.9	2.0	3.0
2 levels	0.7	0.8	1.4	1.3	0.6	0.2	0.6	0.8	0.8
3 levels	0.4	0.4	0.7	0.7	0.2	0.2	0.1	0.2	0.4

such cases the multi-resolution approach delivers the greatest benefits (residual motion 0.7 mm for two levels). The results are further improved when three levels are used and the residual motion is reduced to less than 0.5 mm. At our voxel resolution, this means a stationary heart for all practical reasons. The overall results show that the residual motion is almost reduced by half when an additional level of resolution is used.

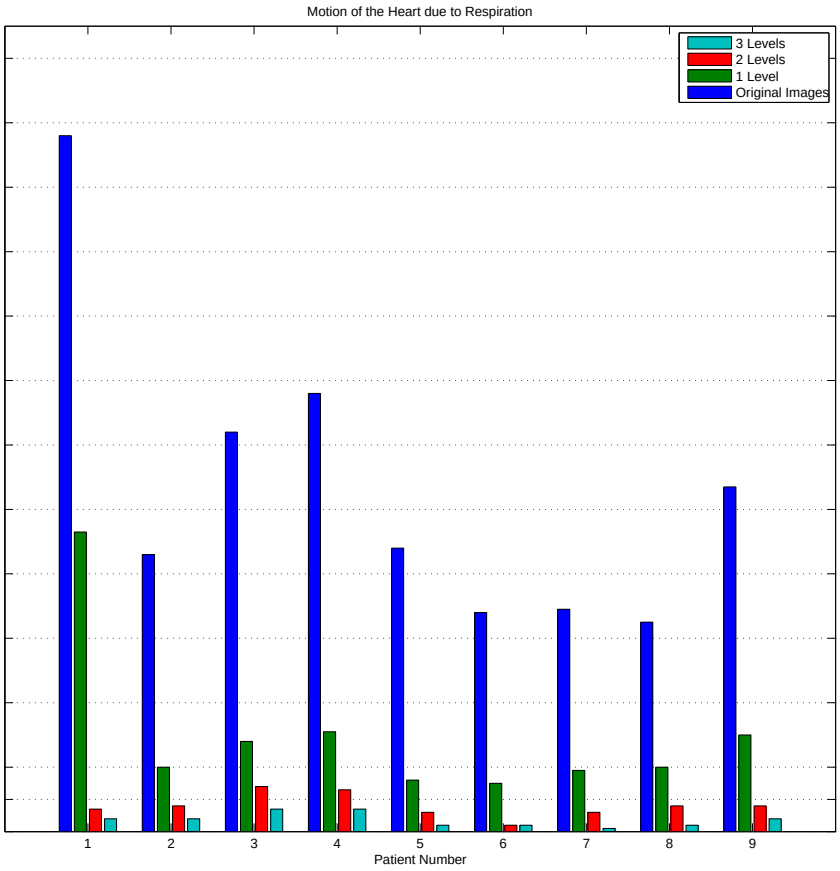

Figure 10.9: Results: Motion of the heart due to respiration on different patient datasets.

Chapter 11

CT Transformation

We have to deal with two different modalities in this study: PET and CT. The problem of motion in the case of the CT images is based partially on the non-correspondence between the PET and the CT data. The PET data has to be corrected for the effects of photon absorption inside the body. Dense tissue, like bones, absorb a larger part of the photons on their way to the detectors than soft tissue like lungs. This effect is corrected by scaling the number of photons registered in the detectors in accordance with the density of the tissue. In PET/CT scanners, CT data is used for attenuation correction. As the CT is acquired within seconds, it represents an almost instantaneous snapshot during the breathing cycle. Consequently, the CT data does not always correspond to the PET data (see figure 11.1). This non-correspondence leads to wrong attenuation because the CT data is used for attenuation of the PET data as described in the introductory chapter. This disparity is of clinical significance. It has been shown in studies with patients that the motion of lungs may lead to wrong staging [35] and mis-location of lesions [80]. Especially lesions near the lung base, which has the most pronounced motion, might constitute a significant problem [21].

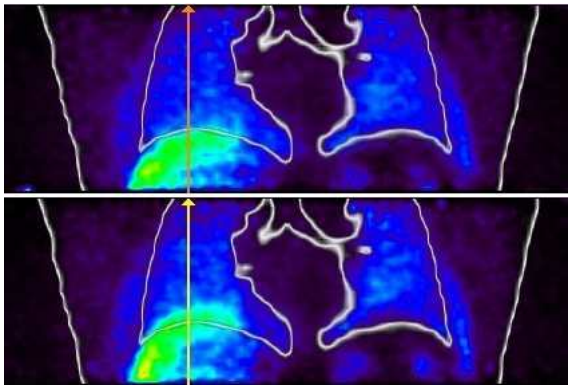

Figure 11.1: PET data does not correspond to static CT based *mu*-map in all respiratory phases. A coronal slice is shown from PET data overlaid with the CT data outline. The liver on PET data (green spot on the left), lies clearly inside the CT lung in some respiratory phases. The displacement was about 9 mm, see figure 11.2.

Motion correction of the PET data, therefore, solves only one part of the whole problem. The PET data should be attenuation corrected at the proper location before motion

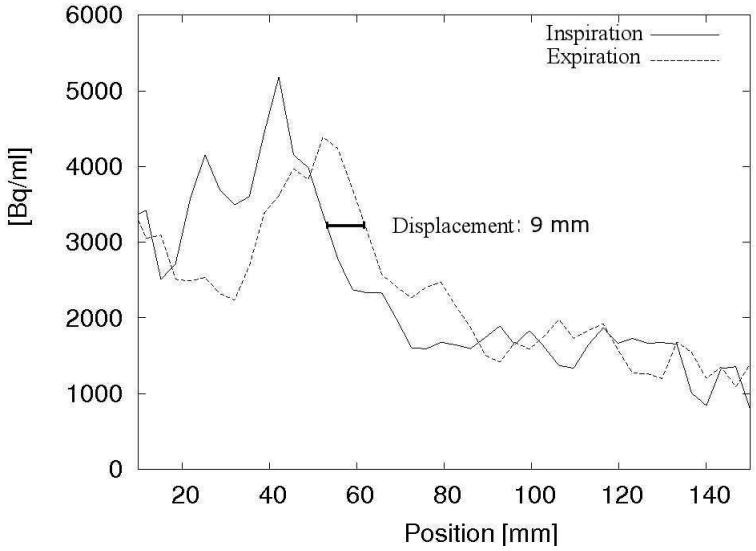

Figure 11.2: Profiles along the line shown in figure 11.1 allow the displacement on PET data to be measured, it is 9 mm.

correction because it was acquired at a specific location with the corresponding attenuation coefficient. Thus in figure 11.3, the voxel at position Pos 1 is moved to the target position, which corresponds to the position of the CT-attenuation-map, Pos 2. However, the attenuation correction should be performed with the coefficient AC 1, as the data in the voxel was acquired at that spatial position and not at the position with the coefficient AC 2.

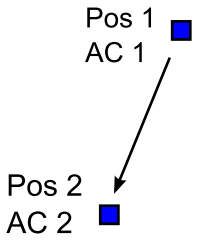

Figure 11.3: The problem of wrong attenuation map during motion correction. A voxel at Pos 1 is motion corrected and moved to the target position Pos 2. The voxel must be attenuation corrected with the attenuation factor AC 1 and not with AC 2 as it was acquired at Pos 1.

As we perform respiratory gating and use optical flow algorithms to extract motion vectors from the PET data using the combined local-global optical flow algorithm, the same method can be used to estimate the motion on PET data and apply it to the static CT images to obtain a series of different CT images. Corresponding PET and CT data is thus obtained for better attenuation correction. The process flow in this instance will be slightly different then previously. It is shown in figure 11.4. After the generation of the different CT respiratory phases, the PET data is attenuated with the help of the STIR package [1]. The results of this method are verified on both software phantom and real patient data.

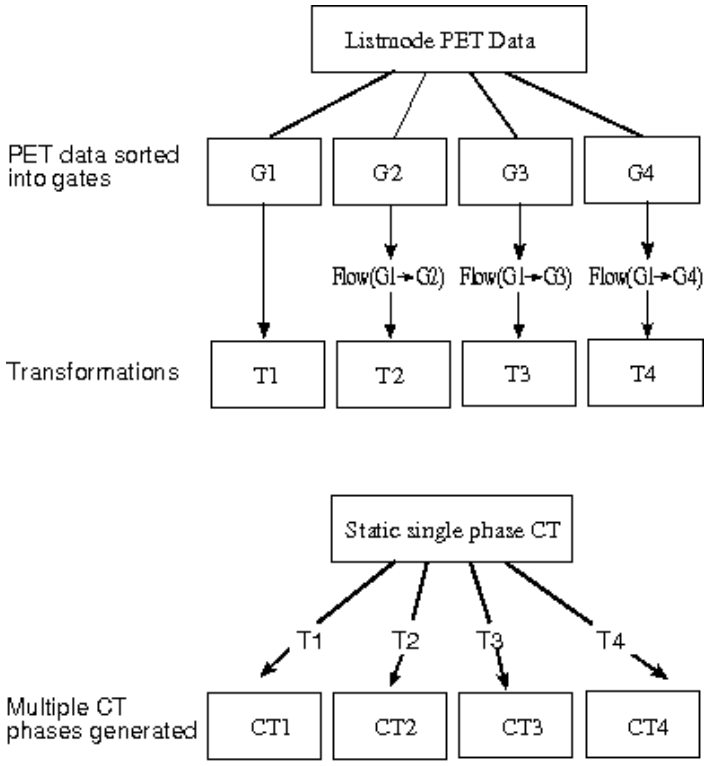

Figure 11.4: The process flow for the transformation of CT based *mu*-maps. Only four gates are shown to illustrate the principle.

11.1 Results and Discussion

Two types of data are used for evaluation: software phantom data and real patient data. The results on phantom data are given in Table 11.1. The CT phases were reconstructed as explained above from static CT and the motion information obtained from the PET data. The ground truth is present in the case of the software phantom data. The table shows that the ground truth CT phase 5 has only a correlation of 0.7041 with the static CT, i.e. they are very dissimilar. The correlation of the reconstructed CT phase 5 with the ground truth phase 5 on the other hand is 0.9250. This shows that the optical flow based reconstruction of phase 5 from the static CT has been very effective. The correlation of the other reconstructed CT phases with the corresponding ground truth CT phase is even better due to less amount of motion present in them.

Table 11.1: Correlation of reconstructed phases on software phantom data

	CT1	CT2	CT3	CT4	CT5	CT6	CT7	CT8
with static CT	1.0000	0.9600	0.8232	0.7041	0.6817	0.7510	0.8742	0.9811
with ground truth	1.0000	0.9897	0.9566	0.9250	0.9197	0.9377	0.9693	0.9948

Apart from software phantom data similar results were seen in patient data. In most

patient datasets, the static CT corresponds roughly to the first respiratory gate of the PET data as the CT is acquired in expiration phase (the numbering of gates is from expiration to inspiration in this study). Using the motion vectors between the first PET gate and all other gates, the CT respiratory phases were reconstructed as described previously (see figure. 11.7). The displacement of the liver on the PET images was calculated using the difference in position of the line profiles. It was found to be around 9 mm in the patient dataset shown in figure 11.2. The objective of the study was to transform the static CT so that it best adapts to this motion in PET data. Because not using the adapted CTs leads to wrong attenuation correction, see figure 11.5.

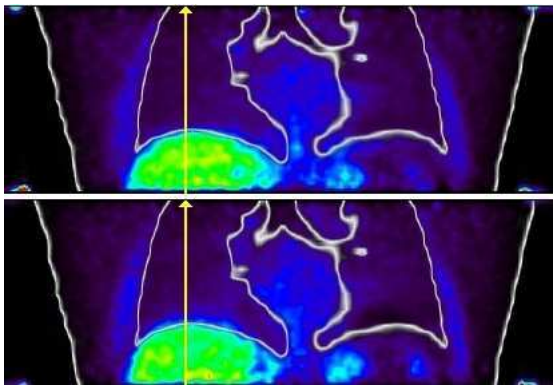

Figure 11.5: Using static CT data leads to wrong attenuation correction, the portion of PET liver inside the CT lung was wrongly attenuated. The displacement was thus found to be about only 2 mm on data attenuated with static CT, see figure 11.6.

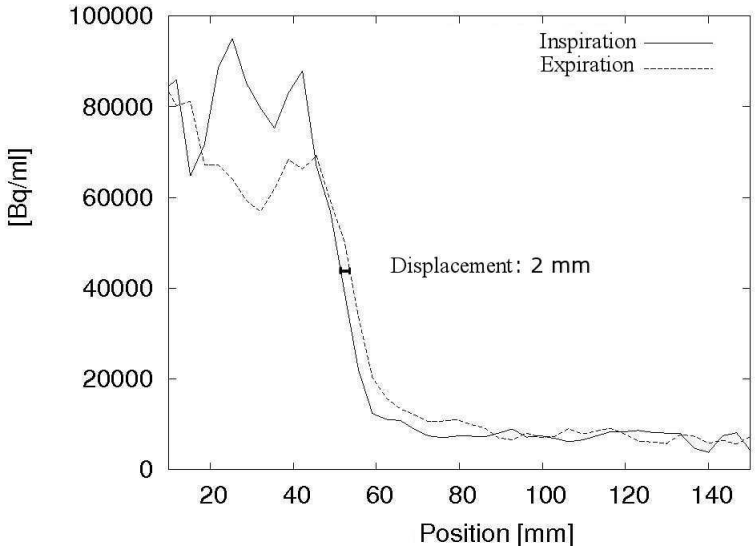

Figure 11.6: Wrong attenuation correction suppresses motion of the PET data. Profiles show the displacement on PET data to be only 2 mm.

The transformation of the static CT in respiratory phases is shown in figure 11.7. Using the line profiles method shows that the motion of the PET data has been transfered to

the CT data as well, see figure 11.8.

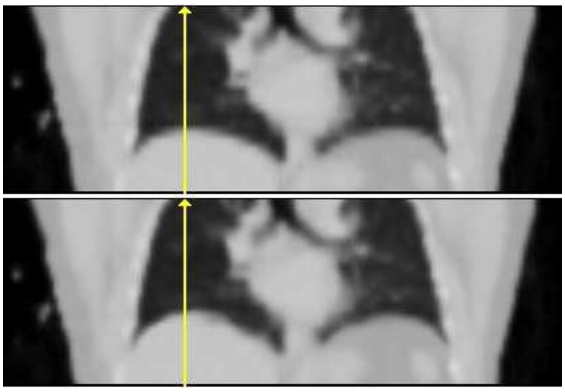

Figure 11.7: A coronal slice from the original CT based *mu*-map (above) and one transformed respiratory phase.

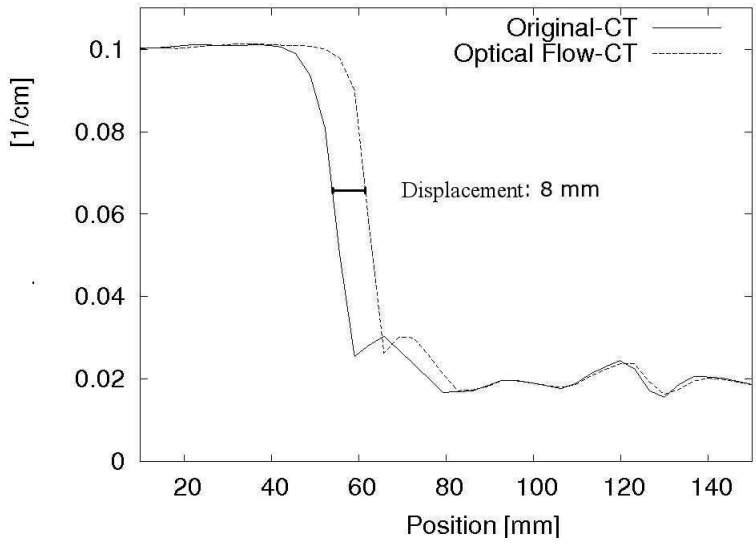

Figure 11.8: Intensity profiles along the marked line shown in figure 11.7. The motion of lungs has been effectively imitated and was found to be 8 mm.

The effect of the transformations after attenuation correction is seen in figure 11.9 where the PET data from phases 1 and 4 is attenuated with the correctly transformed CT data. The change in the hight of the liver is readily visible as compared to the apparently little change seen in figure 11.5. The measurement of displacement with the line profiles method gives the change in position along the marked line to be 8 mm.

The respiration results in upward movement of the lungs and liver as can also be seen in Figure 11.8, where the diaphragm moves up about 3 slices. Thus the PET data from phase 4 attenuated with the static CT wrongly suppresses the liver (the bright spot on the image), whereas the attenuation correction of the same data with the reconstructed CT4 enhanced the liver correctly. A slight enhancement of heart is also observable. The heart is also slightly pushed up with the diaphragm. This small motion was correctly

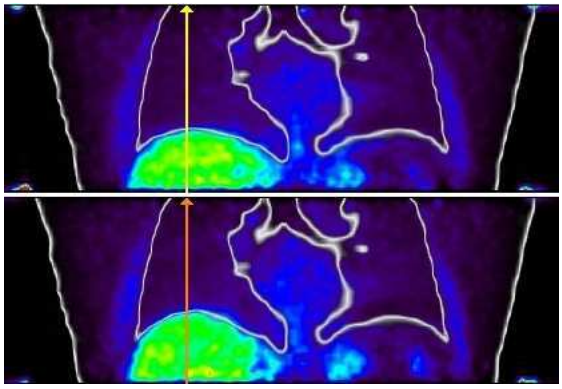

Figure 11.9: PET data after attenuation correction with the transformed CT based *mu*-maps. Top, PET respiratory phase 1 attenuated with CT phase 1. bottom, PET phase 4 attenuated with transformed CT phase 4. (coronal view)

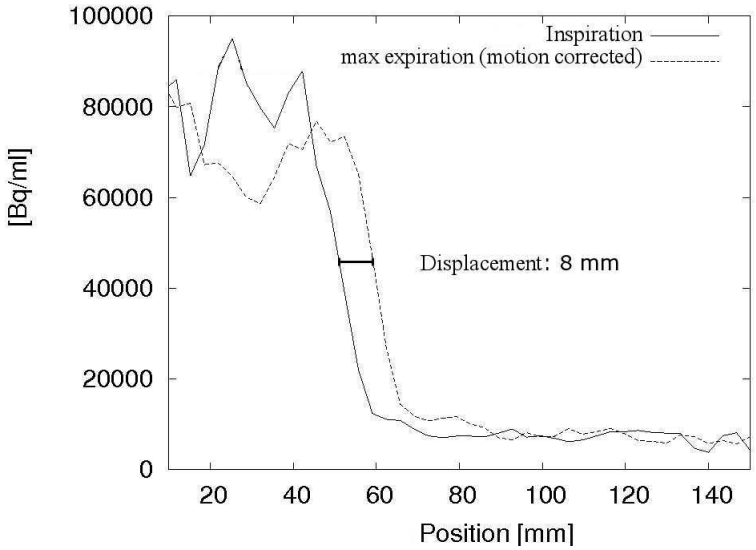

Figure 11.10: Intensity profiles along the marked line shown in figure 11.9. The motion of lungs has been effectively imitated and is found to be 8 mm.

captured by the optical flow method and the static CT deformed accordingly.

11.2 Conclusions

We have presented a novel method of transforming the static single phase CT data acquired during PET/CT scans to different phases of the respiratory cycle. The method was tested on software phantom and real patient data. The method effectively estimates the motion present in the PET data and transforms the static CT to multiple phases accordingly. The method enables better and more precise quantification of the PET/CT data after attenuation correction with the corresponding CT phases and thus enhances the ability to diagnose and plan patient treatment.

Chapter 12

Listmode based Motion and Attenuation Correction

Upto this point in this study, two aspects of the problem of motion in PET/CT data have been presented. Motion correction on PET data, comparison of different algorithms and introduction of discontinuity preservation and multiscale approach were all performed on PET image data. The second aspect, attenuation correction, was also presented based on the optical flow algorithms in the image volumes. However, the PET data can also be acquired from the listmode stream as described earlier in the chapters 1 and 2. This data is more accurate, as it gives the position of the Line-of-Response (LOR) for each detected event directly. The reconstructed image data, in contrast, is the backprojection of these LORs using some analytical or iterative methods. It is thus desirable to perform the motion and the attenuation corrections of the PET data on listmode data to achieve higher accuracy. In this part of the study a complete motion correction scheme is given which combines both the previous parts, motion correction and attenuation correction and uses listmode based reconstruction to give better results. All methods are applied to real patient data sets and are evaluated with respect to three criteria.

12.1 Workflow

The motion and attenuation corrections are applied according to the following scheme. 1) The respiratory gated patient data is acquired on the PET/CT scanner. 2) The individual gates are reconstructed and the motion vectors are calculated with the help of the multi-scale DP optical flow algorithm described previously. 3) The single CT based attenuation-map is transformed to multiple phases so that they correspond to the respiratory phases of the PET data as described in the last chapter. 4) The listmode PET data is reconstructed using the motion vectors and the transformed CT-based attenuation-maps.

12.2 Listmode Motion Correction

The listmode reconstruction was briefly introduced in section 2.2.4. The EM-reconstruction algorithm can also be used on the listmode data without first binning it to sinograms. Thus it is desirable that the motion correction scheme be integrated with the reconstruction scheme for higher precision. A listmode based reconstruction scheme which used rigid

transformations was introduced by Livieratos et al. [61]. Despite better methods the main drawback was the use of rigid motion, which is insufficient for respiratory gated PET data due to the non-rigid nature of respiratory motion. This method was improved by Lamare et al. and the method was extended to affine transformations [55]. The last step, still missing, was again supplied by Lamare et al. to make the listmode reconstruction fully compatible to non-rigid transformations [54].

The basic idea behind this method of reconstruction is to find the intersection of each LOR with the voxels in the reconstructed volume. As the motion of each voxel in the reconstructed volume is known from the application of the optical flow method to the reconstructed image volumes, the LOR is deformed accordingly, see figure 12.1. The same procedure is applied to all events and the deformed LORs are used to reconstruct the images as described by lamare et al. [54]. The attenuation correction is performed by weighting the voxels in accordance with the attenuation values present in the μ-map values given by the deformed CT respiratory phases.

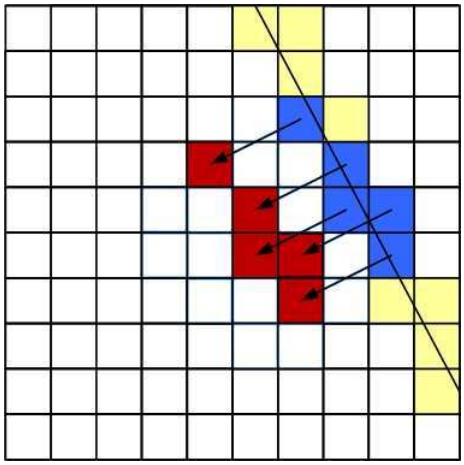

Figure 12.1: In Listmode based motion correction, the voxels for each LOR are corrected according to the motion vectors given by the optical flow algorithm before final image reconstruction.

12.3 Evaluation criteria

Two independent methods were used for evaluating the performance of the motion correction algorithm. These are the heart displacement and the correlation coefficient. The functional parameter used to evaluate the motion correction scheme was the thickness of the myocardium. The first two have been amply explained previously (see chapter 7). Thus only the third one will be introduced below.

12.3.1 Myocardial Thickness

The thickness of the myocardium is an important parameter in assessing our results. The myocardial activity is spread across a band defined by the range of motion of the heart due to respiration. This fact leads to the blurring of the images and to an apparent

thickening of the myocardium. Thicker myocardium thus indicates motion of heart due to respiration. Three consecutive transaxial slices from the center of the heart were manually selected on each patient data. The myocardial thickness was measured on the attenuation corrected PET/CT data by fitting a gaussian function to the anterior wall of the myocardium and the FWHM was calculated. The average thickness of the three slices was then taken to avoid any statistical fluctuations. The myocardial thickness values were measured for three datasets of each patient. These were firstly, the target gate, which contained almost no motion. Secondly, the motion corrected complete dataset and lastly the uncorrected complete dataset. The values of the motion corrected datasets should be similar to the target gate if the motion correction scheme works efficiently. The values for the uncorrected data are expected to be greater than both the previously mentioned datasets.

12.4 Results

The results of the motion correction scheme on the 3D PET data are given in the following subsections in accordance with the criteria described above.

12.4.1 Motion of Heart

The results of the motion of the heart criteria are summarized in table 12.1. The range of motion on the uncorrected data is 21.6 mm to 6.6 mm, whereas the motion corrected data shows a range of 0.5 mm to 0.2 mm. The average results for all patients are given in the last row of the table. Figure 12.2 presents the estimated motion vectors shown on a single coronal-slice taken from the 3D PET volume. The vectors demonstrate that the main motion is present in the heart and the diaphragm region which corresponds with the expectations.

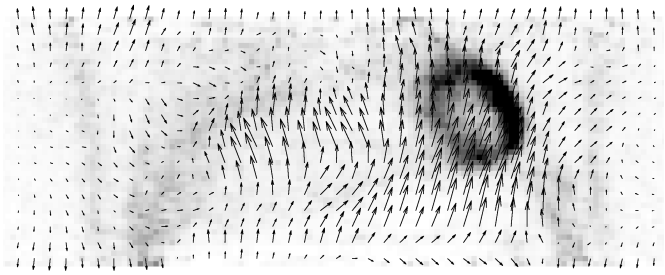

Figure 12.2: Motion estimated on PET data. A coronal-slice from the 3D PET volume is shown overlaid with the estimated motion vectors.

12.4.2 Correlation Coefficient

The correlation coefficient analysis shows the same results as the motion of the heart criteria (table 12.2). The correlation coefficient is shown only for the Gates 1, 4, and 8 to report condensed results. For each of the seven patients the correlation with the target gate, which was Gate 1 for all patients, before motion correction on the original data as well as after motion correction is shown. Gate 1 being the target gate, the correlation for

Table 12.1: Motion of Heart on Patient Data [mm]

Patient	Original	After correction
P1	21.6	0.2
P2	8.4	0.2
P3	12.0	0.5
P4	13.4	0.2
P5	8.9	0.3
P6	6.6	0.2
P7	6.7	0.3
Avg	11.09	0.27

Gate 1 is naturally overall 1.0000. The average of the three values is also given for each patient in the last column.

12.4.3 Myocardial Thickness

The results of the myocardial thickness assessment are given in table 12.3. The thickness of the anterior wall varies from patient to patient, as expected. The range of myocardial thickness without motion correction was between 3.9 mm and 11.0 mm, improving in all cases to values between 4.3 mm and 9.7 mm after motion correction. The averages for all patients are given in the last row of the table.

12.5 Discussion and Conclusions

The aim of this study was to develop a complete motion correction scheme for use in clinical PET/CT applications. The PET data was corrected for motion by using respiratory gating and multi-scale discontinuity-preserving optical flow. Additionally the CT based attenuation map was deformed to correspond to the different respiratory phases, see figure 12.3. This approach is preferable to the approach using gated CT scans because gated CT leads to increased exposure of the patient to x-rays.

12.5.1 Motion of Heart

The results show that the motion correction method has worked with sufficient accuracy on all patients. The performance of the method was independent of the magnitude of motion on the original, uncorrected, images. Thus the motion was reduced to 0.2 mm on patient P1 with 21.6 mm motion as well as on P6 with only 6.6 mm of motion. The highest value on corrected data was 0.5 mm in patient P3 who has 12 mm of displacement. This shows that the motion correction scheme is not dependent upon the magnitude of motion present on the images. As the voxel resolution of the data was 3.375 mm in each direction, we can consider the respiratory motion to have been sufficiently corrected for all practical purposes.

Table 12.2: Correlation Coefficient Analysis on Patient Data

Patient	Gate 1	Gate 4	Gate 8	Average
P1 Original	1.0000	0.7309	0.6130	0.7813
P1 Corrected	1.0000	0.9413	0.9378	0.9597
P2 Original	1.0000	0.8865	0.8000	0.8955
P2 Corrected	1.0000	0.9512	0.9495	0.9669
P3 Original	1.0000	0.8451	0.8034	0.8828
P3 Corrected	1.0000	0.9281	0.9118	0.9466
P4 Original	1.0000	0.8153	0.6975	0.8376
P4 Corrected	1.0000	0.9743	0.9698	0.9814
P5 Original	1.0000	0.8856	0.8127	0.8994
P5 Corrected	1.0000	0.9514	0.9508	0.9674
P6 Original	1.0000	0.9426	0.8893	0.9440
P6 Corrected	1.0000	0.9838	0.9829	0.9889
P7 Original	1.0000	0.8869	0.8482	0.9117
P7 Corrected	1.0000	0.9485	0.9417	0.9634

12.5.2 Correlation Coefficient

The result of the correlation coefficient analysis support the results of the displacement of the heart analysis. The correlation is increased to values closer to 1 as compared to before motion correction for all patients and all gates. The large number of voxels which remain unmoved, e.g. outside the body etc., lead to a high correlation even in the uncorrected data e.g. over 0.88 in patient P5. The correlation of different gates with the target gate is almost constant even though the motion has increased significantly from the first to the eighth gate. Thus the correlation fell from 0.7309 in gate 4 for patient P1 to 0.6130 in gate 8, a difference of 0.1179. The decrease on the corrected data for the same patient is 0.9413 to 0.9378 which is a difference of only 0.0035. This uniformity in results shows that the correction method works relatively independent of the magnitude of the motion present on the data. The same result as given by the heart motion analysis.

It should be noted that the increase in correlation is not due to any interpolation effects as proved earlier in chapter 7. It is rather due to motion correction on the data.

12.5.3 Myocardial Thickness

The results of the myocardial thickness analysis strengthen the results of the previous sections further. It was expected that the anterior wall will appear thicker if respiratory motion is present on the images because the radioactivity will be spread over the area of motion. This fact can been seen by comparing the thickness measured in the target gate

Table 12.3: Myocardial Thickness Analysis on Patient Data [mm]

Patient	Target Gate	Motion Corrected	Not Corrected
P1	7.9	8.3	11.0
P2	7.6	7.2	9.5
P3	3.9	4.3	4.7
P4	6.3	6.5	7.3
P5	10.2	9.7	11.0
P6	5.0	5.2	5.3
P7	4.7	4.5	4.8
Avg	6.5	6.5	7.7

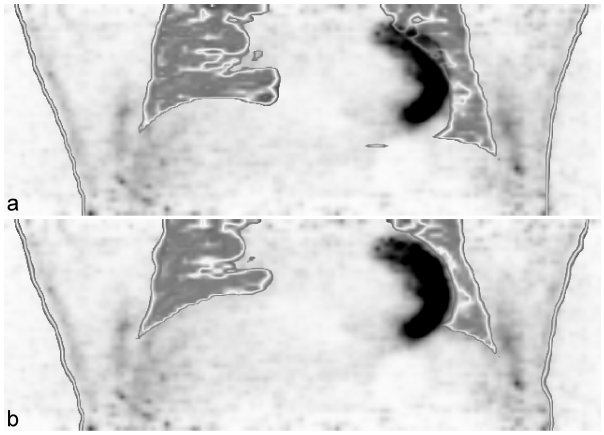

Figure 12.3: Transformation of the CT based μ-maps for accurate attenuation correction. The CT based μ-maps are shown overlaid on the PET data. Image a) shows that the μ-map does not corresponds to the respiratory phase of the PET data in the heart region. Image b) shows that after correction, the μ-map corresponds with the PET data and thus allows more accurate attenuation correction.

to the thickness measured on the not corrected data (columns 1 and 3 of the table 12.3. The results of the motion corrected data are comparable to the target gate. It is to be noted that in P1, the patient with the largest motion, the difference in the myocardial thickness between the corrected and the uncorrected data is around 3 mm, or almost 1 voxel.

12.5.4 Conclusion

A complete motion correction scheme was presented. This scheme included motion correction of the PET data, the transformation of the CT based μ-maps and the reconstruction of the listmode data using these corrections. The results of the scheme were evaluated on seven real patient datasets. Three criteria were used to assess the quality of the motion correction. All three criteria showed that motion was successfully corrected.

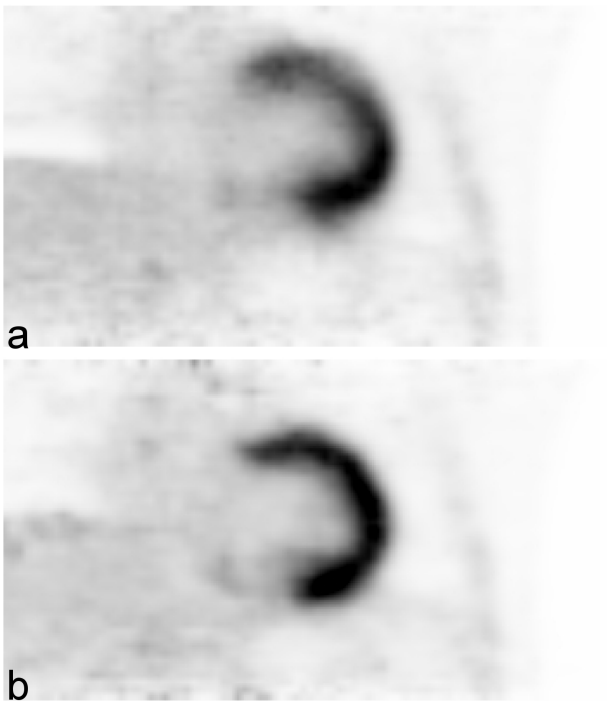

Figure 12.4: The image a) shows the ungated PET/CT images after attenuation correction. The image b) shows the same data after attenuation and motion correction. The blur and the apparently decreased tracer uptake of the anterior wall on image a) is corrected to a great extent in image b).

Part IV

Conclusions

Chapter 13

Conclusions and Outlook

The first part of the proposed solution dealt with the problem of correctly gating the PET data with respect to a respiratory signal. An optical camera based method of capturing respiratory signal was developed and the corresponding signal analysis software was implemented. A quantitative comparison of seven methods of respiratory gating of PET data with respect to their ability to capture the motion in patients was presented. The study proves that amplitude-based methods are superior to time-based methods. If enough number of gates are selected, the variable amplitudes based method is a good choice as it ensures similarity of noise properties on the reconstructed images in addition to capturing the motion accurately. This last aspect is important for application of optical flow methods to the PET data.

In the second part, different optical flow algorithms were extended to 3D+t (also called 4D) and applied to the specific problem of respiratory motion correction on PET data. The non-linear variant of the Bruhn-Simple algorithm was improved to preserve the discontinuities across organ boundaries on the images. The algorithms were applied to the software phantom data and real patient data and evaluated with respect to the motion of the left heart ventricle and the correlation coefficient. It was found, that the advanced optical flow methods give better results as compared to the Lukas-Kanade or Horn-Schunck algorithms.

The discontinuity preserving optical flow algorithm proposed for motion correction of PET images gave good results. However, residual motion continued to be a problem in some patients with very large respiratory motion. The DP-algorithm was therefore extended to a multi-resolution process to overcome this difficulty. The results on real patient data showed a significantly improved performance as compared with the previous, not multi-resolution compatible, version. The residual motion on the PET images was reduced to under 0.5 mm. This figure, when compared to the voxel resolution of 3.375 mm, shows that the motion has been effectively corrected on the PET data for all practical purposes.

In PET/CT Data the CT is also used to correct the PET data for the effects of attenuation inside the body. As using additional CTs was not an option, because it increases the X-ray dose for the patient, the motion information extracted from the PET images was used to deform the CT based μ-maps. The effectiveness of this approach was demonstrated on software phantom and on real patient data.

Lastly, all steps of the respiratory motion correction scheme were incorporated into a reconstruction method which weighted each LOR in accordance with the transformed

μ-maps and corrected it spatially with the help of the motion vectors extracted from the PET data. The results of the study show that motion artifacts and image blur have been removed successfully.

13.1 Outlook

Future work to improve the methods presented in this study can be conceived of in three aspects. Firstly a study on the selection of the number of gates for respiratory motion is needed to optimize the gating scheme. The number of gates selected in this study (eight) was derived from theoretical assessment as described in [25]. Increasing the number of gates improves the sharpness of the images but also decreases the contrast due to the presence of larger amount of noise. Finding a compromise between the two conditions is itself an optimization task.

Secondly the performance of the optical flow methods can be improved by using multi-grid systems for large displacements. It is helpful to not always reduce the resolution by exactly a factor of two. Implementing factors between 1 and 2 will make the optical flow estimation more accurate in presence of large displacements, as it will allow usage of more levels for motion estimation.

Thirdly, the optical flow algorithms can be extended to a complete 4D approach. Using such a scheme will allow more consistency in the results. At present each 3D image volume is motion corrected individually without using the motion information acquired in other gates. In cyclic systems, such as cardiac or respiratory motion, the displacements in one gate should not be very much different than the displacements in the adjacent gates. This fact can be exploited in a complete 4D optical flow scheme easily.

The optimization of all three aspects, it is hoped, will lead to more accurate and consistent results.

List of Tables

List of Figures

Index

Bibliography

[1] Url: stir.sourceforge.net.

[2] L Alvarez, J Weickert, and J Sanchez. Relaiable estimation of dense optical flow fields with large displacements. *IJCV*, 39(1):41–56, 2000.

[3] N Ancona and T Poggio. Optical flow from 1d correlation: Application to a simple time-to-crash detector. In *Proceedings of the 4th International Conference on Computer Vision*, pages 209–214, 1993.

[4] JL Andersson, BE Vagnhammar, and H Schneider. Accurate attenuation correction despite movement during PET imaging. *J Nucl Med*, 36(4):670–678, Apr 1995.

[5] A Bab-Hadiashar and D Suter. Robust total least squares based optic flow computation. In *ACCV*, volume 1, 1998.

[6] JL Barron, DJ Fleet, and SS Beauchemin. Performance of optical flow techniques. *International Journal of Computer Vision*, 12:43–77, 1994.

[7] F Bartolini, V Capellini, C Colombo, and A Mecocci. A multiwindow least squares approach to the estimation of optical flow with discontinuities. *Optical Engineering, Special Section on From Numerical to Symbolic Image Processing: Systems and Applications*, 32(6):1250–1256, 1993.

[8] AS Beddar, K Kainz, TM Briere, Y Tsunashima, T Pan, K Prado, R Mohan, M Gillin, and S Krishnan. Correlation between internal fiducial tumor motion and external marker motion for liver tumors imaged with 4D-CT. *Int J Radiat Oncol Biol Phys*, 67(2):630–638, Feb 2007.

[9] V Behar, D Adam, P Lysyansky, and Z Friedman. Improving motion estimation by accounting for local image distortion. *Ultrasonics*, 43(1):57–65, Oct 2004.

[10] L Boucher, S Rodrigue, R Lecomte, and F Bnard. Respiratory gating for 3-dimensional PET of the thorax: feasibility and initial results. *J Nucl Med*, 45(2):214–219, Feb 2004.

[11] ED Brandner, A Wu, H Chen, D Heron, S Kalnicki, K Komanduri, K Gerszten, S Burton, I Ahmed, and Z Shou. Abdominal organ motion measured using 4D CT. *Int J Radiat Oncol Biol Phys*, 65(2):554–560, Jun 2006.

[12] D Brasse, PE Kinahan, C Lartizien, C Claude, M Casey, and C Michel. Correction methods for random coincidences in fully 3D whole-body PET: impact on data and image quality. *J Nucl Med*, 46(5):859–867, May 2005.

[13] LG Brown. A survey of image registration techniques. *ACM Computing Surveys*, 24:325–376, 1992.

[14] A Bruhn, J Weickert, C, and Schnörr. Lucas/Kanade meets Horn/Schunch: Combining local and global optic flow methods. *International Journal of Computer Vision*, 61(3):211–231, 2005.

[15] A Bruhn, J Weickert, and C Schnörr. Combining the advantages of local and global optic flow methods. In Luc van Gool, editor, *Proceedings of the 24th DAGM Symposium on Pattern Recognition*, volume 2449 of *Lecture Notes on Computer Science*, pages 454–462, Heidelberg, 2002. Springer.

[16] P Bühler, U Just, E Will, J Kotzerke, and J van den Hoff. An accurate method for correction of head movement in PET. *IEEE Trans Med Imaging*, 23(9):1176–1185, Sep 2004.

[17] PJ Burt and EH Adelson. The laplacian pyramid as a compact image code. *IEEE Transactions on Communications*, COM-31(4):532–540, April 1983.

[18] F Büther, L Stegger, M Dawood, F Range, M Schfers, R Fischbach, T Wichter, O Schober, and KP Schfers. Effective methods to correct contrast agent-induced errors in PET quantification in cardiac PET/CT. *J Nucl Med*, 48(7):1060–1068, Jul 2007.

[19] JB Carlin and LW Doyle. Statistics for clinicians: 4: Basic concepts of statistical reasoning: hypothesis tests and the t-test. *J Paediatr Child Health*, 37(1):72–77, Feb 2001.

[20] P Charbonnier, L Blanc-Feraud, G Aubert, and M Barlaud. Two deterministic half-quadratic regularization algorithms for computed imaging. In *Image Processing, 1994. Proceedings. ICIP-94., IEEE International Conference*, volume 2, pages 168–172, November 1994.

[21] C Cohade, M Osman, LNT Marshall, and RNTL Wahl. PET-CT: accuracy of PET and CT spatial registration of lung lesions. *Eur J Nucl Med Mol Imaging*, 30(5):721–726, May 2003.

[22] T Corpetti, E Memin, and P Perez. Estimating fluid optical flow. In *Proceedings of the 15th International Conference on Pattern recognition*, volume 3, page 7045ff, 2000.

[23] WR Crum, T Hartkens, and DLG Hill. Non-rigid image registration: theory and practice. *Br J Radiol*, 77 Spec No 2:S140–S153, 2004.

[24] CQ Davis and DM Freeman. Equivalence of subpixel motion estimators based on optical flow and block matching. In *ISCV '95: Proceedings of the International Symposium on Computer Vision*, page 7ff, 1995.

[25] M Dawood, F Büther, N Lang, O Schober, and KP Schäfers. Respiratory gating in positron emission tomography: A quantitative comparision of different gating schemes. *Medical Physics*, 34(7):3067–3076, July 2007.

[26] M Dawood, N Lang, X Jiang, and KP Schäfers. Lung motion correction on respiratory gated 3-D PET/CT images. *IEEE Trans Med Imaging*, 25(4):476–485, Apr 2006.

[27] ER Denton, LI Sonoda, D Rueckert, SC Rankin, C Hayes, MO Leach, DL Hill, and DJ Hawkes. Comparison and evaluation of rigid, affine, and nonrigid registration of breast MR images. *J Comput Assist Tomogr*, 23(5):800–805, 1999.

[28] R Deriche, P Kornprobst, and G Aubert. Optical-flow estimation while preserving its discontinuities: A variational approach. In *Proceedings of the 2nd Asian Conference on Computer Vision*, volume 2, pages 71–80, Singapore, 1995.

[29] L Dietrich, S Jetter, T Tücking, S Nill, and U Oelfke. Linac-integrated 4D cone beam CT: first experimental results. *Phys Med Biol*, 51(11):2939–2952, Jun 2006.

[30] L Dougherty, JC Asmuth, AS Blom, L Axel, and R Kumar. Validation of an optical flow method for tag displacement estimation. *IEEE Trans Med Imaging*, 18(4):359–363, Apr 1999.

[31] Q Duan, E Angelini, S Homma, and A Laine. Tracking endocardium using optical flow along iso-value curve. *Conf Proc IEEE Eng Med Biol Soc*, 1:707–710, 2006.

[32] Q Duan, ED Angelini, SL Herz, O Gerard, P Allain, CM Ingrassia, KD Costa, JW Holmes, S Homma, and AF Laine. Tracking of LV endocardial surface on real-time three-dimensional ultrasound with optical flow. In AF Farangi et al, editor, *FIMH 2005*, volume 3504 of *LNCS*, pages 434–445, Berlin, 2005. Springer.

[33] R El-Feghali and A Mitiche. Fast computation of a boundary preserving estimate of optical flow. In *Proceedings of the British Machine Vision Conference*, Bristol, UK, 2000.

[34] YE Erdi, SA Nehmeh, T Mulnix, JL Humm, and CC Watson. PET performance measurements for an LSO-based combined PET/CT scanner using the national electrical manufacturers association NU 2-2001 standard. *J Nucl Med*, 45(5):813–821, May 2004.

[35] YE Erdi, SA Nehmeh, T Pan, A Pevsner, KE Rosenzweig, G Mageras, ED Yorke, H Schoder, W Hsiao, OD Squire, P Vernon, JB Ashman, H Mostafavi, SM Larson, and JL Humm. The CT motion quantitation of lung lesions and its impact on PET-measured SUVs. *J Nucl Med*, 45(8):1287–1292, Aug 2004.

[36] J Fitzgerald and PG Danias. Effect of motion on cardiac SPECT imaging: recognition and motion correction. *J Nucl Cardiol*, 8(6):701–706, 2001.

[37] DJ Fleet and AD Jepson. Computation of component image velocity from local phase information. *IJCV*, 5(1):77–104, 1990.

[38] H Foroosh. Pixelwise-adaptive blind optical flow assuming nonstationary statistics. *IEEE Trans Img Processing*, 14(2):222–230, February 2005.

[39] RR Fulton, SR Meikle, S Eberl, J Pfeiffer, CJ Constable, and MJ Fulham. Correction for head movements in positron emission tomography using an optical motion-tracking system. *IEEE Transactions on Nuclear Science*, 49:116–123, 2002.

[40] S Galic and S Loncaric. Spatio-temporal image segmentation using optical flow and clustering. In *Proceedings of the First International Workshop on Image and Signal Processing 2000*, pages 63–68, 2000.

[41] B Galvin, B McCane, K Novins, D Mason, and S Mills. Recovering motion fields: an evaluation of eight optical flow algorithms. In *Proceedings of the Ninth British Machine Vision Conference*, volume 1, pages 195–204, 1998.

[42] P Giraud, E Yorke, EC Ford, R Wagman, GS Mageras, H Amols, CC Ling, and KE Rosenzweig. Reduction of organ motion in lung tumors with respiratory gating. *Lung Cancer*, 51(1):41–51, Jan 2006.

[43] JM Gorce, D Friboulet, and IE Magnin. Estimation of three-dimensional cardiac velocity fields: assessment of a differential method and application to three-dimensional CT data. *Med Image Anal*, 1(3):245–261, Apr 1997.

[44] JF Hair, RE Anderson, RL Tatham, and WC Black. *Multivariate Data Analysis*. Prentice-Hall International, fifth edition edition, 1998.

[45] N Hata, A Nabavi, WM Wells, SK Warfield, R Kikinis, PM Black, and FA Jolesz. Three-dimensional optical flow method for measurement of volumetric brain deformation from intraoperative MR images. *J Comput Assist Tomogr*, 24(4):531–538, 2000.

[46] J He and GE Christensen. Large deformation inverse consistant elastic image registration. In C Taylor and JA Noble, editors, *Information Processing in Medical Imaging*, volume 2732 of *Lecture Notes on Computer Science*, pages 438–449, Heidelberg, 2003. Springer.

[47] M Holden. A review of geometric transformations for nonrigid body registration. *IEEE Trans Med Imaging*, 27(1):111–128, January 2008.

[48] B Horn and B Schunck. Determining optical flow. *Artificial Intelligence*, 17:185–203, 1981.

[49] PE Kinahan, DW Townsend, T Beyer, and D Sashin. Attenuation correction for a combined 3D PET/CT scanner. *Med Phys*, 25(10):2046–2053, Oct 1998.

[50] GJ Klein. *Deformable Models for Volume Feature Tracking.* PhD thesis, The University of California, Berkley, 1999.

[51] GJ Klein, BW Reutter, MH Ho, JH Reed, and RH Huesman. Real-time system for respiratory-cardiac gating in positron tomography. *IEEE Transactions on Nuclear Science*, 45:2139–2143, 1997.

[52] J Knuuti and P Nuutila. Pet as a cardiovascular and metabolic research tool. *Ann Med*, 31(6):450–456, Dec 1999.

[53] N Koch, HH Liu, G Starkschall, M Jacobson, K Forster, Z Liao, R Komaki, and CW Stevens. Evaluation of internal lung motion for respiratory-gated radiotherapy using MRI: Part i–correlating internal lung motion with skin fiducial motion. *Int J Radiat Oncol Biol Phys*, 60(5):1459–1472, Dec 2004.

[54] F Lamare, MJL Carbayo, T Cresson, G Kontaxakis, A Santos, CC Le Rest, AJ Reader, and D Visvikis. List-mode-based reconstruction for respiratory motion correction in PET using non-rigid body transformations. *Phys Med Biol*, 52(17):5187–5204, Sep 2007.

[55] F. Lamare, T. Cresson, J. Savean, C. Cheze Le Rest, A. J. Reader, and D. Visvikis. Respiratory motion correction for pet oncology applications using affine transformation of list mode data. *Phys Med Biol*, 52(1):121–140, Jan 2007.

[56] J Lee, C Park, and I Lee. An arbitrary pointtracking using multi-scale refined optical flow. In *Proceedings of the 9th International Conference on Advanced Communication Technology*, pages 373–377, 2007.

[57] TM Lehmann, C Gönner, and K Spitzer. Survey: interpolation methods in medical image processing. *IEEE Trans Med Imaging*, 18(11):1049–1075, Nov 1999.

[58] TM Lehmann, C Gonner, and K Spitzer. Addendum: B-spline interpolation in medical image processing. *Medical Imaging, IEEE Transactions on*, 20(7):660–665, July 2001.

[59] CS Levin and EJ Hoffman. Calculation of positron range and its effect on the fundamental limit of positron emission tomography system spatial resolution. *Phys Med Biol*, 44(3):781–799, Mar 1999.

[60] XA Li, C Stepaniak, and E Gore. Technical and dosimetric aspects of respiratory gating using a pressure-sensor motion monitoring system. *Med Phys*, 33(1):145–154, Jan 2006.

[61] L. Livieratos, L. Stegger, P. M. Bloomfield, K. Schafers, D. L. Bailey, and P. G. Camici. Rigid-body transformation of list-mode projection data for respiratory motion correction in cardiac pet. *Phys Med Biol*, 50(14):3313–3322, Jul 2005.

[62] W Lu and TR Mackie. Tomographic motion detection and correction directly in sinogram space. *Phys Med Biol*, 47(8):1267–1284, Apr 2002.

[63] BD Lucas and T Kanade. An iterative image registration technique with an application to stereo vision. *Proceedings of Imaging understanding workshop*, pages 121–130, 1981.

[64] E Maeland. On the comparison of interpolation methods. *Medical Imaging, IEEE Transactions on*, 7(3):213–217, Sept. 1988.

[65] F Maes, A Collignon, D Vandermeulen, G Marchal, and P Suetens. Multimodality image registration by maximization of mutual information. *IEEE Trans Med Imaging*, 16(2):187–198, Apr 1997.

[66] JB Maintz and MA Viergever. A survey of medical image registration. *Med Image Anal*, 2(1):1–36, Mar 1998.

[67] BA Mair, DR Gilland, and J Sun. Estimation of images and nonrigid deformations in gated emission CT. *IEEE Trans Med Imaging*, 25(9):1130–1144, Sep 2006.

[68] R Manjeshwar, X Tao, E Asma, and K Thielemans. Motion compensated image reconstruction of respiratory gated PET/CT. In *IEEE International Symposium on Biomedical Imaging: From Nano to Macro*, pages 674–677, 2006.

[69] MJ Martinez, Y Bercier, M Schwaiger, and SI Ziegler. PET/CT biograph sensation 16. performance improvement using faster electronics. *Nuklearmedizin*, 45(3):126–133, 2006.

[70] B McCane, K Novins, D Crannitch, and B Galvin. On benchmarking optical flow. *Computer Vision and Image Understanding*, 84:126–143, 2001.

[71] CK McKibben and NV Reo. A piezoelectric respiratory monitor for in vivo NMR. *Magn Reson Med*, 27(2):338–342, Oct 1992.

[72] K McLeish, DLG Hill, D Atkinson, JM Blackall, and R Razavi. A study of the motion and deformation of the heart due to respiration. *IEEE Trans Med Imaging*, 21(9):1142–1150, Sep 2002.

[73] Y Nakamoto, BB Chin, C Cohade, M Osman, M Tatsumi, and RL Wahl. PET/CT: artifacts caused by bowel motion. *Nucl Med Commun*, 25(3):221–225, Mar 2004.

[74] F Natterer. Numerical methods in tomography. *Acta Numerica*, 8:107–142, 1999.

[75] F Natterer. Inversion of the attenuated radon transform. *Inverse Problems*, 17:113–119, 2001.

[76] F Natterer and F Wübbeling. *Mathematical Methods in Image Reconstruction*. SIAM, Philadelphia, 2001.

[77] S. A. Nehmeh, Y. E. Erdi, T. Pan, E. Yorke, G. S. Mageras, K. E. Rosenzweig, H. Schoder, H. Mostafavi, O. Squire, A. Pevsner, S. M. Larson, and J. L. Humm. Quantitation of respiratory motion during 4D-PET/CT acquisition. *Med Phys*, 31(6):1333–1338, Jun 2004.

[78] SA Nehmeh, YE Erdi, CC Ling, KE Rosenzweig, H Schoder, SM Larson, HA Macapinlac, OD Squire, and JL Humm. Effect of respiratory gating on quantifying PET images of lung cancer. *J Nucl Med*, 43(7):876–881, Jul 2002.

[79] Sadek A Nehmeh, Yusuf E Erdi, Kenneth E Rosenzweig, Heiko Schoder, Steve M Larson, Olivia D Squire, and John L Humm. Reduction of respiratory motion artifacts in PET imaging of lung cancer by respiratory correlated dynamic PET: methodology and comparison with respiratory gated PET. *J Nucl Med*, 44(10):1644–1648, Oct 2003.

[80] MM Osman, C Cohade, Y Nakamoto, LT Marshall, JP Leal, and RL Wahl. Clinically significant inaccurate localization of lesions with PET/CT: frequency in 300 patients. *J Nucl Med*, 44(2):240–243, Feb 2003.

[81] MM Osman, C Cohade, Y Nakamoto, and RL Wahl. Respiratory motion artifacts on pet emission images obtained using ct attenuation correction on pet-ct. *Eur J Nucl Med Mol Imaging*, 30(4):603–606, Apr 2003.

[82] N Otsu. A threshold selection method from gray-level histograms. *IEEE Transactions on Systems, Man, and Cybernetics*, 9:62–66, 1979.

[83] T Pan, O Mawlawi, D Luo, HH Liu, PM Chi, MV Mar, G Gladish, M Truong, J Erasmus, Z Liao, and HA Macapinlac. Attenuation correction of PET cardiac data with low-dose average CT in PET/CT. *Med Phys*, 33(10):3931–3938, Oct 2006.

[84] T Pan, O Mawlawi, SA Nehmeh, YE Erdi, D Luo, HH Liu, R Castillo, R Mohan, Z Liao, and HA Macapinlac. Attenuation correction of PET images with respiration-averaged CT images in PET/CT. *J Nucl Med*, 46(9):1481–1487, Sep 2005.

[85] D Papathanassiou, S Becker, R Amir, B Menroux, and JC Liehn. Respiratory motion artefact in the liver dome on FDG PET/CT: comparison of attenuation correction with CT and a caesium external source. *Eur J Nucl Med Mol Imaging*, 32(12):1422–1428, Dec 2005.

[86] GP Penney, JA Schnabel, D Rueckert, MA Viergever, and WJ Niessen. Registration-based interpolation. *Medical Imaging, IEEE Transactions on*, 23(7):922–926, July 2004.

[87] ME Phelps, editor. *PET, Molecular Imaging and its Biological Applications*. Springer, 2004.

[88] Y Picard and CJ Thompson. Motion correction of PET images using multiple acquisition frames. *IEEE Trans Med Imaging*, 16(2):137–144, Apr 1997.

[89] JP Pluim, JB Maintz, and MA Viergever. Image registration by maximization of combined mutual information and gradient information. *IEEE Trans Med Imaging*, 19(8):809–814, Aug 2000.

[90] PH Pretorius, MA King, BM Tsui, KJ LaCroix, and W Xia. A mathematical model of motion of the heart for use in generating source and attenuation maps for simulating emission imaging. *Med Phys*, 26(11):2323–2332, Nov 1999.

[91] JL Prince, SN Gupta, and NF Osman. Bandpass optical flow for tagged MRI. *Med Phys*, 27(1):108–118, Jan 2000.

[92] F Qiao, T Pan, JW Clark, and OR Mawlawi. A motion-incorporated reconstruction method for gated PET studies. *Phys Med Biol*, 51(15):3769–3783, Aug 2006.

[93] M Qiu. Computing optical flow based on the mass-conserving assumption. In *Proceedings of the 15th International conference on Pattern Recognition*, volume 3, pages 1029–1032, 2000.

[94] A Rahmim, M Lenox, AJ Reader, C Michel, Z Burbar, TJ Ruth, and V Sossi. Statistical list-mode image reconstruction for the high resolution research tomograph. *Phys Med Biol*, 49(18):4239–4258, Sep 2004.

[95] TR Reed. the computation of optical flow using the 3-D gabor transform. *Multidimensional Systems and Signal Processing*, 9:447–452, 1998.

[96] EM Rohren, TG Turkington, and RE Coleman. Clinical applications of PET in oncology. *Radiology*, 231(2):305–332, May 2004.

[97] J Ruhlmann, P Oehr, and HJ Biersack, editors. *PET in der Onkologie*. Springer, Heidelberg, 1998.

[98] MP Sandler, RE Coleman, JA Patton, F Wackers, and A Gottschalk, editors. *Diagnostic Nuclear Medicine*. Lippincott Williams & Wilkins, 2003.

[99] D Sarrut and S Miguet. Similarity measures for image registration. In *First European Workshop on Content-Based Multimedia Indexing*, pages 263–270, Toulouse, France, 1999.

[100] AJ Schwarz and MO Leach. Implications of respiratory motion for the quantification of 2D MR spectroscopic imaging data in the abdomen. *Phys Med Biol*, 45(8):2105–2116, Aug 2000.

[101] WP Segars. *Development of a new dynamic nurbs-based cardiac-torso (ncat) phantom.* PhD thesis, The University of North Carolina, 2001.

[102] Yvette Seppenwoolde, Hiroki Shirato, Kei Kitamura, Shinichi Shimizu, Marcel van Herk, Joos V Lebesque, and Kazuo Miyasaka. Precise and real-time measurement of 3d tumor motion in lung due to breathing and heartbeat, measured during radiotherapy. *Int J Radiat Oncol Biol Phys*, 53(4):822–834, Jul 2002.

[103] G Shechter, B Shechter, JR Resar, and R Beyar. Prospective motion correction of X-ray images for coronary interventions. *IEEE Trans Med Imaging*, 24(4):441–450, Apr 2005.

[104] S Shen, J Duan, JB Fiveash, IA Brezovich, BA Plant, SA Spencer, RA Popple, PN Pareek, and JA Bonner. Validation of target volume and position in respiratory gated CT planning and treatment. *Med Phys*, 30(12):3196–3205, Dec 2003.

[105] SM Song and RM Leahy. Computation of 3-D velocity fields from 3-D cine CT images of a human heart. *IEEE Trans Med Imaging*, 10:295–306, 1991.

[106] JA Sorensen and ME Phelps. *Physics in nuclear medicine*. Grune & Stratton Inc, 1987.

[107] G Tarantola, F Zito, and P Gerundini. PET instrumentation and reconstruction algorithms in whole-body applications. *J Nucl Med*, 44(5):756–769, May 2003.

[108] MM Ter-Pogossian, SR Bergmann, and BE Sobel. Influence of cardiac and respiratory motion on tomographic reconstructions of the heart: implications for quantitative nuclear cardiology. *J Comput Assist Tomogr*, 6(6):1148–1155, Dec 1982.

[109] P Thevenaz, T Blu, and M Unser. Interpolation revisited. *IEEE Trans Med Imaging*, 19(7):739–758, Jul 2000.

[110] M Thomas, C Kambhamettu, CA Geiger, J Hutchings, J Richter-Menge, and M Engram. Near-real time application of SAR-derived sea ice differential motion during APLIS ice camp 2007. In *Proceedings of the 2007 Annual Conference of the Remote Sensing & Photogrammetry Society*, 2007.

[111] DA Torigian, WB Gefter, JD Affuso, K Emami, and L Dougherty. Application of an optical flow method to inspiratory and expiratory lung mdct to assess regional air trapping: a feasibility study. *AJR Am J Roentgenol*, 188(3):W276–W280, Mar 2007.

[112] BMW Tsui, WP Segars, and DS Lalush. Effects of upward creep and respiratory motion in myocardial SPECT. *IEEE Transactions on Nuclear Science*, 47:1192–1195, 2000.

[113] S Vandenberghe, Y D'Asseler, R Van de Walle, T Kauppinen, M Koole, L Bouwens, K Van Laere, I Lemahieu, and RA Dierckx. Iterative reconstruction algorithms in nuclear medicine. *Comput Med Imaging Graph*, 25(2):105–111, 2001.

[114] SS Vedam, VR Kini, PJ Keall, V Ramakrishnan, H Mostafavi, and R Mohan. Quantifying the predictability of diaphragm motion during respiration with a noninvasive external marker. *Med Phys*, 30(4):505–513, Apr 2003.

[115] BC Vemuri, S Huang, S Sahni, CM Leonard, C Mohr, R Gilmore, and J Fitzsimmons. An efficient motion estimator with application to medical image registration. *Med Image Anal*, 2(1):79–98, Mar 1998.

[116] GD Vitale, RA deKemp, TD Ruddy, K Williams, and RS Beanlands. Myocardial glucose utilization and optimization of (18)F-FDG PET imaging in patients with non-insulin-dependent diabetes mellitus, coronary artery disease, and left ventricular dysfunction. *J Nucl Med*, 42(12):1730–1736, Dec 2001.

[117] MP Wachowiak, R Smolikova, Y Zheng, JM Zurada, and AS Elmaghraby. An approach to multimodal biomedical image registration utelizing particle swarm optimization. *IEEE Trans on EC*, 8(3):289–301, 2004.

[118] N Wink, C Panknin, and TD Solberg. Phase versus amplitude sorting of 4D-CT data. *J Appl Clin Med Phys*, 7(1):77–85, 2006.

[119] K Wurstbauer, H Deutschmann, P Kopp, and F Sedlmayer. Radiotherapy planning for lung cancer: slow CTs allow the drawing of tighter margins. *Radiother Oncol*, 75(2):165–170, May 2005.

[120] Y Ye and G Wang. Filtered backprojection formula for exact image reconstruction from cone-beam data along a general scanning curve. *Medical Physics*, 32:42–48, 2005.

[121] H Zaidi. Scatter modelling and correction strategies in fully 3-D PET. *Nucl Med Commun*, 22(11):1181–1184, Nov 2001.

[122] H Zaidi and KF Koral. Scatter modelling and compensation in emission tomography. *Eur J Nucl Med Mol Imaging*, 31(5):761–782, May 2004.

[123] D Zhang and G Lu. An edge and color oriented optical flow estimation using blockmatching. In *Signal Processing Proceedings*, volume 2, pages 1026–1032, 2000.

[124] Y Zhang, DB Goldgof, and S Sarkar. Towards physically-sound registration using object-specific properties for regularization. In JBA Maintz JC Gee and MW Vannier, editors, *Biomedical Image Registration*, volume 2717 of *Lecture Notes on Computer Science*, pages 358–366, Heidelberg, 2003. Springer.

[125] GP Zientara, P Saiviroonporn, PR Morrison, MP Fried, SG Hushek, R Kikinis, and FA Jolesz. MRI monitoring of laser ablation using optical flow. *J Magn Reson Imaging*, 8(6):1306–1318, 1998.

[126] B Zitova and J Flusser. Image registration methods: A survey. *Image and Vision Computing*, 21:977–1000, 2003.